COMPUTATIONAL MODELS FOR FUNCTIONAL NEAR-INFRARED SPECTROSCOPY AND IMAGING

by

JOSHUA DEEPAK VEESA

A thesis submitted to the University of Birmingham for the degree of
DOCTOR OF PHILOSOPHY

School of Computer Science
College of Engineering and Physical Sciences
University of Birmingham
April 2021

ABSTRACT

Functional near-infrared spectroscopy (fNIRS) is a neuro-monitoring tool that is non-invasive, non-ionising, cost efficient, and portable. Its application for the traumatic brain injury patients is a well suggested approach due to its role in being able to continuously monitor key biomarkers such as the tissue oxygenation and blood haemoglobin level to understand the flow of blood supply to the tissue in the brain to assess injury in patients. In light of the great potential that fNIRS has to offer in neuro-monitoring in critical care, it is hindered by the inconsistency seldom seen in multiple research works that can be attributed to the assumptions made on tissue scattering properties to decouple their dependency along with absorption properties that can provide information about the key biomarkers useful in neuro-monitoring. These inconsistencies can also be attributed to the application of an inaccurate model to represent photon migration in underlying the biological tissue, or it can also be attributed to the unavoidable contamination of the measured fNIRS data by the superficial (skin and scalp) tissue, which is intended to probe the brain tissue, due to the typical placing of measurement probes on the head. The possibility to overcome these challenges in fNIRS methodology is examined in this thesis, and the proposed methods to overcome these are derived theoretically and validated on numerical simulation and experimental data to demonstrate better performance as compared to existing methods.

A spectrally constrained approach is designed to efficiently circumvent the coupling of absorption and scattering properties to directly yield more accurate estimates of oxygenation levels for the cerebral tissue showing an average improvement of 6.6% as compared to a

conventional and widely used approach of spatially resolved spectroscopy, in estimating the tissue oxygenation level. The uncertainty factor in the knowledge of scattering coefficient of the tissue, which is a key limitation in the conventional approach, is shown to be removed in the proposed spectrally constrained approach, therefore maintaining the methodology of subject and tissue-type independence.

With the demonstration of better performance on spectral constrained approach, the role of more spectral information i.e., broadband intensity data, to allow recovery of more information is also explored and is demonstrated that when the data is measured on a complex tissue such as the human head, an often used simple semi-infinite model based layered recovery can lead to uncertain results, whereas, by using an appropriate model accounting for the tissue-boundary structure and geometry, the tissue oxygenation levels are recovered with an error of 4.2%, and brain depth with an error of 11.8%. The algorithm is finally used together with human subject data, to demonstrate the robustness in application and repeatability in the recovered parameters that adhere well to expected published parameters.

Finally, the signal regression of fNIRS data to reduce superficial signal contamination which is well defined for a continuous wave (CW) fNIRS system is expanded to another data-types, namely phase data as used in frequency-domain (FD) fNIRS systems, by proposing a new approach for FD fNIRS that utilizes a short-separation intensity signal directly to regress both intensity and phase measurements. This is shown to provide a better regression of superficial signal contamination from both intensity and phase data-types. Intensity-based phase regression is shown to achieve a better suppression of superficial signal contamination by 68% whereas for phase-based phase regression the suppression is only by 13%. Phase-based phase regression is

also shown to generate false-positives in the image reconstruction of haemodynamic activations from the cortex, which is not desirable and therefore this work provides a better methodology for minimizing the superficial signal contamination for FD fNIRS.

All the parameter recovery models and signal processing methods presented in this work, in addition to their better performance that is shown, carry an additional and most prominent advantage of being able to be applied to all existing NIRS systems without any additional instrumentation or measurement for the purpose of providing a more accurate and robust neuro-monitoring tool.

I would like to dedicate this thesis to my dear mom,

who has been my greatest strength and strongest support.

ACKNOWLEDGEMENTS

I would like to express my deepest gratitude to my supervisors and thesis-group members. Iain Styles for his depth of understanding on the most intricate problems and his guidance in preparation and planning of the research work. Ata Kaban for her intriguing questions in our thesis group meetings that helped me stay in the right direction. A very special thanks to Hamid Dehghani for his consistent support throughout my research work, acting as a great source of knowledge, wisdom and inspiration. Our weekly meetings have provided me with an invaluable space to explore new ideas and directions of work.

I would like to thank all my colleagues, both in the Medical Imaging Lab and NIHR SRMRC, and the BitMap project partners, for creating such an inspiring scientific community to work within. A particular thanks to Mario Forcione, Matthaios Doulgerakis, Stanislaw Wojtkiewicz and Wenqi Lu for their riveting scientific discussions and friendship throughout my studies. I must also gratefully acknowledge all the volunteers who, very kindly, participated during experimental studies that proved to add a great value to the methodology developed in this work.

Finally, I would like to thank my dear mom, dad and beloved sister for always supporting me in everything I do.

This work was financially supported by the funding received from the European Union's Horizon 2020 Marie Sklodowska-Curie Innovative Training Networks (ITN-ETN) program, under grant agreement no. 675332, BitMap.

PUBLICATIONS RESULTING FROM THIS WORK

Peered Reviewed Journal Papers

A new method in functional near-infrared spectroscopy is developed that uses multi-wavelength spatially resolved continuous wave data to assess brain tissue oxygenation. The proposed method is shown to estimate the underlying scattering properties and improving accuracy of recovered tissue oxygenation parameter, contributing to Chapter 3 of this thesis.

Veesa JD, Dehghani H. Functional near infrared spectroscopy using spatially resolved data to account for tissue scattering: A numerical study and arm-cuff experiment. J Biophotonics. 2019; 12(10):e201900064.

A study to demonstrate the application of broadband intensity data in estimating the absorption and scattering parameters of cerebral and extra-cerebral tissue using a head-model based fitting approach, contributing to Chapter 4 of this thesis.

Veesa JD, Dehghani H. Hyper-spectral Recovery of Cerebral and Extra-Cerebral Tissue Properties Using Continuous Wave Near-Infrared Spectroscopic Data. Applied Sciences. 2019; 9(14):2836.

A new signal regression method for frequency-domain diffuse optical tomography system is shown to greatly improve the superficial signal regression compared to a straight forward of extension of regression technique for non-intensity data types. This is presented in Chapter 5 of this thesis.

Veesa JD, Dehghani H. Signal regression in frequency-domain diffuse optical tomography to remove superficial signal contamination. Neurophotonics. 2021; 8(1):015013.

Peer Reviewed Conference proceedings

Spectral constraint on the spatially resolved spectroscopy technique is presented and is shown to yield better estimates of tissue oxygenation, this contributes to Chapter 3 of this thesis.

Veesa JD, Dehghani H, editors. Spectrally constrained approach of spatially resolved spectroscopy: towards a better estimate of tissue oxygenation. Biophotonics Congress: Biomedical Optics Congress 2018 (Microscopy/Translational/Brain/OTS); 2018 2018/04/03; Hollywood, Florida: Optical Society of America.

Application of broadband intensity data measured on a two-layered semi-infinite medium to estimate absorption and scattering properties is demonstrated, and this forms the basis for Chapter 4 of this thesis.

Veesa JD, Dehghani H, editors. Spectral parameter recovery of cerebral and extra-cerebral tissues using broadband near-infrared spectroscopy. Clinical and Preclinical Optical Diagnostics II; 2019 2019/06/23; Munich: Optical Society of America.

The combination of broadband intensity and spatially resolved data, applied to measure the tissue oxygen saturation to estimate absorption and scattering properties is demonstrated.

Kovácsová Z, Bale G, Veesa JD, Dehghani H, Tachtsidis I. A broadband multi-distance approach to measure tissue oxygen saturation with continuous wave near-infrared spectroscopy: SPIE; 2019.

TABLE OF CONTENTS

LIST OF FIGURES

LIST OF TABLES

Chapter 1

INTRODUCTION

1.1. Background

Traumatic Brain Injury (TBI) has been one of the leading causes of deaths in young people and a lifelong disability is common in those who survive (1). It has been estimated that more than 10 million people globally are affected by TBI resulting in either mortality or hospitalization (2), and therefore is a critical public health problem worldwide. In severe cases TBI, the mortality rate is seen to be very high between 20% - 40%, and another 20% of patients remain critically disabled (3). This outcome is mainly due to the secondary cerebral ischemic injury that can occur at any time after the initial injury including during resuscitation, transport and in the intensive care unit. In fact this is observed in 90% of deaths due to head injury (4). Therefore an important aspect of improving health-care for TBI patients is to predict and prevent the secondary injuries, through continuous monitoring of subjects in clinical conditions and taking up the appropriate clinical procedure immediately when and as required (5).

Current available brain health monitoring modalities for prehospital use are pulse oximetry and blood pressure monitoring systems. The concern with these modalities is that the oxygenation and blood pressure in other tissue is not necessarily an indicative of brain directly and therefore could lead to incorrect therapy. Clinical modalities include brain monitoring methods such as intracranial pressure monitors and electroencephalography (6) and diagnostic

methods such as computed tomography and magnetic resonance imaging (MRI), often just structural rather than a functional MRI (7). These modalities are limited by their ionizing, invasive or their high cost nature making them unfavourable to be used for the diagnosis of TBI as a continuous monitoring tool (5). Near-infrared (NIR) technology has the potential to fill these gaps and can be used as a continuous nonionizing, non-invasive and a low-cost alternative to the current methods.

1.2. Traumatic Brain Injury

Traumatic Brain Injury (TBI) is defined as an alteration or impairment in brain function, caused by an external mechanical force. The term head injury, although used interchangeably with TBI, may also refer to trauma to other parts of the head such as the scalp and skull. TBI can be categorized by its severity using the Glasgow Coma Scale (GCS) based on patient response. A mild TBI (mTBI) could be a concussion caused by a sport injury where the patient is awake and responsive. At the other end of the categorization, a severe TBI would be from a more significant impact, such as motor vehicle collision, where the patient may be unconscious.

The initial impact of a TBI is likely to cause shearing of the white matter tracts and rupturing of blood vessels leading to both intra and extracranial hematomas (8). This often results in inflammation and swelling, and is referred to as the primary insult to the brain. While these are significant injuries, in themselves they are not fatal, and is instead the repercussions of these injuries further down the line that are the main source of patient mortality; these repercussions are known as secondary insults to the brain (9). The main issues in the secondary insult process are hypoxia (lack of oxygen) and intracranial hypotension (abnormally low blood pressure) (5, 10), which along with the impaired brain's intrinsic blood regulatory mechanism (cerebral autoregulation), compromise the delivery of oxygen and nutrients to cerebral tissue. Furthermore, the swelling in the brain from the initial insult increases intracranial pressure (ICP), which in turn decreases cerebral perfusion pressure (CPP), meaning that adequate cerebral tissue perfusion is further compromised causing further impairment of the brain's intrinsic autoregulation abilities (8). As these secondary injuries can take place at any time post injury, the

ability to continuously monitor patients from the moment emergency care arrives is essential for securing positive patient outcomes (5).

Standard practice for the treatment of most trauma victims (recommended by the National institute for health and care excellence and other bodies) is Permissive Hypotensive Resuscitation (PHR), which helps to reduce the risk of a secondary haemorrhage, lung injury or tissue oedema. PHR is a procedure, which involves gentle fluid infusion in order to increase systemic blood pressure to just below normal levels. The notable exception to this, is the case of TBI. This is due to concerns that PHR will cause an ischaemic insult to the brain, resulting in further damage by reducing blood pressure in a brain that is potentially already hypotensive, a topic which is still controversial. Currently the main goal in pre-hospital treatments is to use fluid therapy to avoid hypoxia and hypotension until the patient can be fully assessed in a hospital. However, the information available to emergency medics at this point in order to guide the therapy is limited to blood pressure and systemic blood oxygen saturation measurements. It is only on arrival at a hospital that more informative monitoring and assessment modalities can be utilised. More accurate information then allows clinicians to manipulate ICP and CPP safely through fluid and pharmaceutical intervention with surgical techniques also available, such as a decompressive craniectomy (11).

1.3. Established neuro-monitoring methods

Currently there are very few monitoring modalities available for pre-hospital use, which as mentioned are pulse oximetry and blood pressure monitoring systems. The concern with these modalities is that, both of them only give a systemic overview of patient health and the recorded

oxygenation and blood pressure is not necessarily an indicative specific to brain and therefore could lead to incorrect therapy. Clinical methods of brain monitoring include computed tomography (CT), MRI, ICP monitors, transcranial Doppler (TCD) and electroencephalography (6). CT and pressure monitors are the most common. There are also catheters similar to the ICP probes that can measure brain tissue oxygenation (PbtO2) and provide positive outcomes when used with ICP. CT scans are standard practice for TBI patients and when used with contrast agents can accurately show the position and size of haematomas in the brain and can guide surgical procedures. It is however only usable once the patient arrives in hospital and due to the ionizing nature and risk of moving critical patients it is not useful as a continuous monitoring tool. Similarly, ICP and PbtO2 monitors can only be installed in the hospital by a surgeon. The pressure monitors are invasive and are screwed into the skull in order to give a long-term assessment of intracranial pressure and tissue oxygenation. They also have their own associated risks with the implantation, specifically a 0.5% risk of causing a haemorrhage and a 2% risk of becoming infected (11). TCD can show blood flow velocity in the brain and has been found useful in guiding therapy to restore cerebral perfusion (12), however the results can be inconclusive and interpretation varies between users.

As there is currently no accepted modality/technique for guiding both hospital and pre-hospital therapies, this leaves a gap which could potentially be filled by functional near-infrared spectroscopy (fNIRS) as it has the depth penetration ability to assess the cortex (reaching the ideal TBI monitoring depth of 21 ± 4mm (13). The application of fNIRS for assessment of haemodynamics is widely used in clinical research due to its versatility and ease of use (14). Also, as it is non-ionizing and significantly cheaper to purchase and run than CT/MRI scanners, it can

be used to continuously monitor TBI patients, from the moment emergency medics start treatment. As cerebral tissue oxygenation index (TOI) and tissue haemoglobin index (THI) are the key parameters that clinicians are concerned with (15) when it comes to monitoring TBI patients, the ability to use fNIRS which can measure such parameters would be advantageous.

There is evidence indicating that the changes in TOI and THI as measured by fNIRS can also be used as an indicator of ICP (16, 17), yet it is considered unreliable to predict ICP consistently (18). However, NIR based methods like diffuse correlation spectroscopy that can measure the cerebral blood flow (19), have been demonstrated to estimate the ICP non-invasively (20-22). In its current state, NIRS can supplement the current TBI assessment methods although not replacing them (23-25). However, the ability of NIRS to obtain combined information regarding the quantity of blood reaching the cerebral tissue along with the oxygen saturation levels of the supplied haemoglobin, gives it a distinctive advantage in the field of non-invasive monitoring in TBI (15).

The key challenges in fNIRS that decide the accuracy, with which the cerebral tissue parameters can be predicted, depends mainly on these factors:

a) Excitation and detection mode: The measured data-type can be either attenuation of transmitted light intensity (continuous wave NIRS), attenuation of light intensity combined with phase shift of the modulated light (frequency-domain NIRS), or the intensity distribution of the time of flight of photons (time-domain NIRS). The additional data-types measured in frequency and time-domain NIRS systems can therefore yield more accurate absolute parameter recovery by accounting for tissue scatter and hence photon pathlength, but are heavily limited by the low signal-to-noise ratios of these

additional data-types. While the continuous wave (CW) NIRS has limited information as compared to frequency and time-domain NIRS systems to estimate the underlying tissue properties, the robustness and cost effectiveness of CW-NIRS provides an advantage, provided that a more accurate and tissue specific absolute parameter recovery methods are employed, which forms the basis for the work presented in Chapter 3 and 4.

b) Contamination of the measured signal by the superficial tissue (skin and skull) that covers the cerebral region. This can be described as a two-fold problem. On one hand, the absolute value of NIRS measurements are effected by both cerebral and extra-cerebral tissue and therefore any information relating to just the cerebral tissue is inherently contaminated. On the other hand, the time-traces of the NIRS signals, which are used to observe the underlying haemodynamic changes over time, are also contaminated by the extra-cerebral superficial tissue. These are explained further in Chapter 2.

1.4. Research aims

In view of the key challenges listed above, given the current state of NIRS in the application of monitoring TBI patients by estimating TOI, oxy and deoxy haemoglobin concentrations, the primary focus of the research is to the address the following hypotheses:

1. Measurement of TOI using NIRS requires absorption coefficient at least two wavelengths. While the conventional methods of continuous wave NIRS cannot extract (de-couple) absorption and scattering properties of the tissue from intensity only measurements at each wavelength, the use of multi-spectral information can help in extracting absorption

and scattering properties by spectrally constraining the problem and therefore estimating more accurate TOI values.

2. The application of multi-distance broadband intensity measurements can distinguish between cerebral and extra-cerebral tissue's absorption and scattering parameters.
3. The use of layered head-model based parameter recovery method greatly improves the accuracy of cerebral tissue parameters as compared to the conventionally used homogenous or even the simplified layered slab models.
4. While the use of intensity and phase measurements can greatly improve the localization and resolution of brain activation maps, the superficial signal contamination still poses an issue with its conventional application on phase measurements but alternative regression method can be developed for the phase measurements.

The interaction of near-infrared light with matter, and models to accurately reflect the light propagation in biological tissue are presented in Chapter 2. It also explains the background of the key challenges faced by existing fNIRS methods which are broadly mentioned in the previous section forming the basis for the research aims listed above. Chapter 3, deals with tackling the limitations experienced by an intensity-only NIRS measurement systems, by adding a spectral constraint to the recovery model. The application of broadband intensity data to retrieve both cerebral and extra-cerebral tissue parameters is visualized in Chapter 4, overcoming the non-uniqueness challenge faced by intensity based parameter recovery models. The importance of using an accurate model based recovery approach reflecting the shape and structure of the medium being probed is also discussed in elaborate way. The reduction in the contamination of the measured NIRS data-types by the superficial tissue, through pre-processing methods such as

the signal regression is explained in Chapter 5 specifically for the phase data in FD systems and highlights a path towards the application on other data-types. The conclusive remarks and directions for the future work extending the research work presented in this thesis are described in the final Chapter 6.

Chapter 2

DIFFUSE OPTICAL SPECTROSCOPY AND IMAGING

2.1. Introduction

The utilization of high-energy light (x-rays and gamma rays) to image biological tissue is well established within the clinical setting, with Computerized Tomography (CT) X-ray and Positron Emission Tomography (PET) often being used in hospitals. Incident radiation (electromagnetic light) can be assumed to travel in a straight line through a medium with contrast coming from any decrease in intensity of the detected light due to absorption. However, the propagation of NIR light in biological tissue is a more complex phenomenon. Unlike x-rays, NIR light does not travel in a straight line inside biological tissue, as the dominant interaction process is no longer absorption; scattering now plays a major role and the light which originates from a point source becomes dispersed.

In order to predict or reconstruct the path of NIR light in tissue, and to better predict its optical properties, computational methods and models are required. Modelling of NIR light propagation can be done using the Radiative Transfer Equation (RTE) or simplifications of the RTE such as the Diffusion Approximation.

2.2. Interaction of light with the biological tissue

The prediction of NIR photon migration in tissue is based on our understanding of how light interacts with biological media. The main interaction methods of a photon with tissue are scatter and absorption; this section aims to describe how these interactions take place and why they cause changes in detected intensity at a given measurement point. Examples of absorption and scattering spectra of the main biological tissue constituents (chromophores) are shown in Figure 2.1 and Figure 2.2, where the area of high scattering and lower absorption in the NIR range can be seen.

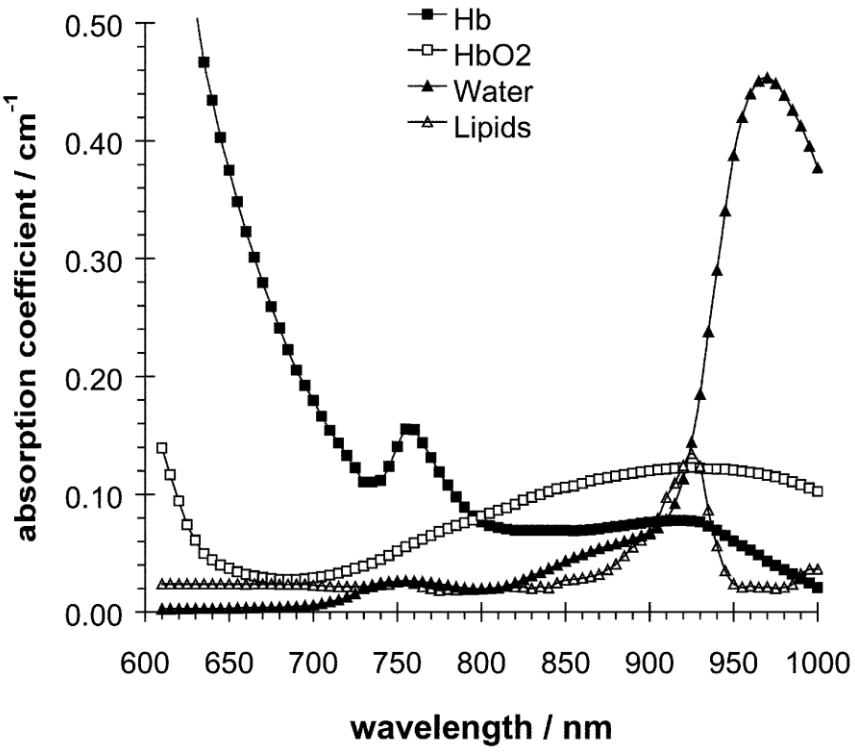

Figure 2.1. Absorption spectra of main tissue constituents in the range of 600-1000 nm. The curves refer to 100% water (▲), and lard (△), and to 100 µM of oxy- (□) and deoxy- (■) haemoglobin. (26)

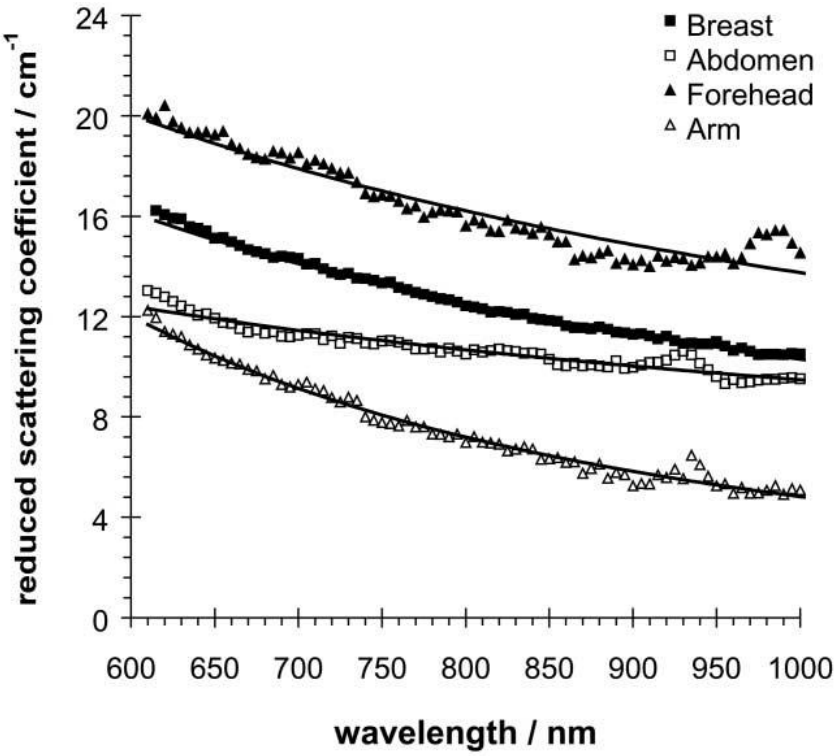

Figure 2.2. Scattering spectra of the abdomen (□), the female breast (■), the forearm (△), and the forehead (▲). (26)

A photon is the name given to a 'packet' of energy, with the energy of the photon being directly related to its frequency or wavelength (Planck-Einstein relation); as shown in equation (2.1), where E is the photon energy, f its frequency, λ its wavelength, c is the speed of light in the medium and h is Planck's constant.

$$E = hf = \frac{hc}{\lambda} \tag{2.1}$$

2.2.1. Absorption

The process of absorption occurs when a photon transfers its energy to molecules inside the medium being traversed. The transfer of energy takes place via excitation of an electron moving it from a lower energy level, or ground state, to a higher energy level or excited state. Once the excitation has taken place, the electron can return to its original, or intermediate, state by releasing some or all of the absorbed energy. This can take place through a variety of mechanisms, which can be generalised under luminescence or thermal energy. NIR light is described as 'non-ionising' as its photons do not have sufficient energy to excite an electron to a level where it can break free of its parent nucleus, a process which can cause tissue damage.

The energy levels for electrons in different molecules (chromophores) are specific and as the energy of a photon is directly related to the wavelength of the light, there is a wavelength dependence of the amount of absorption by a specific molecule as seen in Figure 2.1, a principle that is essential for NIRS.

The probability of a photon, of a particular wavelength, being absorbed within a medium per unit of distance travelled is dependent on its absorption coefficient (μ_a). This absorption coefficient is a measure of the net absorption from all the constituents absorbing molecules (chromophores) such as oxy-haemoglobin (HbO), deoxy-haemoglobin (Hb) and water (H_2O) in the tissue which can be defined by the Beer-Lambert Law as:

$$\mu_a(\lambda) = \epsilon(\lambda)_{HbO} C_{HbO} + \epsilon(\lambda)_{Hb} C_{Hb} + \epsilon(\lambda)_{H_2O} C_{H_2O} \quad (2.2)$$

The molar extinction coefficient (ϵ) specifies the absorption coefficient per unit molar concentration of the respective chromophore and is dependent on the wavelength (λ) of light. The concentration of the chromophores is given by 'C'.

Given an initial intensity of light (I_0), the relationship between its reduced intensity (I) over a distance (d) travelled through a non-scattering medium with absorption coefficient μ_a, is exponential and is defined by equation (2.3) which is referred to as the Beer-Lambert Law.

$$I(d) = I_0 e^{-\mu_a d} \tag{2.3}$$

However, for biological tissues scattering is the dominant interaction (which is the reason NIR light can probe deeper into biological tissue than visible light, and is often termed as Diffuse Imaging) and therefore the relation between output intensity and propagation distance is more complex than equation (2.3), and as discussed in the later sections alternative relationships must be used.

The main NIR absorption species in biological tissue are haemoglobin (split into oxygenated (HbO) and deoxygenated (Hb) components), Water (H_2O), and others such as cytochrome oxidase and melanin. Recovering concentrations of HbO and Hb can also provide measures of blood oxygen saturation ($SO2 = \frac{HbO}{HbO+Hb} x100$) and total haemoglobin concentration ($HbT = HbO + Hb$). The saturation of the blood is an overall value covering both

the venous and arterial components of blood, which are usually approximate to the ratio of 75:25 as the venous contributions are stronger.

By measuring the absorption of light at multiple wavelengths in the NIR region, combined with the extinction coefficients (for each chromophore at the measured wavelengths) it is possible to calculate the concentration of each chromophore within a sample, using equation (2.2).

2.2.2. Scattering

Scattering is the process by which the direction of a photon is changed. It can be modelled as a series of interactions between spherical particles and photons (Mie and Rayleigh Theory) which, in the context of NIR light, are elastic meaning no energy is transferred from the photons during this interaction process. There are other forms of scattering which are non-elastic and results in the reduction in incident photon energy, such as Raman scattering; but are less likely in the NIR region due to the associated energy level transitions. Mie scattering dominates when the size of the particles is similar to that of the optical wavelength (NIR), which is the case in biological tissue where cell membranes, nuclei and mitochondria are key scattering particles. A mismatch in refractive indices between constituent particles and the background medium can also cause a significant amount of scattering, as governed by Snell's Law.

Similar to absorption coefficient, the scattering coefficient (μ_s) defines the probability of a scattering event to occur per unit length travelled by the photon. The reciprocal of the scattering coefficient gives the average distance a photon will travel in a medium before undergoing a scattering event. Another factor to consider with scattering is the angle of direction

of the scattered light, known as anisotropy. This is important as the probability of light being scattered is not equal in all direction, so there is often a preference for forward or backward scatter. Therefore, to account for this, a reduced scattering coefficient can be used that incorporates an anisotropy factor, 'g' which can range from -1 (for back scatter) through to 1 (for forward scatter) as shown in equation (2.4). The anisotropy factor can be estimated experimentally and a typical value for biological tissue is 0.9, indicating forward scattering.

$$\mu_s' = (1 - g)\mu_s = a\,\lambda^{-b} \tag{2.4}$$

The empirical approximation of the Mie scattering theory with equation (2.4) has shown a good fit (27, 28) to the reduced scatter coefficient of a tissue (μ_s') with respect to the wavelength (λ). The scatter amplitude a and the scatter power b are related to the particle sizes and density of scatters in a tissue. Another well-used approximation is a linear fit between reduced scattering coefficient and the wavelength which is further detailed later in chapter3.

2.3. Radiative transport equation and diffusion approximation

Based on the scattering and absorption parameters outlined in Section 2.2 the path of diffuse light can be predicted by looking at the photon interactions within the medium. The prediction of light propagation using the radiative transfer equation (RTE) is shown in equation (2.5). The original basis for the RTE was developed by Boltzmann in the form of the Boltzmann transport equation in 1872. The physical quantities shown in the equation are as follows: $\vec{r}$ is the position;

$\hat{s}$ is the unit direction vector; t is time; c is the speed of light in the medium; μ_t is the total attenuation coefficient ($\mu_a + \mu_s$), a combination of both absorption and scattering coefficient; $d\Omega'_{\mathrm{SA}}$ is the differential solid angle term in the direction $\hat{s}'$, $L(\vec{r}, \hat{s}, t)$ represents radiance (photon density) as a function of time at a given position $\vec{r}$ in a given direction $\hat{s}$, the photons reach this position from different direction originating from the source undergoing multiple scattering events, and some photons being absorbed by the medium and lost; $\Theta(\hat{s}', \hat{s})$ is the normalized scattering phase function representing the probability of scattering from a direction $\hat{s}'$ to a direction $\hat{s}$ and '$c.Q(\vec{r}, \hat{s}, t)$' is equal to the number photons emitted by the source per volume per unit time defined as a function of time at a given position $\vec{r}$ in a given direction $\hat{s}$, and the term Q is commonly addressed as the source term (29, 30) as it can be separated from the other parts of the RTE as shown below.

$$\frac{1}{c}\frac{\partial L(\vec{r}, \hat{s}, t)}{\partial t} + \hat{s} \cdot \nabla L(\vec{r}, \hat{s}, t) + \mu_t L(\vec{r}, \hat{s}, t) = \mu_s \int_{4\pi} L(\vec{r}, \hat{s}', t)\, \Theta(\hat{s}', \hat{s}) d\Omega'_{\mathrm{SA}} + Q(\vec{r}, \hat{s}, t) \quad (2.5)$$

Given the complexity of the RTE equation it is most commonly simplified into the Diffusion Approximation (DA), which is valid when the scattering is more dominant than absorption and the region of interest is far (i.e. diffuse) from any sources or boundaries given the light fluence does not change rapidly with time (30, 31). Using these principles, the RTE can be simplified into:

$$\frac{\partial \Phi(\vec{r},t)}{c\,\partial t} + \mu_a \Phi(\vec{r},t) - \nabla \cdot [\kappa\, \nabla \Phi(\vec{r},t)] = q(\vec{r},t) \tag{2.6}$$

Here, κ is the diffusion coefficient given as $\kappa = 1/3(\mu_a + \mu_s')$; Φ is the fluence rate, and μ_s' is the reduced scattering coefficient. The above equation represents transient nature of diffuse light propagation. The steady-state representation of it (by integrating over time) gives the continuous wave diffusion equation (or simply identified as the diffusion approximation) which can be written as follows:

$$-\nabla \cdot [\kappa\, \nabla \Phi(\vec{r})] + \mu_a \Phi(\vec{r}) = \mathrm{q}(\vec{r}) \tag{2.7}$$

Solving the diffusion equation requires a boundary condition for which the modified Robin boundary condition (mRBC) is generally used which is given as (32):

$$\text{mRBC:} \qquad \Phi(\vec{r}) + 2\kappa\, A\, \hat{n} \cdot \nabla \Phi(\vec{r}) = 0, \ \forall \ \vec{r}\, \epsilon\, \partial\Omega \tag{2.8}$$

$$\text{where, } A = \frac{2/(1-R_0) - 1 + |\cos\theta_c|^3}{1 - |\cos\theta_c|^2} \text{ and} \tag{2.9}$$

$$R_0 = \frac{(n_m - 1)^2}{(n_m + 1)^2} \tag{2.10}$$

Here, $\partial\Omega$ defines the boundary of a medium represented by Ω and 'n_{m}' is its refractive index, and for air '$n_{\mathrm{AIR}} = 1$'. $\theta_{\mathrm{c}} = \sin^{-1}(1/n_{\mathrm{m}})$, is the critical angle beyond which total internal reflection occurs at the air-tissue interface for the photons moving from tissue to air.

With fewer variables (only space and time, versus space, time and direction for RTE), the diffusion equation is a simpler differential equation to solve than the RTE. The solution is usually recovered in one of two ways either analytically through computational modelling. While analytical methods (33-36) involve calculating the solutions the simplest form for the diffusion equation using Green's functions for more general and simpler geometries of the medium (37), the computational methods (32, 38-41) however employ modelling techniques to solve the diffusion equation or the RTE on a given medium and boundary conditions, and this is relatively more time consuming.

2.3.1 Analytical Methods

An analytical solution is a direct mathematical approach where an exact answer can be found, and in this case the equation being solved is the partial differential equation of Diffusion Approximation given by equation (2.7). Depending on the geometry of a situation, solving the diffusion equation is not always possible using analytical methods. There are however a set of simple or semi-complex geometries such as: homogenous infinite medium, homogenous semi-infinite medium (37), two or three layered semi-infinite heterogenous medium (33), where analytical solutions can be derived that will allow direct calculation of light intensity at a given distance from the source. An analytical solution is the fastest way to calculate light fluence in

order to reconstruct measurement data and is used in fNIRS systems where real time data processing is required and the geometries are simple.

In a majority of cases a continuous wave fNIRS device would be used to measure differential changes in chromophore concentrations from a single source-detector pair. Here, a modified Beer-Lambert Law (MBLL) is applied (42), which essentially adds a scatter dependent term to the attenuation ($\log(I_0/I)$) as defined in equation (2.3), and by assuming scatter changes to be time-invariant a change in attenuation of light intensity at a wavelength can be used to measure the changes in absorption coefficient at the respective wavelengths, which can then be utilised to obtain a global estimate of chromophore changes in the target volume using equation (2.2).

The analytical solution to the diffusion approximation can also be used to find more accurate estimates of the absorption and scattering coefficients (depending on the measurement type) to improve the accuracy of the recovered chromophore concentrations. Analytical solutions to the diffusion approximation for various geometries (such as slabs cylinders and spheres) have been derived using Green's functions: these models can be used for forward modelling of data. These solutions tend to be based on a homogeneous medium although there are analytical solutions to the DA, which are built on more complex models such as layered slabs. Even with more complex geometries, analytical solutions can only provide accurate results in certain situations (e.g., Muscle oximetry).

In the situation where there are multiple source-detector pairs at different separations, such as a DOT array, the approach for using an analytical solution to the DA is less direct; this is where forward modelling of boundary data is used. Boundary data is simply a simulation of the intensity

measured at given points on the boundary of a medium, in this case a semi-infinite slab. The data fitting routines do vary but a general methodology for fitting measurement data to an analytical model in order to obtain optical property estimates, μ_a and μ_s' (or the chromophore concentrations and scattering parameters) is defined as follows:

- Starting with an initial guess of optical parameters the boundary data is simulated and compared with the measurement dataset, the optical parameters are then updated for the next iteration so that the sum of squares of difference between simulation and measurement dataset is minimized (least-square minimization model).
- The iterations are repeated until the mismatch between the two datasets reaches a predefined acceptance level, or a set number of iterations are reached.

Due to the simplicity of analytical models this process is still very fast even in the event of modelling large arrays of sources and detectors.

This method would converge easily when the measurement data has high signal-to-noise ratio. However, in the situation where the data is noisy or the initial guess at the optical properties is far from the solution, the least-squares minimization method can break down and yield incorrect results. This can also be an issue when the analytical model being used is not truly representative of the measurement geometry or where the changes in optical properties are expected to be large (i.e., the changes are not small enough to be linear). For more complex geometry modelling of a layered head for example, computational methods are required to obtain more accurate results.

2.3.2. Computational Methods

When looking at more complex geometries, analytical solution may be either unavailable or inappropriate, instead computational methods (32, 38-41) can be used to model forward data for reconstructions. Whereas an analytical solution will most often be fully homogeneous or nearly homogeneous in a target region, a numerical solution can use fully heterogeneous models to give more accurate results in such scenarios, although the reconstruction time is longer due to computational complexity. Numerical solutions are often performed using finite element models (FEM), which are utilized in the following chapters to reconstruct data and is explained in detail further in this section.

Monte Carlo (MC) is another commonly used computational method (41) of modelling the RTE and is often used as a gold standard for validation of other computer models with heterogeneous media. MC uses a statistical approach to modelling and simulates the paths of millions of individual photons through a series of random walks until a set level of counting statistics obtained. The MC techniques are highly versatile and have been implemented for multi-layered tissues geometries, such as that of the human head. The computational time required to complete the simulations is the reason MC methods are not currently as widely used as FEM-based approaches, however there have been many advances in both parallel computing and utilisation of graphics processing units in order to reduce this computational time.

The reconstruction of optical parameters or chromophore concentrations of medium can be of two types:

a) Dynamic parameters recovery: the dynamic changes in light intensity over time is used to obtain the dynamic changes in tissue parameters (chromophore concentrations). The mapping from intensity to tissue parameters is implemented in a single linear inversion step using the sensitivity or Jacobian matrix (change in intensity per unit change in tissue parameter, as defined in the subsection 2.3.2.2. Inverse problem),

b) Absolute parameter recovery: the absolute values of the tissue parameters (chromophore concentrations) are obtained using an iterative fitting algorithm by modelling the light intensity (forward model) with an approximated tissue parameters, these are updated in each iteration to minimize the difference between measured light intensity and the modelled light intensity data (inverse model). The forward and inverse models are explained further in detail below.

2.3.2.1. Finite element method for forward model:

The finite element discretization of a given volume of a medium defined by Ω, can be obtained by subdividing the domain into N_{e} number of small elements joined at N interconnecting nodes. In finite element method, the fluence at a given point, $\Phi(\mathbf{r})$, is approximated by the piecewise continuous polynomial function,

$$\Phi^{\mathrm{a}}(\mathbf{r}) = \sum_{i=1}^{N} \Phi_i u_i(\mathbf{r}) \in \Omega^a \tag{2.11}$$

where, Ω^a is a finite dimensional subspace spanned by the basis functions u_i chosen to have a limited support. The diffusion approximation equation (2.8) can be represented in FEM framework (32, 38) as a system of linear algebraic equations:

$$(\mathbf{K}(\kappa) + \mathbf{C}(\mu_a) + \mathbf{F})\mathbf{\Phi} = \boldsymbol{q_0} \tag{2.12}$$

where the matrices **K, C, F, Q** have entries given by,

$$\mathbf{K}_{ij} = \int_{\Omega} \kappa(\mathbf{r})\, \nabla u_i(\mathbf{r}) \cdot \nabla u_j(\mathbf{r})\, d\Omega \tag{2.13}$$

$$\mathbf{C}_{ij} = \int_{\Omega} \mu_a(\mathbf{r})\, u_i(\mathbf{r}) \cdot u_j(\mathbf{r})\, d\Omega \tag{2.14}$$

$$\mathbf{F}_{ij} = \frac{1}{2A} \oint_{\partial\Omega} u_i(\mathbf{r}) \cdot u_j(\mathbf{r})\ d(\partial\Omega) \tag{2.15}$$

$$\mathbf{Q}_{ij} = \int_{\Omega} u_i(\mathbf{r}) \cdot \mathrm{q}_0(\mathbf{r})\, d\Omega \tag{2.16}$$

The estimation of photon fluence now depends on inversion of the sparse matrix ($\mathbf{K}+\mathbf{C}+\mathbf{F}$). The simulation reflects the experimental data when the source is modelled at one transport scattering distance $1/\mu_s{}'$ within the outer boundary $\partial\Omega$

2.3.2.2. Inverse problem

The objective of the inverse problem is to recover the optical properties $\boldsymbol{\mu}=[\boldsymbol{\mu}_{\mathrm{a}},\boldsymbol{\mu}_{\mathrm{s}}']$ at each node (or each region or the bulk properties) in the mesh using discrete light intensity measurements on the boundary of the medium. The recovery can be achieved using any minimization method with a regularization term to solve ill-conditioned problems based on the application. Here least square minimization with Tikhonov regularization is being used. If the measured output intensity is represented by $\mathbf{I}^{\mathrm{m}}$ and the modelled data as $f(\boldsymbol{\mu})$ (either analytical or numerical forward models) for M source–detector measurements, then the standard Tikhonov minimization function is given by,

$$\chi^2=\min_{\mu_a,\,\mu_s'}\left\{\sum_{i=1}^{M}(\mathrm{I}_i^{\mathrm{m}}-f(\boldsymbol{\mu}))^2+\alpha\sum_{j=1}^{N}\left(\mu_j\right)^2\right\} \tag{2.17}$$

Here, $\mathbf{I}^{\mathrm{m}}$ and $f(\boldsymbol{\mu})$ are matrices of $M\times1$ dimension, $\boldsymbol{\mu}$ i.e. $\boldsymbol{\mu}_{\mathrm{a}}$, $\boldsymbol{\mu}_{\mathrm{s}}'$ are matrices of $N\times1$ dimension and α is the Tikhonov regularization parameter defined as the ratio of variances of the measurement data and optical properties. In case of a regional recovery the N will be the number of regions, and in case of bulk recovery it will be 1.

By setting the first derivative of equation (2.17) to zero, i.e. $\frac{\partial \chi^2}{\partial \mu} = 0$ and ignoring the higher order terms, we obtain the update equation for optical parameter at the i^{th} iteration as,

$$\Delta\mu = (\mathbf{J}^T\mathbf{J} + \alpha\mathbf{I})^{-1}\mathbf{J}^T\left(\mathbf{I}_{\mathrm{i}}^{\mathrm{m}} - f(\boldsymbol{\mu}_{\mathrm{i}})\right) \tag{2.18}$$

Here, $\mathbf{J}$ is the sensitivity matrix (Jacobian) given by $\frac{\partial f(\boldsymbol{\mu})}{\partial \boldsymbol{\mu}}$. For data using multiple wavelengths, the chromophore concentrations and the scattering parameters can be directly calculated by modifying the Jacobian matrix and measurement matrix accordingly as described in (31), from which the tissue oxygenation levels in each region can be recovered. Different regularization methods were investigated, such as generalised least square minimization, singular value based regularization in an effort to improve the convergence and the accuracy of recovery (43).

It should be noted that the reconstruction is always limited by the noise in real data, which is more predominant for larger source–detector separations. Hence, the measurements with very large source–detector separations are ignored in the reconstruction procedure. Also, with real measurements before beginning the reconstruction procedure, calibration of the data has to be done by taking measurements on phantoms of known optical properties and comparing it with the corresponding modelled data for the phantom of same optical properties (44-49).

2.4. Types of near-infrared systems

The relative transparency of human tissue including the skull in the near–infrared range as first shown by Jobsis in 1977 (50), has been an initiating step towards the use of near–infrared spectroscopy (NIRS) in non-invasive monitoring of oxy and deoxy haemoglobin in the brain. With the advancements in the technology of light sources and the detection systems, today's NIRS can be broadly classified into three different modalities based on their detection mode: continuous wave (CW), frequency domain (FD), and time resolved (TR) systems.

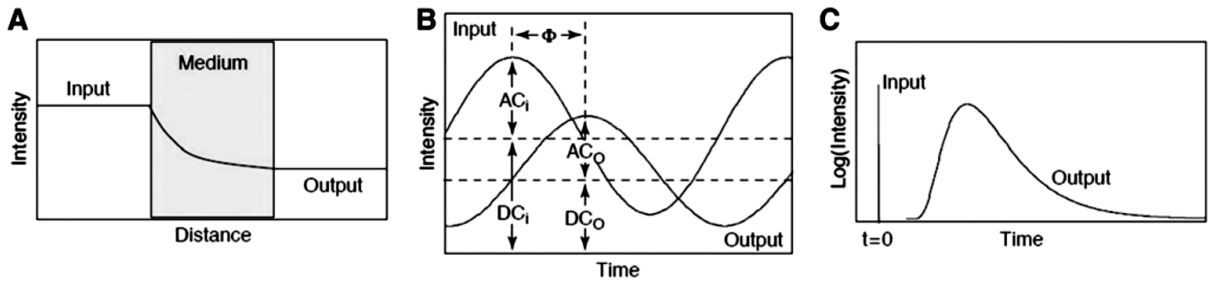

Figure 2.3. Illustration of three different types of NIRS systems (A) continuous wave, (B) frequency-domain, and (C) time-domain. (15)

Continuous wave systems are the simplest of the three types. They are solely based on intensity measurements i.e. near–infrared light that is sent into the tissue and the intensity of the re-emerging light is measured. CW systems using multi-wavelength multi-channel (more than one measuring distances) measurements were shown to be able to recover absolute values of chromophore concentrations of the tissue assuming the knowledge of the scattering parameters (51, 52).

Frequency domain or phase modulation spectroscopy operates in Fourier domain. This means the light sources are intensity modulated typically at radio frequencies (mostly 100 MHz). After passing through the tissue the intensity and phase of the emerging wave are measured. The phase shift between the source signal and detected signal is related to the time of flight or the average pathlength of light travelled through the tissue. Most of the systems use a single modulation frequency and multiple distance measurements (53). With more information compared to CW systems, this can give a more accurate absolute recovery of the tissue absorption and scattering properties.

Time resolved spectroscopy also known as time-domain spectroscopy, is a technique that measures the time of flight in addition to the light intensity. It does so by emitting a short (~100 pico-seconds) pulse of light (54) into the tissue and measuring the time point spread function of the light after it has passed through the tissue. Due to the scattering process, the pulse will broaden as seen in Figure 2.3, and due to absorption, the intensity will be reduced. The result of such a measurement is a histogram of the number of photons on the y-axis and their arrival times on the x-axis, this is called the distribution of time of flight (DTOF) of photons. The DTOF also contains information about the depth of the photonic path, because photons that arrive later have a higher probability of having travelled deeper. The absorption and reduced scattering coefficients are calculated (55-57) from the DTOF, and these absorption coefficients at multiple wavelengths are utilised to calculate the absolute values of oxygenated and deoxygenated haemoglobin (58). Both frequency domain and time domain methods require sophisticated and expensive instrumentation.

Continuous wave systems have a low cost, simpler instrumentation, high data acquisition rates, and easy portability. Unlike the time-resolved and frequency domain systems a stable optical contact is critical in continuous wave systems (59). Recent developments in software modelling (31) for light absorption and scattering through biological tissue enabled a far more accurate prediction of how light travels through the tissues of skin, skull and brain. Recent studies also show that using modelling methods such as those in NIRFAST (an open-source finite-element model based tool for simulation of light propagation in biological tissue), assuming the knowledge of scattering properties it is possible to accurately determine the physiological parameters in each layer of the head (60) using CW measurements. This presents a wide scope of improvement in the existing algorithms of continuous wave near–infrared spectroscopy and imaging methods.

2.5. Challenges in Diffuse optical spectroscopy and imaging of brain

2.5.1. Non-uniqueness in CW NIRS

The non-uniqueness in diffuse optical tomography (61), states that simultaneous recovery of absorption and scattering coefficients cannot be achieved using single wavelength continuous wave measurements and any attempted reconstructions would thereby lead to cross-talk between the absorption and scattering coefficients. Later the recovery of both chromophore concentrations and scattering parameters using multi-wavelength data has been explored in the context of breast imaging (62, 63). These results established a similar condition for non-uniqueness in terms of the multi-spectral parameters i.e. chromophore concentrations C_i,

scattering amplitude 'a', and scattering power 'b'. However, the choice of wavelengths was optimized (62-64) such as to increase the unlikeliness of two different parameter-sets capable of producing the same data, so that it minimizes the cross-talk between the recovered images of chromophore concentrations and scattering parameters. This is based on approximations that are more specific for a breast tissue which is nearly homogenous. For a more complex layered tissue such approximations are not valid and the absolute parameter recovery would be rather challenging. Recent studies (60) have demonstrated the potential of continuous wave diffuse optical tomography (CW-DOT) in recovering regional values of oxygen saturation using subject specific and atlas models of the head, but with the assumption of the knowledge of scattering parameters. This presents a wide scope of improvement in the existing algorithms of continuous wave near–infrared spectroscopy and imaging methods. The non-uniqueness problem in CW NIRS is addressed in Chapter 4 where the effect of regional constraints to the parameter recovery is demonstrated and is used to overcome the possibility of multiple solutions and limiting the recovery to unique solutions.

2.5.2. Superficial signal contamination

The topic of superficial contamination is a prominent issue within NIR imaging and spectroscopy of brain, this section is designed to explore some of the existing methods that have been devised to reduce its the effects. Any NIRS signal with a source detector distance sufficient enough to probe the cerebral tissue, will sample not only deep tissue signals but also superficial tissue signals. Therefore, to reduce the superficial contamination from deep tissue information the use of multi-distant source-detector combinations is adopted.

2.5.2.1. Spatially resolved spectroscopy

Spatially resolved spectroscopy (SRS) was a technique developed (52) to measure the tissue oxygenation index (TOI) in deep tissues with reduced contamination from superficial layers by analysing the gradient of light-attenuation $A = \ln(I_0/I)$ at large source-detector separation (ρ) given as,

$$\frac{\Delta A}{\Delta \rho} = \frac{\Delta \ln(I_0/I)}{\Delta \rho} = -\frac{\Delta \ln(I)}{\Delta \rho} \approx \sqrt{3\mu_a \mu_s'} + \frac{2}{\rho} \tag{2.19}$$

The attenuation gradient $\Delta A/\Delta \rho$ is typically measured by two detectors that are closely spaced as compared to their distance from source (for example: detectors separated by 6 mm compared to source-detector distances of ~40 mm for a commercially available NIRO-200NX system). NIR light is attenuated by the superficial layers as well as the cerebral tissue before reaching the detectors. For large source-detector separations, the sensitivity of light attenuation due to the superficial layer is similar at these two detectors as demonstrated in Figure 2.4 and therefore the sensitivity of gradient measurement at these superficial layers becomes much lower.

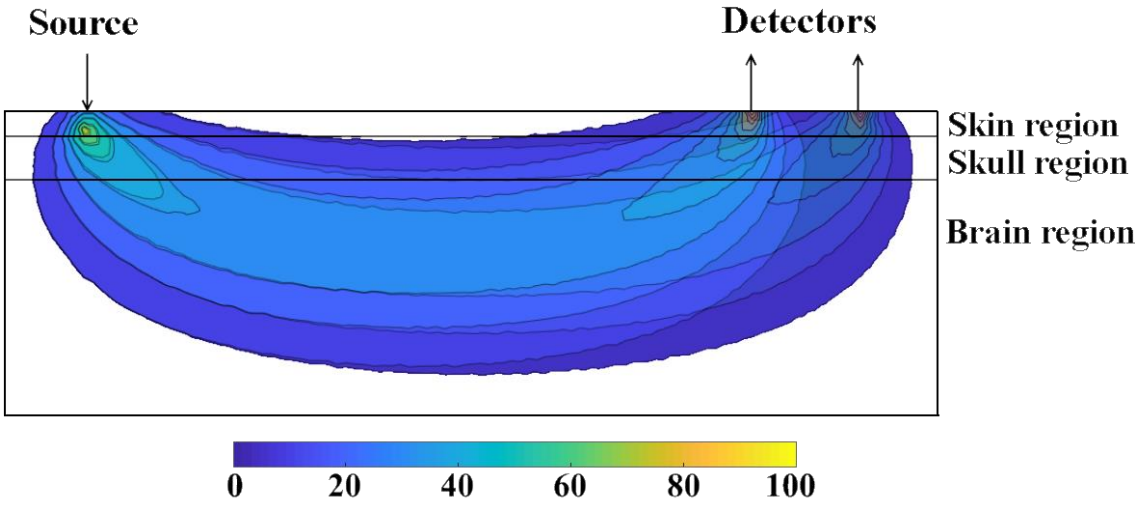

Figure 2.4. A qualitative schematic showing the sensitivity of light-attenuation in a three-layered medium. The two detectors are modelled at 37 mm and 43 mm from the source.

This reduction of light sensitivity to superficial tissue for the gradient of attenuation measurement is better illustrated in Figure 2.5. Here, the total sensitivity of intensity due to absorption is plotted as a function of depth for both detectors at distances of 37 and 43 mm from the source as well as the gradient of attenuation between them, as simulated using NIRFAST.(31) This is calculated for a source detector separations of $\rho = 37$ and $\rho = 43$ mm using a three-layered rectangular mesh (200×100×100 mm^3) with mean element size of 0.7 mm^3, layer-1 thickness of 5 mm (depicting skin), and layer-2 thickness of 8 mm (depicting skull), using an average estimate of optical properties of biological tissue (65). As seen, the gradient of attenuation is less sensitive to the superficial layer as compared to individual attenuation measurements, which implies that the measured gradient of attenuation is comparatively less affected by the haemodynamics of superficial layers, while providing higher sensitivity at deeper regions.

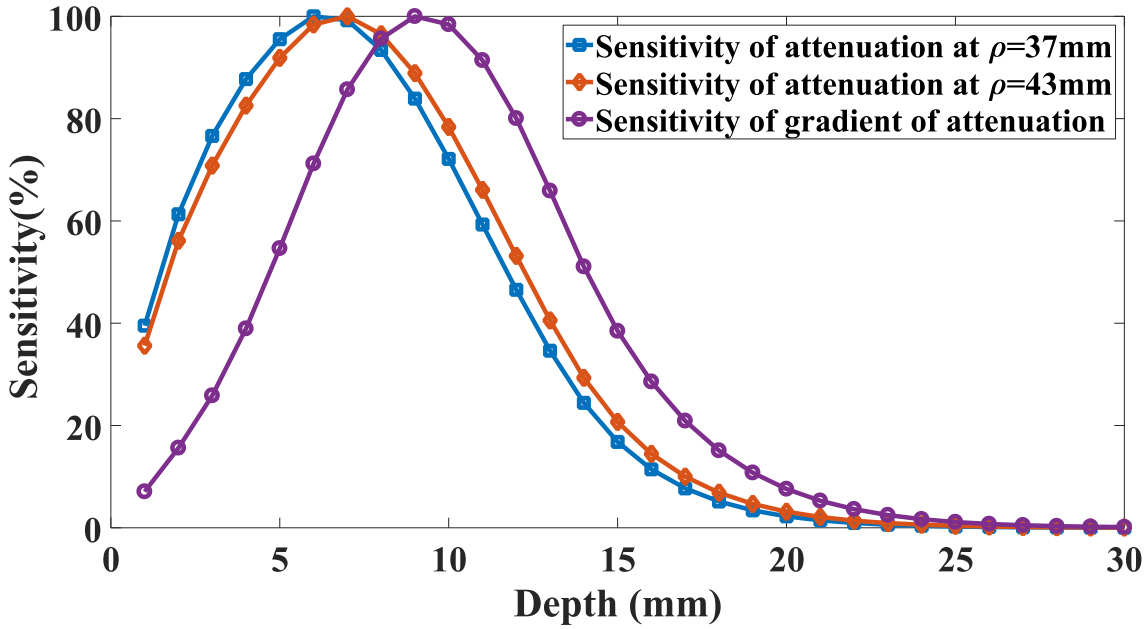

Figure 2.5. Sensitivity of attenuation with respect to depth for individual detectors as well as the gradient between them.

The absorption coefficients are estimated at multiple wavelengths by assuming the scattering properties based on empirical data (66) in order to further estimate TOI. This assumption is due to the inseparability of absorption and scattering coefficient from their relation with intensity gradient measurement. The scattering properties however vary across different subjects and tissue types and can lead to unreliable estimates of TOI, and therefore this assumption is a major setback of this method. This topic is discussed in detail in the Chapter 3 where a new spectrally constrained approach is demonstrated to take account for the underlying scatter properties and therefore estimated more accurate TOI.

2.5.2.2. Signal regression

In CW-NIRS, a short distance source-detector (SD) pair at around 15 mm is used that will sample mainly superficial regions together with a long SD pair at around 30 mm which samples both deep

and superficial regions. The short SD intensity measurement can be used as a regressor to remove the superficial contributions from the long SD intensity measurement (67-69). This is a feature that is inherent in CW-DOT where 3D reconstructions of optical properties automatically separate contributions by layer, also having multiple overlapping measurements obtained over a smaller sample area will improve the ill-posed nature of the inverse problem that can improve the accuracy of image reconstruction. However, the parameter recovery still suffers from the hyper sensitivity in superficial regions, and therefore the superficial signal regression is still performed on the measured NIRS signals prior to reconstruction step to significantly improve the cerebral haemodynamic recovery and the contrast of the recovered 3D haemodynamic activations (70).

While, the recent advancements in FD-DOT (71) show significant improvement in the localization and effective resolution of the reconstructed focal activations in the cerebral tissue, the effect of superficial signal contamination is still a major problem and is addressed in detail in Chapter 5.

2.6. Conclusions

The propagation of near-infrared light inside a scattering medium such as a biological tissue has been explained, along with the different types of near-infrared systems utilized based on their detection mode. The inverse problem of the recovery of tissue parameters based on the measured data-type following a propagation model is elaborated through analytical methods and computational methods of recovery.

The non-uniqueness observed in the CW-NIRS parameter recovery methods i.e., the inability to separate the absorption and scattering dependency with the current methodology is explained as this can especially affect the estimated values of tissue oxygenation. Due to the presence of tissue under study (the brain) inside a highly scattering box (skin + skull) any information coming from cerebral tissue is inherently contaminated with superficial signal. The spatially resolved approach of SRS method is explained, which utilizes the spatial derivative of attenuation to achieve a measurement quantity that is more sensitivity to deeper tissue and therefore reducing the superficial contamination. Signal regression methods are introduced that are vastly used in many dynamic imaging or spectroscopy studies, to measure the changes in haemodynamic activity to improve the image reconstruction. Based on this premise, the following chapter will elaborately explain the method to tackle these key challenges that are listed in the previous section, with the aim of addressing the hypotheses listed in section 1.4.

Chapter 3

SPECTRALLY CONSTRAINED SPATIALLY RESOLVED SPECTROSCOPY

3.1. Introduction

Spatially resolved spectroscopy (SRS) is a widely-used technique in CW-NIRS to obtain TOI from deep tissues. While the design setup of the SRS method provides an advantage of minimal superficial layer contamination, the assumption of the scattering properties of the tissue leads to uncertainty in the estimated TOI values. While the assumed value of scattering property is based on average empirical data corresponding to the specific tissue-type, the variation of scattering properties for different tissue types across different subjects is quite significant, with about 29% variation in forearm, 7% in head and 14% in calf (66). The more the underlying scattering properties differ from the assumed values, the greater the error between ground-truth and estimated TOI values.

The aim of this chapter, is to address superficial layer contamination in the estimation of TOI by further developing the multi-distance SRS technique, but at the same time to also account for the unknown scattering properties of the underlying tissue to remove any uncertainty due to inter-subject variability in scattering properties.

3.2. Methodology

The solution to the CW diffusion equation for a homogeneous semi-infinite medium is given by, (51)

$$I = \frac{I_0}{2\pi\mu_s'\rho^2}\left[\sqrt{3\mu_a\mu_s'} + \frac{1}{\rho}\right]\exp(-\rho\sqrt{3\mu_a\mu_s'}) \tag{3.1}$$

This equation describes the intensity of (back-scattered) light (I) for a source intensity I_0, measured at a distance $\rho \gg 1/\mu_s'$ from source, in terms of optical properties of the medium. Here, μ_a and μ_s' are the bulk absorption and reduced scattering coefficients of the medium. For the case of a homogeneous medium, this equation is widely used to derive the absorption of the medium from multi-distance intensity (or attenuation) measurements.(72, 73) However, in the case of a complex multi-layered medium such as the human head, this relation becomes inappropriate, as the recovery of cerebral tissue parameters will always be contaminated by the superficial layers of head, such as skin, scalp, bone and CSF (Cerebrospinal fluid). Therefore, a different formulation is derived from the same equation, that defines the gradient of light-attenuation as mentioned in equation (2.19).

The main drawback of using the intensity gradient based method is that the absorption coefficient and reduced scattering coefficient are always coupled and cannot be separated. To separate μ_a and μ_s' from the gradient measurement, Farrell et al.(72) used the additional information of reflectance measured at smaller source-detector separation to obtain μ_s', whereas

Liu et al.(74) exploited the intercept of $\log(\rho^2 I)$ vs ρ to find μ_s' and Matcher et al.(66) used time-resolved methods to find the scattering coefficient initially and assumed that the scattering properties are similar across same tissues types for all subject. These methods use an additional measure to decouple μ_a and μ_s' which would be applicable only for a homogeneous medium. But for a layered medium such as the human head, all these additional measures contain information either from the superficial layer alone or superficial and cerebral tissue combined, and would therefore limit the inherent advantage of probing the deeper layers and being less sensitive to superficial layers, as exhibited by the gradient measurement alone.

A new approach that uses intensity gradient measurements at multiple wavelengths to decouple the absorption and scattering parameters to obtain TOI is presented. Rewriting equation (3.1) in terms of scattering parameters and chromophore concentrations (C_1, C_2, C_3 … corresponding to the molar concentrations of the chromophores oxy-haemoglobin, deoxy-haemoglobin, water volume fraction and other major light-absorbing tissue constituents),

$$\frac{1}{3}\left[\frac{\Delta A(\lambda)}{\Delta\rho} - \frac{2}{\rho}\right]^2 = \mu_a(\lambda)\mu_s'(\lambda) = \left[\sum_{j=1}^{N} \varepsilon_{j,\lambda} C_j\right] a\, R(b,\lambda) \tag{3.2}$$

The absorption coefficient at a given wavelength is related to the chromophore concentrations (C_j) as: $\mu_a(\lambda) = \sum_{j=1}^{N} \varepsilon_{j,\lambda}\, C_j$; where '$\varepsilon_{j,\lambda}$' is the molar extinction coefficient of chromophore-*j* at λ (μm) wavelength and 'N' is the number of chromophores contributing to absorption of light at the measured wavelengths.

The dependency of the reduced scattering coefficient on wavelength can also be represented as, $\mu_s'(\lambda) = a.R(b,\lambda)$ Considering all the scattering particles to be spherical, elastic and of similar size,(27) the Mie theory approximation fits well for the exponential relation as given by,(28)

$$R(b,\lambda) = (\lambda)^{-b} \tag{3.3}$$

Due to the practical inhomogeneity in the size, density and type of scattering particles in a tissue, the exponential relation may not be able to accurately represent the scattering spectrum of a tissue. Alternatively, a linear approximation of the variation of μ_s' with respect to wavelength can be used to yield an alternative representation of scattering spectrum,(52, 66) which can be expressed as:

$$R(b,\lambda) = 1 - b\lambda \tag{3.4}$$

Similar to equation (3.1) the chromophore concentrations (C_j) and the scattering parameter 'a' are coupled and would lead to infinitely many solutions. Therefore, with the normalized chromophore concentrations defined as $C_j' = a\ C_j$, equation (3.2) can be re-written as:

$$\frac{1}{3}\left[\frac{\Delta A(\lambda)}{\Delta\rho}-\frac{2}{\rho}\right]^2=\left[\sum_{j=1}^{N}\varepsilon_{j,\lambda}C'_j\right]R(b,\lambda) \tag{3.5}$$

Considering the left-hand-side term of equation (3.5) to be $\gamma(\lambda)$, the known measurements are $\gamma(\lambda_1)$, $\gamma(\lambda_2)$ … $\gamma(\lambda_N)$ at multiple wavelengths and the unknown parameter set ($\mathbf{p}$) to be recovered is: $\{b, C'_1, C'_2,\ldots C'_N\}$. Ideally at least $N+1$ wavelengths are required to solve for these $N+1$ unknowns (N normalized chromophore concentrations and 1 scattering parameter). The inverse problem of solving this non-linear equation is implemented by an iterative regularized least-square minimization with the following update equation for each iteration,(43)

$$\Delta\mathbf{p}=(\mathbf{J}^T\mathbf{J}+\alpha\mathbf{I})^{-1}\mathbf{J}^{\mathrm{T}}\Delta\boldsymbol{\gamma} \tag{3.6}$$

Here, $\Delta\mathbf{p}$ represents the update for the parameter set $\{b, C'_1, C'_2,\ldots C'_N\}$, $\Delta\boldsymbol{\gamma}$ is the measured and modelled data (calculated using equation (3.5)) misfit at the end of each iteration and $\mathbf{J}$ is the Jacobian (or sensitivity) matrix with its structure is given by,

$$\mathbf{J}=\begin{bmatrix}\frac{\partial\gamma(\lambda_1)}{\partial C'_1} & \frac{\partial\gamma(\lambda_1)}{\partial C'_2} & \cdots & \frac{\partial\gamma(\lambda_1)}{\partial b}\\ \frac{\partial\gamma(\lambda_2)}{\partial C'_1} & \frac{\partial\gamma(\lambda_2)}{\partial C'_2} & \cdots & \frac{\partial\gamma(\lambda_2)}{\partial b}\\ \vdots & \vdots & \vdots & \vdots\end{bmatrix} \tag{3.7}$$

The stability of the inverse problem relies on the condition number of the matrix **J** which varies with the values of the parameters given by $\mathbf{p}$. The condition number directly relates to the amount of information available for parameter recovery: The higher the condition number corresponds to larger instability and therefore a lower condition number is desired. To further aid the ill-conditioned problem, the inverse problem is guided with a regularization parameter given by α. The Jacobian matrix can be computed using the perturbation method on equation (3.5) and as this is an analytical expression, the whole process of the inverse problem can be accomplished in real-time.

Once the parameter set $\mathbf{p}$ is recovered, the tissue oxygenation index (TOI) can then be calculated from the normalized oxy haemoglobin concentration (C_1') and normalized deoxy haemoglobin concentration (C_2') as, $\mathrm{TOI}\ (\%) = 100 \times C_1'/(C_1' + C_2')$. This algorithm is defined as Spectrally Constrained Spatially Resolved Spectroscopy (SCSRS).

3.3. Optimization of wavelengths

The stability of the inverse problem relies on the condition number of the sensitivity matrix (**J**). Lower condition number implies a good recoverability of parameters, with low cross-talk. Remembering that $\mu_a(\lambda) = \sum_{j=1}^{N} \varepsilon_{j,\lambda}\, C_j$, the distinguishability of oxy-haemoglobin and deoxy-haemoglobin should also be taken into account and it depends on the extinction coefficient matrix ($\mathbf{E}$) given by,(64)

$$\mathbf{E} = \begin{bmatrix} \varepsilon_{1,\lambda_1} & \varepsilon_{2,\lambda_1} \\ \varepsilon_{1,\lambda_2} & \varepsilon_{2,\lambda_2} \\ \vdots & \vdots \end{bmatrix} \tag{3.8}$$

Here, ε_1 and ε_2 represent the extinction coefficients of oxy-haemoglobin and deoxy haemoglobin respectively. In this work, the recovery of just two chromophores oxy and deoxy-haemoglobin is considered i.e., $N = 2$ and therefore the three optimal wavelengths to implement this algorithm are sought. To this end, different combinations of a set of 3 wavelengths are considered from the spectra 650 to 850 nm with 4 nm separation. The wavelength range is limited from 650 to 850 nm to avoid the peak absorption wavelengths for water and lipids, so that oxy and deoxy haemoglobin remain as the major chromophores contributing to light absorption in this wavelength region. The condition numbers of $\mathbf{E}$ and $\mathbf{J}$ are calculated for different combinations of wavelengths as shown in Figure 3.1 and Figure 3.2. The highlighted region shows the combinations with low condition number of $\mathbf{E}$ (<5.3) and low condition number of $\mathbf{J}$ (<250).

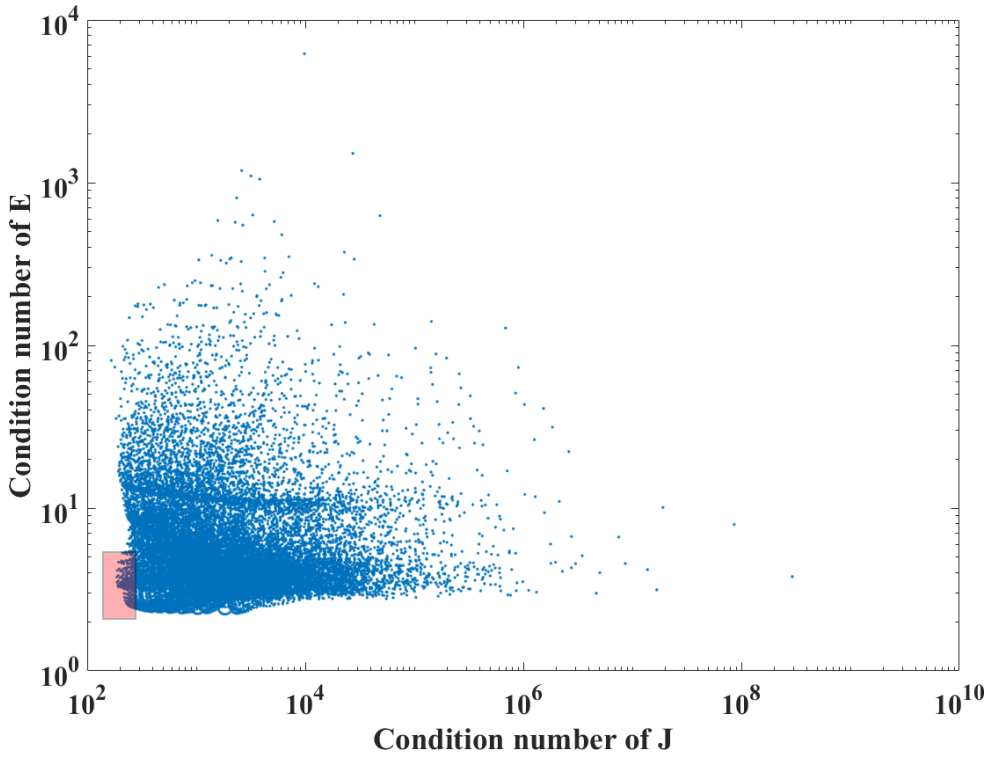

Figure 3.1. Scatter plot of condition numbers calculated for E and J with exponential scattering model.

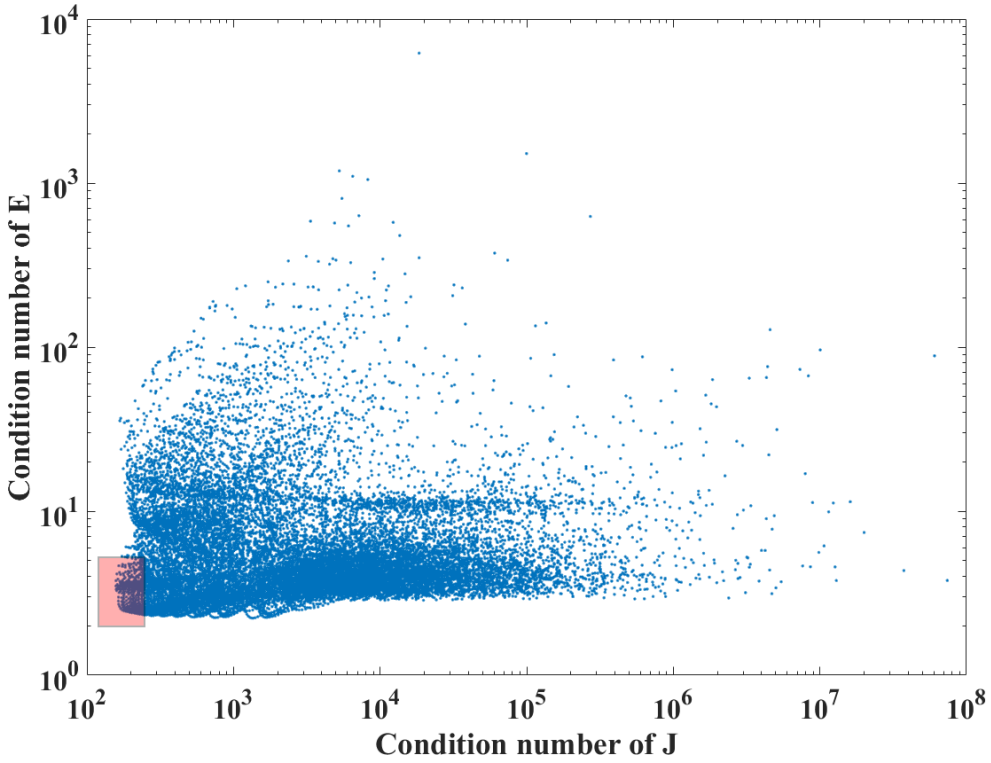

Figure 3.2 Scatter plot of condition numbers calculated for E and J with linear scattering model.

The histograms of optimized wavelength sets that satisfy this low condition number criterion are shown in Figure 3.3 and Figure 3.4. The optimal three wavelengths for the exponential scattering model are 744 ± 23, 805 ± 7 and 848 ± 2 nm. Similarly, the optimal wavelengths for the linear scattering model are found to be 734 ± 25, 805 ± 6 and 848 ± 2 nm, demonstrating that the optimal wavelengths for both models seem to be similar. Given that we are only recovering oxy and deoxy haemoglobin, and given the large difference in their extinction coefficients at lower wavelengths, this gives rise to the wide distribution at lower wavelengths. The condition number for any set of three wavelengths within this distribution has minimal variation.

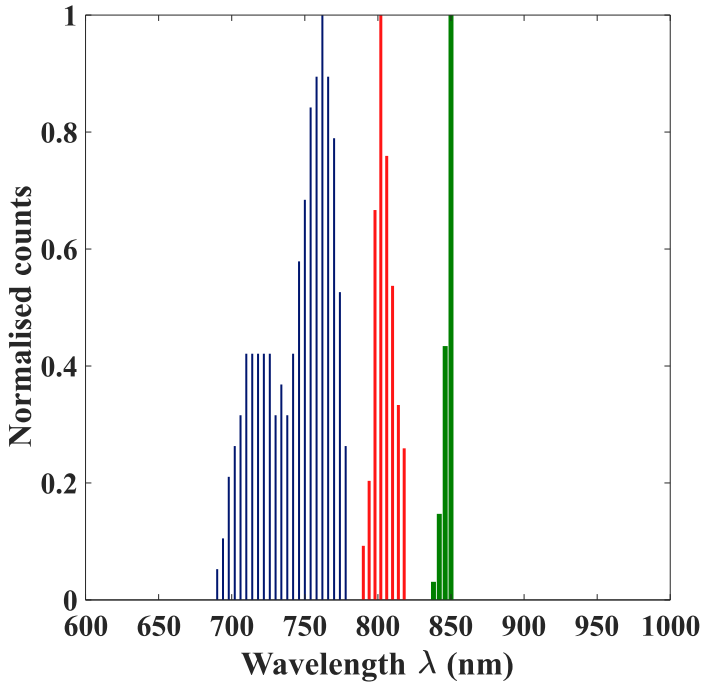

Figure 3.3. Normalized histogram of optimal wavelengths that satisfy the low condition number criterion for exponential scattering model.

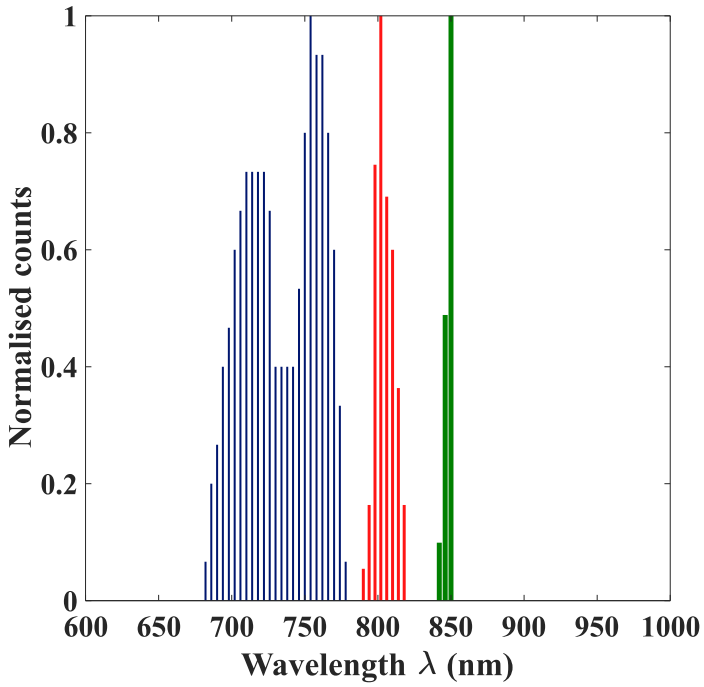

Figure 3.4. Normalized histogram of optimal wavelengths that satisfy the low condition number criterion for linear scattering model.

3.4. Numerical validation on head model

MRIs of 10 different subjects are used to build different head models. One source and two detectors (37 and 43 mm from the source) are placed on the forehead as shown in Figure 3.5, operating at wavelengths 735, 810, 850 nm; this probe model is similar to the commercially available NIRO-200NX and these wavelengths combination fall within the optimal wavelength set derived in the previous section. Using the baseline properties given in Table 3.1, the transmitted light intensity data is simulated on NIRFAST. The scatter amplitude and scatter power for three regions shown in Table 3.1 are randomly distributed around the baseline value by +/-30% to

account for inter-subject variability. Two cases are examined here for data simulation: A) the medium is assumed to be homogeneous with optical properties of brain to account for zero superficial layer contamination, B) the medium is considered as a heterogeneous three layered model as shown in Figure 3.5 to study a more realistic case. The 10 head models have an average skin thickness of 5 mm and skull thickness of 8 mm.

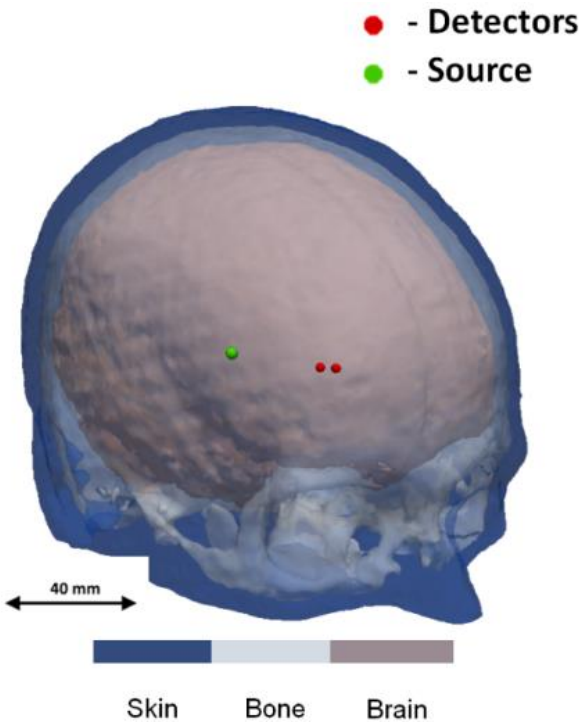

Figure 3.5. Probe locations shown on a 3-layered model of human head.

Table 3.1. Baseline tissue optical parameters.(65, 75)

Parameter↓	Region→	**Skin**	**Bone**	**Brain**
Total haemoglobin (mM)		0.07	0.049	0.076
Tissue oxygenation index (%)		80	80	50 to 80
Scatter Power		1.42	0.72	1.61
Scatter Amplitude (mm^{-1})		1.72	1.40	0.80

The regularization parameter α for the inverse problem as shown in equation (3.6) is considered as 0.01 times the maximum diagonal value of $\mathbf{J}^{\mathbf{T}}\mathbf{J}$. The recovered TOI values are shown in Figure 3.6 and Figure 3.7 for the proposed SCSRS (for both exponential and linear scatter model) method as well as those with the regular spatially resolved spectroscopy (SRS), as defined elsewhere (52) with the error in the estimation of cerebral TOI values shown in Figure 3.8. For the conventional SRS method, equation (3.5) is used in combination with the linear scatter model described in equation (3.4), along with $b = 0.63\ \mu\mathrm{m}^{-1}$ as is typically chosen to represent brain tissue (52). With the assumption of b parameter, equation (3.5) becomes a simple linear equation in $\{C_1', C_2'\}$ and can be solved to recover TOI.

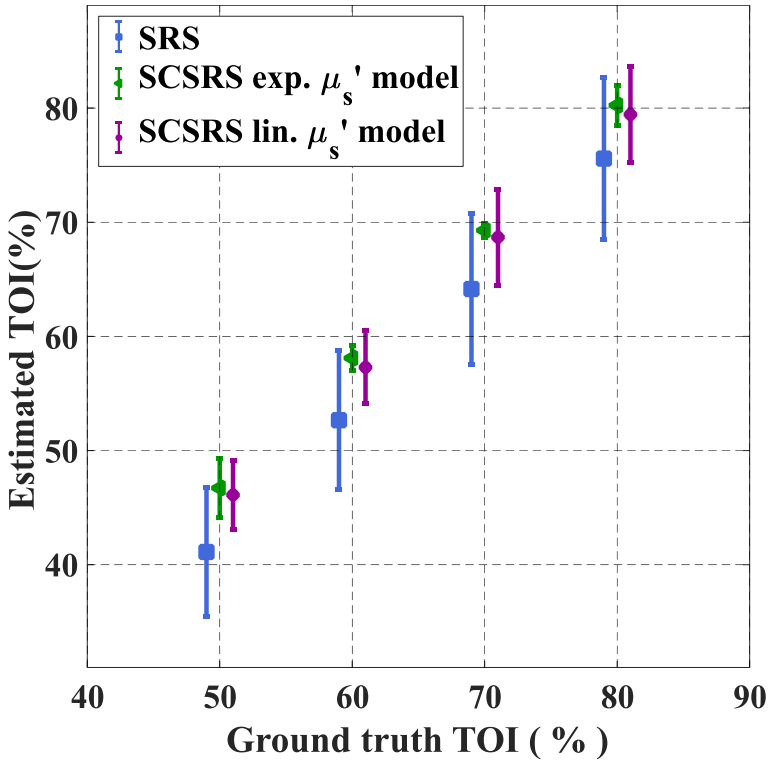

Figure 3.6. Recovered TOI values of the brain with standard-deviation of recovery across 10 head models with homogenous optical properties, using both exponential (exp.) and linear (lin.) scattering models.

Figure 3.6, Figure 3.7 and Figure 3.8 show that for both homogeneous and layered head scenarios, SCSRS method has higher accuracy in recovering the cerebral TOI with a maximum third quartile (75th percentile) error of ±5.7% for the linear scatter model (±6.7% for exponential scatter model), compared to that of ±12.3% for SRS method, showing an improvement of 6.6% in the estimation error. The lower errors of SCSRS with exponential scatter model for homogeneous head scenario are due to the inverse crime of using the exponential scatter model to simulate the data and recover the parameters as well. However, for the 3-layered head scenario this advantage is absent due to the inhomogeneity in the scattering properties of the medium, and the homogeneous approximation (since SCSRS in based on a homogeneous model)

of a linear scatter model performed better than the exponential scatter model. The recovered values of *b* parameter in SCSRS method corresponding to the linear scatter model is shown in Figure 3.9 and Figure 3.10 corresponding to homogeneous and 3-layered head scenarios respectively, for all varying modelled TOI values, in comparison to the ground-truth values and also the constant approximated b value of 0.63 μm^{-1} in SRS method. It should be noted that the ground-truth scatter model used in simulations is the exponential model, and the values shown in Figure 3.9 and Figure 3.10 correspond to a linear approximation to the exponential model. This clearly demonstrates the variation in the best-fit 'b' parameter across different subject models of different scattering properties.

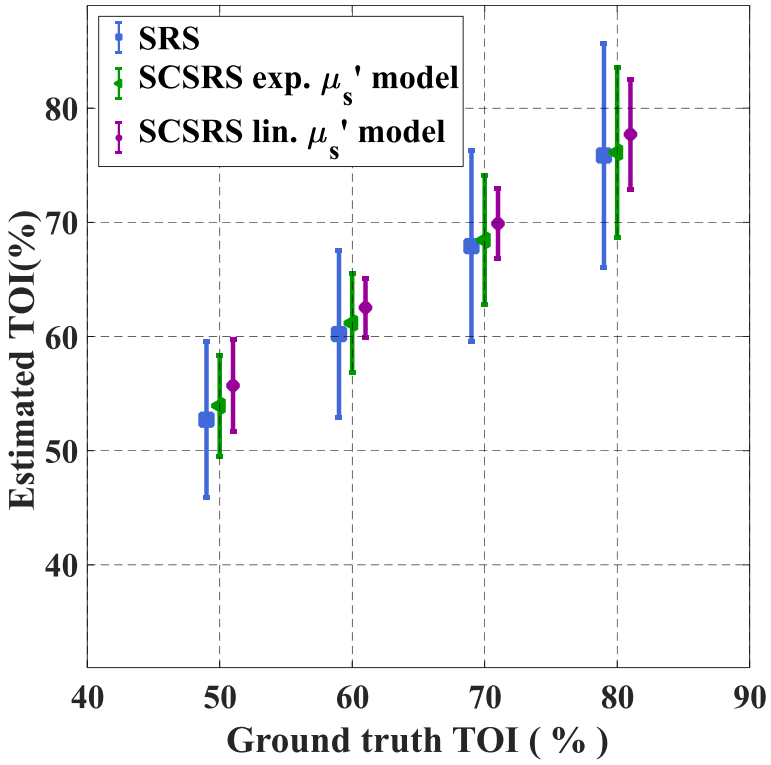

Figure 3.7. Recovered TOI values of the brain with standard-deviation of recovery across 10 head models of three-layered optical properties, using both exponential (exp.) and linear (lin.) scattering models.

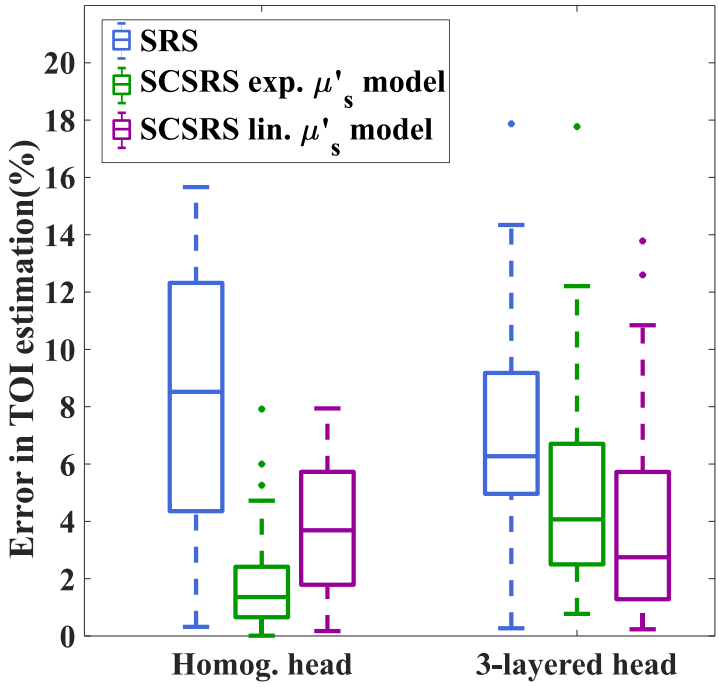

Figure 3.8. Box-plot of absolute error in the estimation of TOI, showing the distribution of errors across different ground-truth TOI and scattering parameters for, homogeneous and three-layered head model.

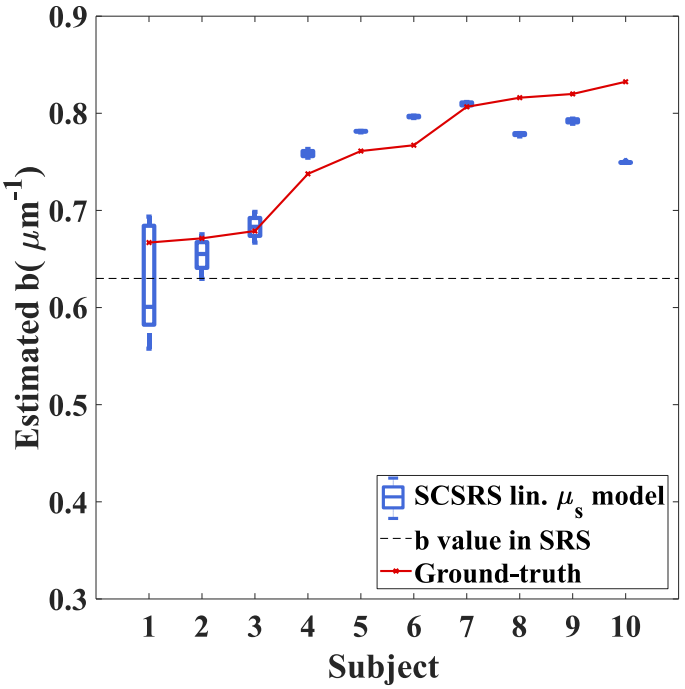

Figure 3.9. Recovered *b*-value (corresponding to linear scattering model) with SCSRS for homogeneous head models, of 10 different subjects with different scattering parameters. The boxplot shows the distribution of recovered '*b*' for different cerebral TOIs (50 to 80%). The solid line represents the ground-truth values of the homogenous medium. The dotted line marks the value assumed in SRS method.

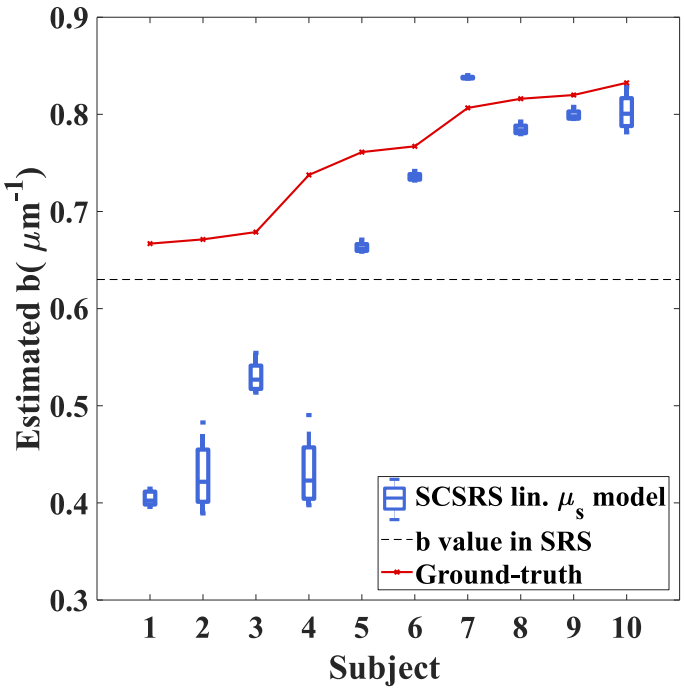

Figure 3.10. Recovered *b*-value (corresponding to linear scattering model) with SCSRS for 3-layered head models, of 10 different subjects with different scattering parameters. The boxplot shows the distribution of recovered '*b*' for different cerebral TOIs (50 to 80%). The solid line represents the ground-truth values of the cerebral region. The dotted line marks the value assumed in SRS method.

3.5. Effect of superficial layer thickness

Although the recovered brain TOI values using this proposed gradient based method are shown to be less sensitive to variations in scattering, their accuracy in the recovery of cerebral tissue parameters is limited due to the heterogeneous layered nature of the head. Here the effect of superficial layer thickness in determining cerebral TOI is demonstrated using the proposed SCSRS method and compared to the conventional SRS.

To simulate the effect of different tissue thicknesses, a rectangular-slab FEM model (200×100×100 mm^3) of mean element size of 0.7 mm^3, is considered with three layers

corresponding to the three layers of human head: skin, skull and brain. The sum of skin and skull thickness is varied from 0 to 14 mm in steps of 2 mm to simulate possible tissue thicknesses from an infant head to an adult head while the ratio of skin to skull thickness is maintained 5:8 in accordance with the average thickness of real head models considered in section 3.4.(76) Using the medium properties as defined in Table 3.1, the transmitted light intensity data is simulated on NIRFAST. The modelled measurement system is similar to the one considered in previous section with one source and two detectors (37 and 43 mm from the source) at 735, 810 and 850 nm wavelengths. To account for the inter-subject variability the data is simulated for 30 different cases with scattering properties randomly varied around the baseline values given in Table 3.1, by a standard deviation of 30% and TOI values of brain region is changed from 50% to 80%. The recovery of tissue oxygenation is shown in Figure 3.11 for different possible superficial layer thicknesses along with the error plots shown in Figure 3.12. The conventional SRS method is implemented using a linear scatter model with $b = 0.63\ \mu\text{m}^{-1}$ corresponding to an adult head.

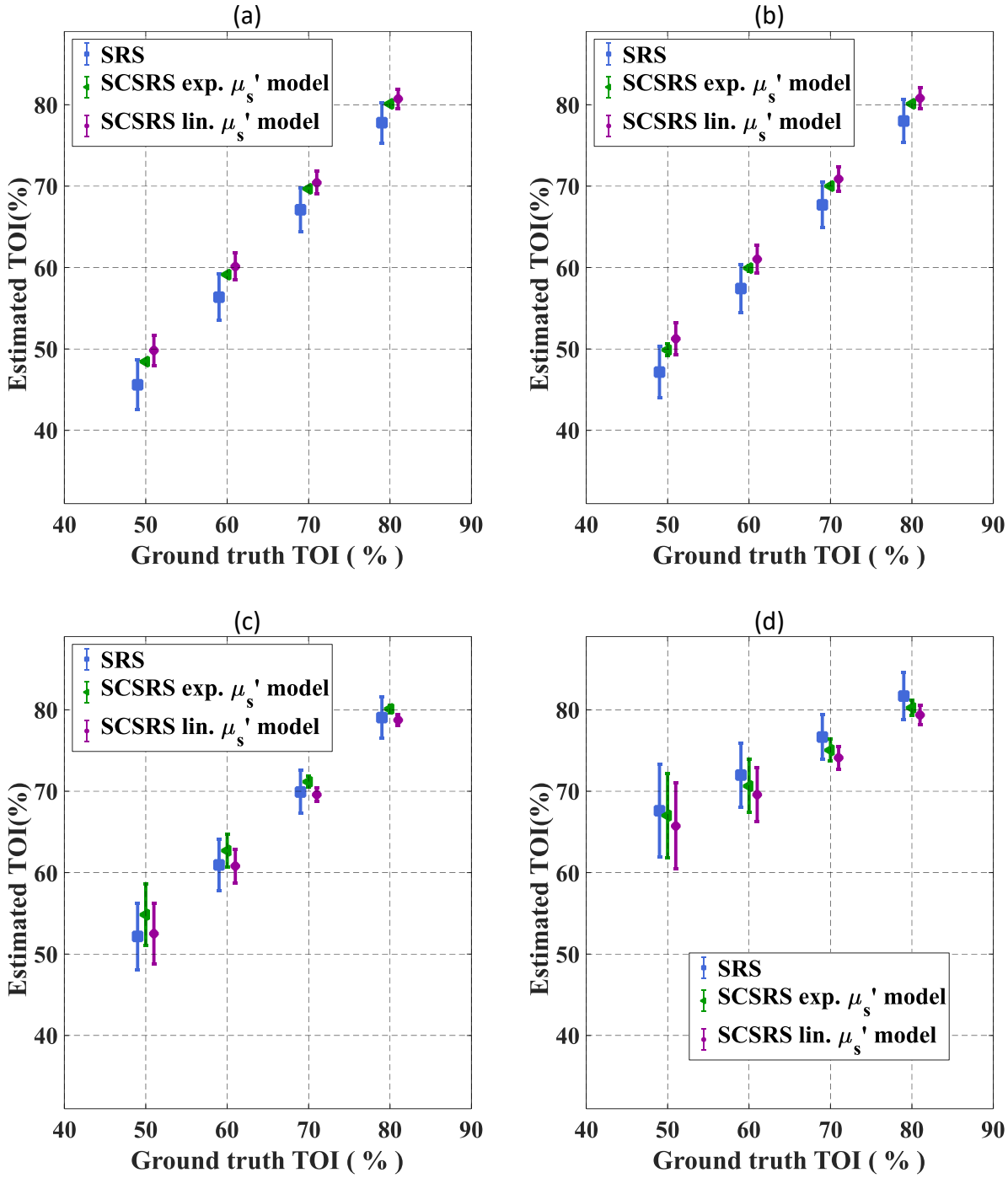

Figure 3.11. Recovered TOI values with standard-deviation of recovery across 30 different cases of randomly varying scattering properties, for a skin + skull thickness of (A) 0 mm, (B) 4 mm, (C) 8 mm and (D) 14 mm.

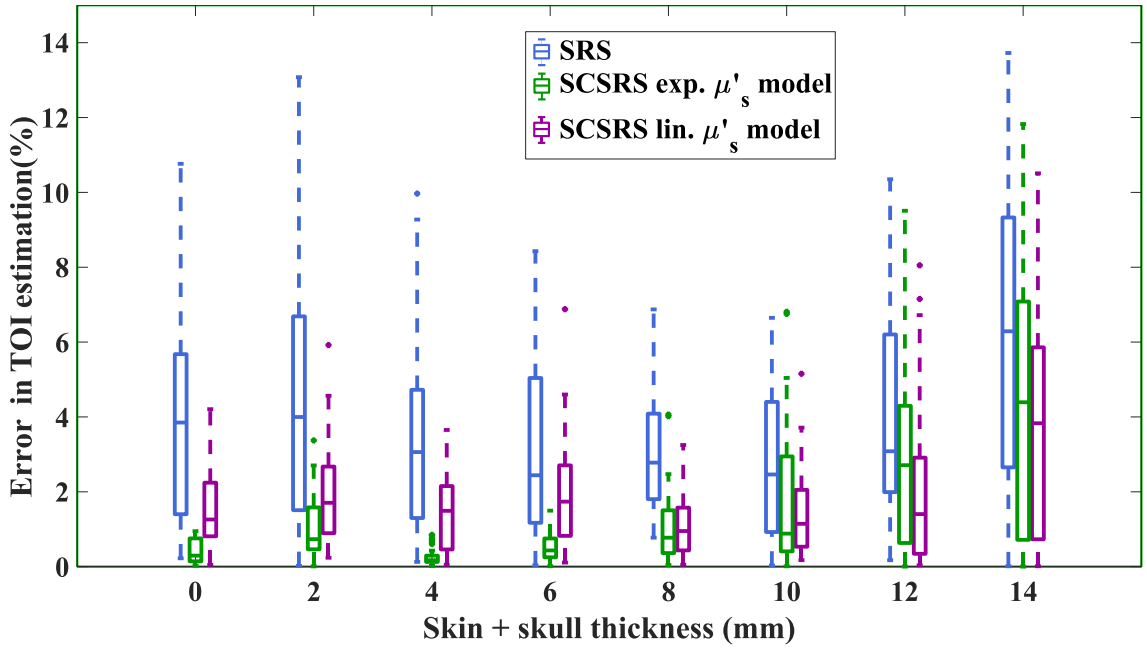

Figure 3.12. Boxplot of absolute error in the estimation of TOI for different skin + skull thicknesses, showing its distribution across different ground-truth TOI and scattering parameters.

For a homogeneous medium (i.e. skin + skull thickness = 0 mm), the SCSRS method with both scattering models exhibit a mean error of less than 2% out-performing the SRS method which results in errors up to 6%. The lower errors for the SCSRS with exponential scattering model as compared to the linear scattering model is to be attributed to the fact that the data was simulated using exponential scattering model and this advantage seems to be prevalent only up to a superficial layer thickness of 8 mm where the inhomogeneity starts to dominate. The decrease in overall mean errors in TOI estimation for superficial thickness 4 and 6 mm is due to the higher TOI values of superficial layer. It can be seen from Figure 3.11 that as the superficial layer thickness increases from 0 to 14 mm, the estimated cerebral mean TOI at lower ground truth values demonstrate a minor underestimation at 0 mm superficial layer thickness i.e., homogenous scenario (similar to the head-model results observed in Figure 3.6) which can be attributed to the cross-talk with recovered scattering parameter and tend to move towards the

TOI of the superficial layers (80%, shown in Table 3.1) at higher superficial layer thicknesses, which is an overestimation (similar to head-model results observed in Figure 3.7) for cerebral TOI of low ground-truth values. This shift from negative (underestimation) to positive (overestimation) errors at low ground-truth TOI as we move from 0 to 14 mm, causes the absolute errors to reach lower values, which is seen to be happening at superficial layer thicknesses of 4 and 6 mm in Figure 3.11. At higher thicknesses of superficial layers the mean TOI recovery tends to be inaccurate and the recovery errors for SCSRS increase up to 7.7% with an exponential scattering model and 5.8% with a linear scattering model, which are still lower than a recovery error of 9.3% using conventional SRS. All the quantitative errors quoted above are the 75th percentile errors from Figure 3.12. These results demonstrate that the proposed method of SCSRS, with both exponential scatter model and linear scatter model, performs better than the conventional SRS.

3.6. Arm-cuff validation

The proposed SCSRS method is tested on experimental data from forearm occlusion experiment (institutional ethical approval: ERN16-1490) using a commercial CW-system, the NIRO-200NX. The probes were attached to both forearms of a human subject and a blood pressure cuff was applied on the upper arm with the cuff inflated to 140 mmHg for 60s to observe arterial occlusion. The conventional SRS is also implemented (linear μ_s' model: $b = 0.47\ \mu\mathrm{m}^{-1}$ corresponding an adult forearm(77)) to compare the results with SCSRS, Figure 3.13. Both methods show a similar trend in the changes of recovered TOI, but the absolute values differ by more than 10%.

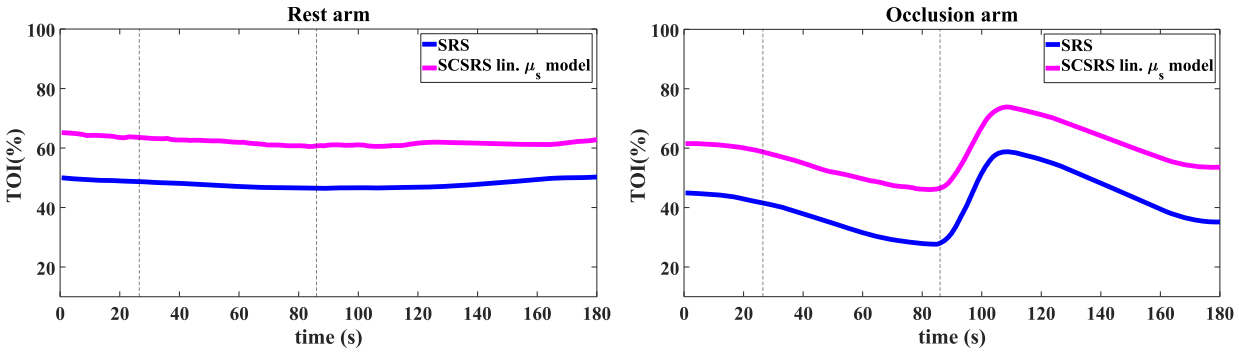

Figure 3.13. TOI measurement on human forearm: Rest arm recovered b-value from SCRS is 0.79±0.007 μm^{-1}, and Occlusion arm recovered b-value from SCSRS is 0.82±0.003 μm^{-1}.

The recovered values of 'b' with SCSRS were 0.79±0.007 μm^{-1} and 0.82±0.003 μm^{-1} for each arm respectively. Although these are similar for each arm, they are different as compared to the average literature value of 0.47 μm^{-1} (as used for SRS algorithm) (77). Since the variation in the 'b' parameter across different subjects and tissues can be large (66, 77), the proposed SCSRS method overcomes this by fitting for this 'b' parameter and simultaneously recovering the TOI using the optimal wavelengths. Finally, although the proposed algorithm provides a TOI which is higher than the SRS method, this is likely to be more accurate based on results in Figure 3.11, where the SRS always under-estimates the TOI.

3.7. Discussion

It is shown that the SCSRS method which is based on gradient of light of attenuation measurement is less sensitive to superficial region and more sensitive to deeper tissues. Although the superficial layer contamination is shown to be minimized using the gradient measurement,

the error due to the heterogeneity of a layered medium still exists and is shown to cause an underestimation of the recovered TOI values of the brain.

The parameter recovery involves inversion of a Jacobian matrix, for which an optimal set of wavelengths (734 ± 25, 805 ± 6 and 848 ± 2 nm) have been found to maximize the information present while minimizing the crosstalk between parameters. This is similar to previous wavelength optimization work done by Eames et al. (64) where they recovered optimal wavelengths which were also based on normalization of the absorption by the scattering properties (i.e. an assumed pathlength). It should however be noted that central wavelengths of interest are always a function of the absorption parameters being recovered and although the methodology can be generalized this should be repeated for each specific application under investigation.

The inter-subject variability in the scattering properties is known to be significant, which has been identified through findings in other works (66, 77). Therefore, any assumption of the scattering properties for the estimation of absorbing properties such as the tissue oxygenation would result in an uncertain estimation, which is the case with SRS. The feasibility of the proposed SCSRS approach is shown to measure the deep layer tissue oxygenation with higher accuracy (average recovery errors of <5%) by simultaneously fitting the scattering parameters for adult head geometries. The repeatability (low variation) of recovered scattering parameters for different cerebral TOIs (50 to 80%) on the same subject, as shown in Figure 3.9 and Figure 3.10, demonstrates that the cross-talk between the recovered parameters is low which can be attributed to the wavelength optimization. A variation of TOI from 50% to 80% in the brain is considered as safe (78) and beyond which it is regarded as cerebral hypoxia (79), in which case

clinical intervention is opted, therefore these range of practical extreme values are considered for this work and the subsequent work in the next chapter.

3.8. Conclusions

A methodology of SCSRS is demonstrated to yield more accurate results of TOI estimates than a conventional SRS without any prior assumptions on the value of tissue scattering coefficient, therefore being independent of the subject and tissue-type. The key advantage of this method is that it is compatible with the commercially available devices such as NIRO-200NX without any additional instrumentational changes. The use of analytical equation for modelling data for the inverse problem makes the method computationally less expensive.

However, the major limitation of the method being that it is based on a homogenous model. For tissue types where a local homogeneity can be expected (to some degree in the measurement-sensitive region) this is not a major issue, but for tissue-type such as head, where a layered heterogeneity is inherent, the accuracy of the method decreases as the difference between tissue properties of the layers increases which is also clearly demonstrated in this simulation study. While the proposed method still outperforms the conventional SRS in a heterogenous scenario, there is still a necessity for a NIRS parameter recovery method that considers the heterogenous nature of the medium in its recovery model. This forms the basis idea for the work presented in the next chapter.

Chapter 4

RECOVERY OF CEREBRAL AND EXTRA-CEREBRAL TISSUE PARAMETERS USING BROADBAND INTENSITY DATA

4.1. Introduction

The aim of this chapter is to address the non-uniqueness in CW NIRS systems to retrieve both absorption and scattering properties of the cerebral tissue while also accounting for the heterogenous nature of the problem. The parameters of interest are mainly haemoglobin concentration and tissue oxygenation index. While most of the parameter recovery algorithms of CW systems assume a homogenous tissue for the investigated region (42), the inherent heterogenous or layered nature of the tissue can lead to quantification errors. Multi-distance algorithms have been proposed using gradient of intensity attenuation measurements (51, 52, 66) based on a flat semi-infinite homogenous model. Since the gradient is more sensitive to deeper regions than raw intensity as shown in earlier chapters, this makes the recovered parameters less sensitive to changes in extra-cerebral tissue. However, the accuracy of the recovered cerebral tissue parameters still remains low due to the homogenous approximation of the head and due to the curvature and complex internal structure of the head. The assumption of scattering properties of the tissue is another source of error in these gradient-based algorithms. The uncertainty due to scatter approximation has been investigated and an alternative method was proposed in Chapter 3 to recover scattering parameters and scaled

haemoglobin concentrations for a more accurate estimate of tissue oxygenation. Other works that are aimed at the removal of signal contamination due to extra-cerebral layer include: signal regression-based methods (68, 69) for recovering changes rather than absolute values. Frequency domain-based methods (35, 45) have been proposed that can recover both absorption and scattering properties of extra-cerebral and cerebral tissues along with the thickness of the top layer. In CW-based methods however, phantom studies on a two layered model have been studied with a known superficial layer thickness (80). The work reported to date has relied on spectral and spatial derivative measurements, where a theoretical non-uniqueness is unavoidable (as detailed in later sections). The unknown superficial layer thickness, and the performance of a two-layered model in a realistic scenario with oxy and deoxy-haemoglobin as the primary absorption constituents remains unexplored. This is a crucial point to address since the spectral characteristics play a major role in distinguishing the tissue parameters in any recovery algorithm.

With no constraint on the spatial distribution of the optical properties, it has been shown (61) that there can be more than one solutions to the CW diffusion equation and with optimal choice of wavelengths this non-uniqueness can be avoided by spectrally constraining the parameter recovery process (63). In this work, the uniqueness/non-uniqueness problem of a CW system in the context of a layered medium is addressed, by assuming regional homogeneity; it is shown that the solution set is unique if the measured boundary data is intensity-based only. Based on this a two-layered parameter recovery approach is defined for a multi-distance continuous wave broadband system, to recover the tissue parameters of two layers corresponding to cerebral and extra-cerebral regions as well as the superficial tissue thickness.

The study is divided into three parts, the first part deals with data simulated and parameter recovery using the two-layered semi-infinite model, second part deals with data simulated on two-layered head model but the parameter recovery is implemented using two-layered semi-infinite model, third part deals with data simulated on two-layered head model and parameter recovery is also based on a head model. The proposed method is then implemented and used to recover the cerebral and extra-cerebral tissue parameters of a human subject by measuring NIRS data on the forehead to demonstrate the practical viability of the approach.

4.2. Continuous wave data and uniqueness in parameter recovery

Uniqueness/non-uniqueness problem in the parameter recovery methods of CW based systems has been a long-discussed topic (61, 63) and has been shown that for a single wavelength multi-distance boundary intensity measurements there can be more than one solutions of absorption and reduced scattering coefficient distributions which will lead to the same boundary data. This non-uniqueness can be addressed by using multi-wavelength data and constraining the problem spectrally (63). The reported findings to date discuss a very general scenario of image reconstruction where the recovered parameters are the three-dimensional distribution of absorption and reduced scattering coefficients. However, in the context of finding the absolute parameters of different regions in a layered medium such as the human head, this presented work brings an additional spatial constraint to the distribution of parameters. Here, by extending the arguments made in previous works (61, 63) it is shown that given such a regional constraint on parameters, each solution set is unique to a measured boundary intensity data, and also investigates the scenario when the measured data is either a spatial or 1^{st} spectral derivative of intensity (in log scale).

Consider the following schematic of a two-layered medium as shown in Figure 4.1.

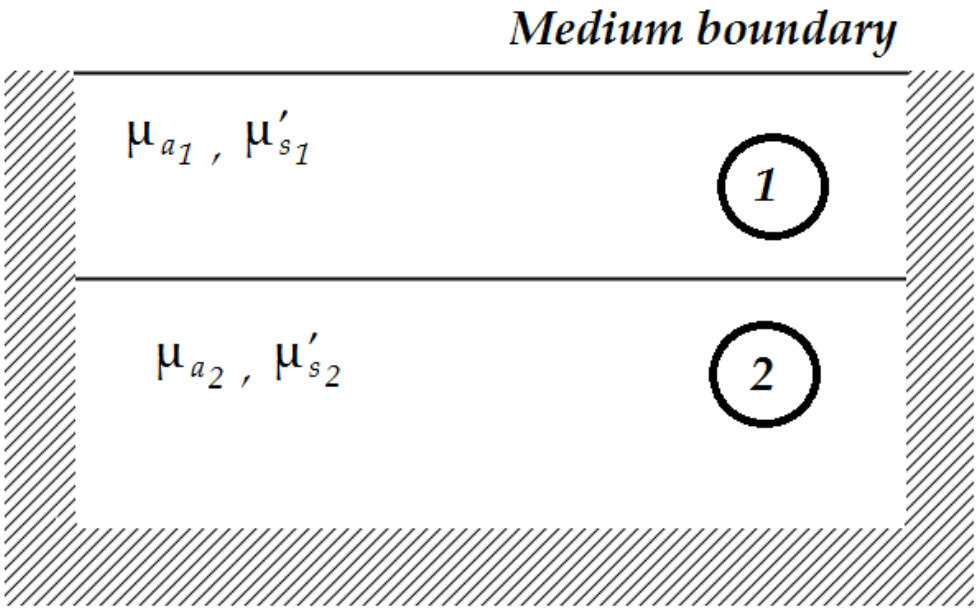

Figure 4.1. Schematic showing a two-layered medium

Here, μ_a is the absorption coefficient, μ_s' is the reduced scattering coefficient, and the diffusion coefficient (κ) is defined as, $\kappa = 1/3(\mu_a + \mu_s') \approx 1/3\mu_s'$. Re-writing the CW diffusion approximation given in equation (2.7) by change of variables to get the Helmholtz-type equation given as (61),

$$-\nabla^2\Psi + \eta\Psi = \frac{q_0}{\gamma} \tag{4.1}$$

where $\gamma^2 = \kappa$, q_0 is the source distribution, $\Psi = \gamma\Phi$, where Φ is the photon density, and the variable η is given by,

$$\eta = \frac{\nabla^2 \gamma}{\gamma} + \frac{\mu_a}{\gamma^2} \tag{4.2}$$

Considering the light-source to be a point source at a location $\mathbf{r}_0$ on the external medium boundary, and defining Ψ_0 such that:

$$-\nabla^2 \Psi_0 + \eta \Psi_0 = \mathrm{q}_0 \tag{4.3}$$

This implies that $\Psi = \Psi_0/\gamma(\mathbf{r}_0) = \Psi_0/\gamma_1$, as $\gamma(\mathbf{r}_0) = \gamma_{boundary} = \gamma_1$ in the given scenario and therefore $\Phi_{\mathrm{boundary}} = \Psi_{0_{boundary}}/\gamma_1^2$.

For any measured boundary intensity data Φ_{boundary}, two non-unique solution sets $\{\mu_a, \mu_s', L\}$ and $\{\tilde{\mu}_a, \tilde{\mu}_s', \tilde{L}\}$ (with their equivalent canonical parameters η and $\tilde{\eta}$), can exist if they satisfy the following two conditions:

- Condition-1: $\eta = \tilde{\eta}$ everywhere inside the medium, this ensures Ψ_0 to be the same for both solutions.
- Condition-2: $\gamma_{boundary} = \tilde{\gamma}_{boundary}$, together with condition 1 this ensures Φ_{boundary} to be the same for both solutions.

Applying condition 1, to this scenario, $\eta = \tilde{\eta}$ for region-1, region-2 and at the boundary between them. This requires the superficial layer thickness to be equal i.e., $L = \tilde{L}$, as without this the two solutions would have a different location of the interface between region-1 and region-

2, and η can never be equal to $\tilde{\eta}$ at the regional interface. Solving condition-1 inside region-1 and region-2 (i.e., $\eta_1 = \tilde{\eta}_1$ and $\eta_2 = \tilde{\eta}_2$ with $\nabla^2\gamma = 0$), we have:

$$\mu_{a_1} \cdot \mu'_{s_1} = \tilde{\mu}_{a_1} \cdot \tilde{\mu}'_{s_1} \tag{4.4}$$

$$\mu_{a_2} \cdot \mu'_{s_2} = \tilde{\mu}_{a_2} \cdot \tilde{\mu}'_{s_2} \tag{4.5}$$

At the boundary between region-1 and 2, knowing that $\nabla^2\gamma \propto (\gamma_2 - \gamma_1)$, and from equations (4.4) and (4.5):

$$\frac{\gamma_1}{\gamma_2} = \frac{\tilde{\gamma}_1}{\tilde{\gamma}_2} \Rightarrow \frac{\mu'_{s_1}}{\mu'_{s_2}} = \frac{\tilde{\mu}'_{s_1}}{\tilde{\mu}'_{s_2}} \tag{4.6}$$

Similar analysis can be extended for more than two regions if needed and therefore the solution set $\{\tilde{\mu}_a, \tilde{\mu}'_s\}$ should be of the form $\{\alpha\mu_a, \alpha^{-1}\,\mu'_s\}$ everywhere in the medium, for an arbitrary constant α. An equivalent representation of this non-uniqueness expression in terms of spectral parameters chromophore concentrations (C_{i}), scattering amplitude (Sa) and scattering power (Sp) can be shown as $\{\tilde{C}_{\mathrm{i}}, \widetilde{Sa}, \widetilde{Sp}\} = \{\alpha C_{\mathrm{i}}, \alpha^{-1}Sa, \mathrm{Sp}\}$, where these spectral parameters are related to the optical properties as follows:

$$\mu_a(\lambda) = \sum_{\mathrm{i}=1}^{N} \varepsilon_{\mathrm{i}}(\lambda) \cdot C_{\mathrm{i}} \tag{4.7}$$

$$\mu_s'(\lambda) = Sa \cdot \lambda^{-Sp} \tag{4.8}$$

Here, C_{i} denotes the concentration of the major chromophores contributing to light absorption, ε_{i} denotes the extinction coefficient of the corresponding chromophore.

Applying condition 2, $\tilde{\gamma}_{boundary} = \gamma_{boundary} \Rightarrow \tilde{\gamma}_1 = \gamma_1 \Rightarrow \tilde{\mu}_{s_1}' = \mu_{s_1}'$, this gives the value of the arbitrary constant to be $\alpha = 1$. This shows that for measured boundary intensity, the solution set is unique with the assumed regional homogeneity.

However, if the measured data is either a spatial or spectral derivative of the form $\log\left(\Phi_{\mathrm{boundary}}(\mathbf{r}_1, \lambda_1)/\Phi_{\mathrm{boundary}}(\mathbf{r}_2, \lambda_2)\right) = \log\big(\Psi_0(\mathbf{r}_1, \lambda_1) \cdot \gamma_1(\lambda_2)/\Psi_0(\mathbf{r}_2, \lambda_2) \cdot \gamma_1(\lambda_1)\big)$, any arbitrary value of the constant α leads to the same measured data, thus allowing for a non-unique solution set. In such a scenario, this non-uniqueness leads to uncertain parameter recovery, and this is seen in terms of the cross-talk between chromophore concentrations and scattering amplitude. However, biomarkers such as TOI which are based on the ratio of chromophore concentrations will still be accurate, as all the chromophore concentrations in any of the non-unique solution sets differ only by a common constant factor from true values.

To demonstrate the non-uniqueness in terms of the widely used spectral derivative of intensity data, let us consider an example of a two-layered medium with two major light-absorbing chromophores i.e., oxy-haemoglobin (its concentration denoted by HbO) and deoxy-

haemoglobin (its concentration denoted by Hb) with their layer specific values given as $\mathrm{HbO}_1 = 0.047\mathrm{mM}$, $\mathrm{HbO}_2 = 0.054\mathrm{mM}$, $\mathrm{Hb}_1 = 0.011\mathrm{mM}$, $\mathrm{Hb}_2 = 0.022\mathrm{mM}$, $\mathrm{Sa}_1 = 0.64\mathrm{mm}^{-1}$, $\mathrm{Sa}_2 = 0.98\mathrm{mm}^{-1}$, $\mathrm{Sp}_1 = 1.06$, $\mathrm{Sp}_2 = 0.611$, corresponding to layer-1 and layer-2 respectively, and L=10mm. For the source-detector distances of $\rho = 10, 20, 30, 40, 50$ mm, and wavelengths $\lambda = 650$ to 850 nm, in steps of 10 nm, the boundary intensity is simulated using NIRFAST (31), Figure 4.2 shows the spectral derivative of intensity data for two distinct parameter-sets corresponding to $\alpha = 1$ and 0.5, which are clearly coinciding with each other and their corresponding intensity data is shown in Figure 4.3.

As evident in Figure 4.2 and Figure 4.3, while the intensity data remains distinct for two different ground-truth parameters, the derivative data shows very little variation and therefore demonstrates the non-uniqueness of derivative of intensity data. Hence, in this work only the intensity data is considered as the measurement for the recovery of absolute tissue parameters. Although, uniqueness in terms of intensity data is established from above, one should remember that in a practical scenario, finite independent measurements, noise in the measured data, any mismatch in the assumed model, or the stopping criterion of an iterative fitting method algorithm, can lead to potential recovery errors.

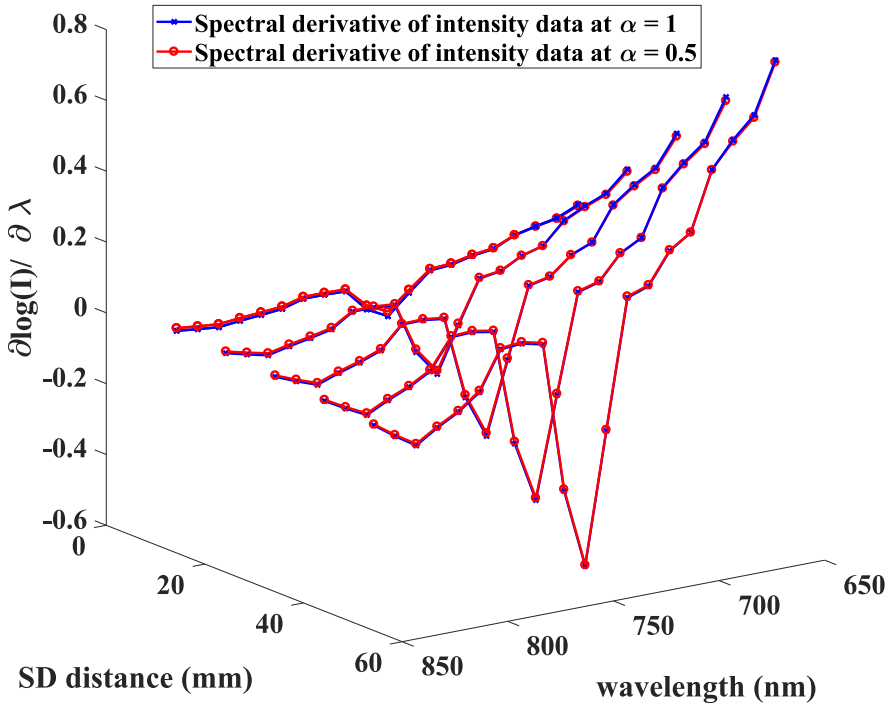

Figure 4.2. 1st Spectral derivative of intensity data at α = 1 and 0.5

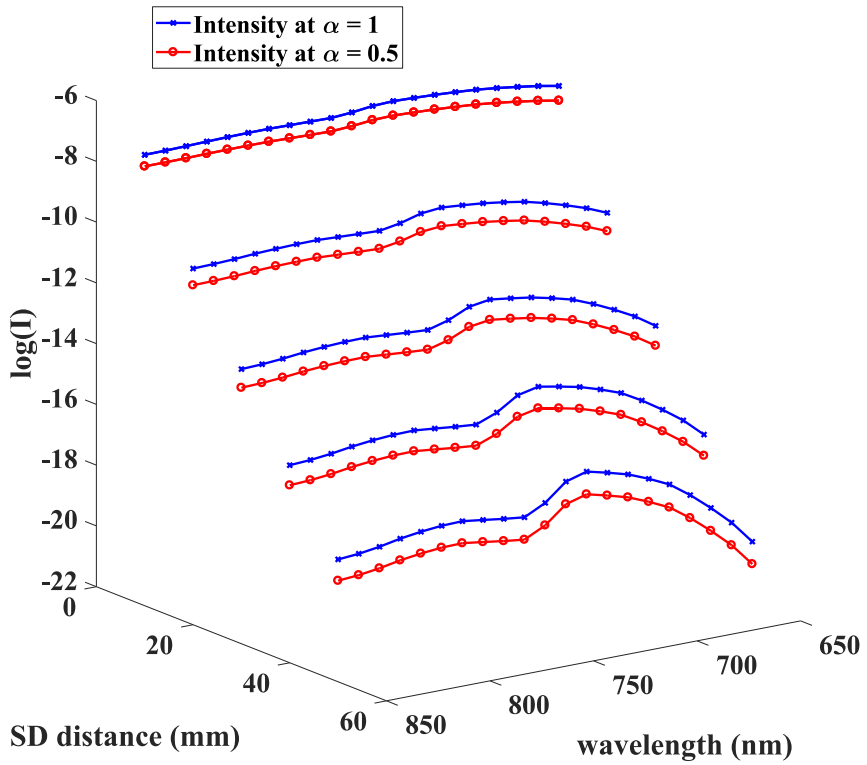

Figure 4.3. Intensity data at α = 1 and 0.5

4.3. Methodology

Initially, the complex structure of the head is simplified into two layers to better understand and distinguish the haemodynamics of cerebral and extra-cerebral (skin and skull) tissues. For a two-layered semi-infinite medium (as shown in Figure 4.1), the measured boundary intensity at a detector at a distance ρ from a point-source can be written as (36, 80):

$$I(\rho) = \frac{1}{2\pi}\int_0^\infty \phi(s)\, s\, J_0(s\rho) ds, \tag{4.9}$$

where, s is the radial spatial frequency coordinate corresponding to the radial distance ρ, J_0 is the zeroth order Bessel function of first kind, and ϕ is given by:

$$\phi(s) = \frac{\sinh\big(\alpha_1(z_b + z_0)\big)}{\kappa_1\alpha_1} \times \frac{\kappa_1\alpha_1\cosh(\alpha_1 L) + \kappa_2\alpha_2\sinh(\alpha_1 L)}{\kappa_1\alpha_1\cosh(\alpha_1(L+z_b)) + \kappa_2\alpha_2\sinh\big(\alpha_1(L+z_b)\big)} - \frac{\sinh(\alpha_1 z_0)}{\kappa_1\alpha_1} \tag{4.10}$$

Here, L is the thickness of layer-1, the subscripts 1 and 2 indicate the properties for layer-1 and layer-2, $\alpha_i = \sqrt{s^2 + \frac{\mu_{a_i}}{\kappa_i}}$, diffusion coefficient $\kappa_i = \frac{1}{3\left(\mu_{a_i} + \mu'_{s_i}\right)}$, $z_0 = \frac{1}{\mu_{a_1} + \mu'_{s_1}}$, $z_b = \frac{1+R_{\text{eff}}}{1-R_{\text{eff}}} 2\kappa_1$ and R_{eff} is the fraction of photons internally and diffusively reflected at the boundary.

As shown in section 4.2, for the measured CW intensity data on the boundary of a two-layered medium a unique solution exists for a parameter set $\{\mu_{a_1}, \mu'_{s_1}, \mu_{a_2}, \mu'_{s_2}, \mathrm{L}\}$. To increase the number of independent measurements and therefore improve the recovery accuracy the problem is spectrally constrained by measuring the intensity data over a broad range of wavelengths. For biological tissues, since haemoglobin is the major absorbing chromophore in the near-infrared range, the wavelength range 650 to 850 nm at either side of the isosbestic region are considered (which is typically conventional in most systems, well away from 950 nm beyond which other molecules, such as Methaemoglobin and water are the dominant absorbing chromophores). Although other chromophores have significant extinction coefficients in this wavelength range, their concentration in the tissue is relatively low, therefore oxy and deoxy haemoglobin can be considered as the main absorbers. The parameter set now becomes $\mathbf{p} \equiv \{HbO_1, HbO_2, Hb_1, Hb_2, Sa_1, Sa_2, Sp_1, Sp_2, L\}$, and measurement data is the light intensity at source-detector distances $\rho = 10, 20, 30, 40, 50$ mm, and wavelengths $\lambda = 650$ to 850 nm, in steps of 10 nm. Instead of a conventional approach of recovering all parameters together using a least-square minimization method which generally exhibits a very high condition number, the recovery of parameters is achieved in two steps: (1) recovering layer-1 parameters from spectral intensity data at $\rho = 10$ mm i.e., a short source-detector distance, assuming a homogenous model as implemented by considering same parameters of layer-1 and layer-2 properties in equation (4.10), the dependency on L is assumed to be minimal in such a case, and (2) utilizing the recovered layer-1 parameters in step-1, the layer-2 parameters and tissue thickness L, are recovered using spectral intensity data from $\rho = 10$ to 50 mm. This splitting of the parameter

recovery is observed to greatly improve the inverse problem with decreasing the condition number by at least an order of magnitude (i.e., by a factor of 10).

Consider the column vectors $\mathbf{p_1} \equiv \{HbO_1, Hb_1, Sa_1, Sp_1\}$, and $\mathbf{p_2} \equiv \{HbO_2, Hb_2, Sa_2, Sp_2, L\}$, denoting the parameter sets for the two step parameter recovery with the corresponding measurement data given by the column vectors $\mathbf{y_1} \equiv I(\rho, \lambda)$ at $\rho = 10$ mm and $\lambda = 650$ to 850 nm in steps of 10 nm, and $\mathbf{y_2} \equiv I(\rho, \lambda)$ at $\rho = 10$ to 50 mm in steps of 10 mm, and $\lambda = 650$ to 850 nm in steps of 10 nm. Let v_m be the *m*-th entry in the column vector $\mathbf{v}$, then the element $\mathrm{j}_{1_{mn}}$ (of *m*-th row and *n*-th column) of the Jacobian (or sensitivity) matrix $\mathbf{J_1}$ corresponding to recovery step-1 is given by,

$$\mathrm{j}_{1_{mn}} = {}^{\partial \mathrm{y}_{1_m}}\!\Big/\!_{\partial \mathrm{p}_{1_n}} \tag{4.11}$$

Similarly, the element $\mathrm{j}_{2_{mn}}$ of the Jacobian matrix $\mathbf{J_2}$ corresponding to step-2 is given by,

$$\mathrm{j}_{2_{mn}} = {}^{\partial \mathrm{y}_{2_m}}\!\Big/\!_{\partial \mathrm{p}_{2_n}} \tag{4.12}$$

The inverse problem at each step is then implemented by an iterative regularized least-square minimization, where the data is modelled corresponding to the estimated parameter set at each iteration (beginning with an assumed initial values). Based on the mismatch between modelled and measured data the following parameter update equation is calculated at the end of each iteration, (43)

$$\Delta \mathbf{p_i} = \left(\mathbf{J_i}^{\mathrm{T}} \mathbf{J_i} + \beta \mathbf{I}\right)^{-1} \mathbf{J_i}^{\mathrm{T}} \Delta \mathbf{y_i} \tag{4.13}$$

Here, 'i' denotes the recovery step-1 or 2, $\Delta \mathbf{p_i}$ represents the update for the parameter set $\mathbf{p_i}$, $\Delta \mathbf{y_i}$ is the data-model misfit at the end of iteration, and $\mathbf{J_i}$ is the corresponding Jacobian matrix. To further aid the stability, the inverse problem is guided with a regularization parameter given by β, which is considered as 0.01 times the maximum value of the Hessian $\mathbf{J_i}^{\mathrm{T}} \mathbf{J_i}$. A relative change of less than 2% in the error corresponding to data-model misfit over two successive iterations is considered as the stopping criteria for the inverse problem.

The simulation study is split into three parts. Part-(1) deals with data generated on a two-layered semi-infinite model and recovered using a two-layered semi-infinite model as well. To consider a more practical scenario, in part-(2) the data is generated on a two-layered head model but parameter recovery is implemented using two-layered semi-infinite model. Part-(3) deals with data generated on head model and recovered using a head model as well. Part-(2) and (3) are compared to see if the semi-infinite model based recovery is close enough to head-model based recovery.

4.4. Results

4.4.1. Two-layered semi-infinite model

The two-layered semi-infinite model as described in equations (4.9) and (4.10), is employed to simulate the measurement data. The modelled measurement system consists of source-detector distances of 10 to 50 mm in steps of 10 mm, Figure 4.4, and wavelengths from 650 to 850 nm in steps of 10 nm, and a Gaussian random noise of 1% is added to the data. From previous studies, a noise level from 0.12 to 1.42% is generally added for source-detector separations varying from 13 to 48mm (75), to represent a physical model. In this work, apart from multi-distance measurements varying from 10 to 50 mm, we have broadband wavelength data ranging from 650 to 850 nm, and therefore the distribution of noise levels is more complex than that. Therefore, an average of 1% random noise is applied for all source-detector separations and wavelengths. The tissue properties of the two layers are as shown in Table 4.1

(75), and 10 different cases of randomly varying scattering properties (i.e., both Sa and Sp) of both layers are considered with a standard deviation of 10% around the reference values, to include the inter-subject variability in scattering properties. To understand the response of the recovery method to different cerebral oxygenation levels, the TOI of layer-2 was also varied from 50% to 80% which are considered the practical extreme values (78, 79). The sensitivity matrices corresponding to step-1 and step-2 of the recovery process as given in equations (4.11) and (4.12), are calculated using perturbation method on the analytic expression of equations (4.9) and (4.10). The whole simulation study is repeated for different layer-1 thickness values of L=8,

10, 12 mm which are in the range of practical values for the extra-cerebral thickness of human head.

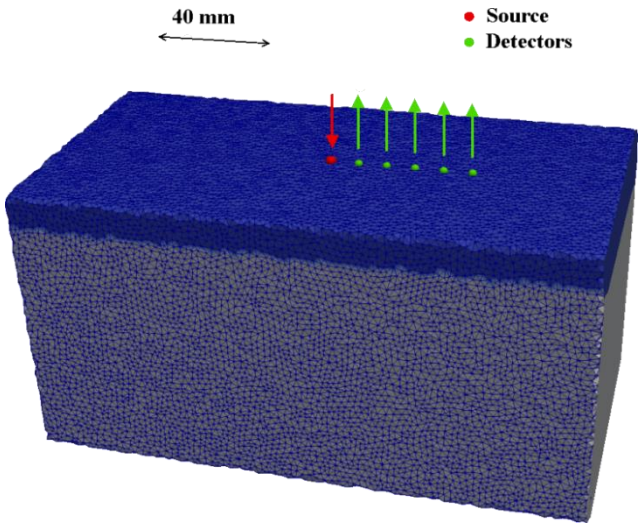

Figure 4.4. Schematic showing semi-infinite model with source-detector locations on the boundary

Table 4.1. Tissue parameters

	HbT (mM)	TOI (%)	Sa (mm^{-1})	Sp
Layer-1	0.059	80	0.64 ± 10%	1.0685 ± 10%
Layer-2	0.076	50-80	0.98 ± 10%	0.611 ± 10%

The recovered TOI values of the two-layers for different thicknesses of layer-1 (8, 10, 12 mm) are as shown in Figure 4.5 in comparison to the homogenous parameter recovery. The homogenous parameter recovery is similar to step-1 in the proposed two-layered recovery process, but all the measured source-detector distances are considered. The retrieved values of layer-1 thickness is as shown in Figure 4.6.

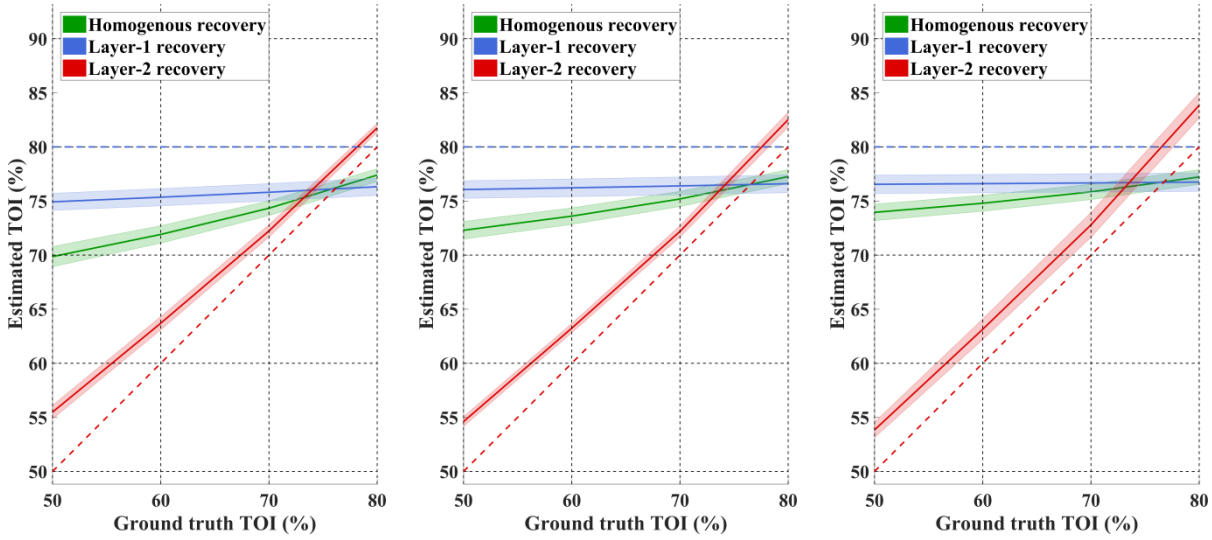

Figure 4.5. Estimated TOI values from the homogenous and two-layered parameter recovery methods corresponding to a two-layered semi-infinite medium of Layer-1 thickness as (a) 8 mm, (b) 10 mm, and (c) 12 mm, using multi-distance broadband CW data. The ground-truth values of layer-1 and layer-2 is shown by dashed lines. The shaded region shows the standard deviation of recovery for different scattering parameters.

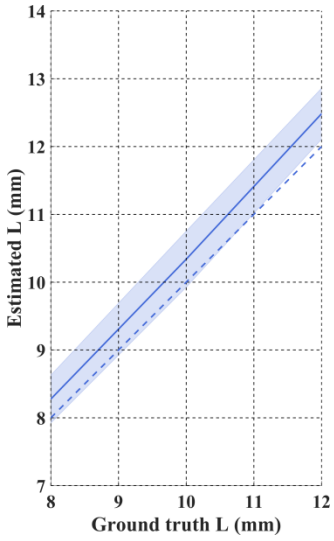

Figure 4.6. Estimated Layer-1 thickness from the two-layered parameter recovery method using multi-distance broadband CW data. The shaded region shows the standard deviation of recovery for different scattering parameters of both layers and different TOI values of layer-2.

Table 4.2. Average percentage error (%) in homogenous and two-layered parameter recovery for different ground-truth scattering parameters and different TOI values of layer-2

Layer-1 thickness →		8 mm	10 mm	12 mm
%Δ HbO	Homogenous	-31.5 ± 17.3	-23.8 ± 18.4	-17.8 ± 19.1
	Layer-1	10.0 ± 4.5	8.2 ± 2.6	7.1 ± 1.4
	Layer-2	-16.6 ± 7.2	-15.0 ± 6.1	-15.9 ± 4.9
%Δ Hb	Homogenous	6.1 ± 23.2	16.3 ± 23.3	23.6 ± 22.7
	Layer-1	-15.9 ± 2.6	-13.8 ± 1.9	-13.0 ± 1.2
	Layer-2	-0.3 ± 9.7	0.8 ± 5.2	2.4 ± 3.4
Δ TOI	Homogenous	8.3 ± 8.3	9.5 ± 9.3	10.4 ± 9.9
	Layer-1	-4.4 ± 0.5	-3.6 ± 0.2	-3.3 ± 0.1
	Layer-2	3.2 ± 1.4	3.1 ± 0.9	3.4 ± 0.5
%Δ Sa	Homogenous	39.4 ± 0.6	38.8 ± 0.3	37.8 ± 0.2
	Layer-1	-8.2 ± 2.9	-8.2 ± 1.8	-8.1 ± 0.9
	Layer-2	7.9 ± 4.8	7.6 ± 1.6	6.4 ± 1.1
%Δ Sp	Homogenous	-13.7 ± 0.3	-15.7 ± 0.4	-17.5 ± 0.5
	Layer-1	25.8 ± 0.4	26.1 ± 0.2	26.3 ± 0.1
	Layer-2	-44.9 ± 9.8	-48.8 ± 9.9	-52.4 ± 8.7
%Δ L	Layer-1	3.4 ± 4.4	3.4 ± 4.1	4.0 ± 3.1

The above results in Table 4.2 show that the proposed two-layered broadband parameter recovery method retrieves the tissue oxygenation index and tissue thickness within 4.4% and 4% error respectively. Recovery of other tissue parameters (haemoglobin concentrations and scattering amplitude of two layers) can be obtained within 16.6% error with this two-layered approach, as compared to 31.5% error with the homogenous parameter recovery. However, the scattering power parameter exhibits relatively higher recovery errors due its low sensitivity to light-intensity.

4.4.2. Two-layered head model

In a realistic scenario, the structure of the head is more complex than a two-layered semi-infinite geometry. Therefore, data was simulated using the same tissue properties as shown in Table 4.1 on two-layered (cerebral and extra-cerebral tissues) head models using NIRFAST corresponding 10 different subject head models, Figure 4.7, with their scattering parameters (both Sa and Sp) randomly varying with 10% standard deviation from the reference values shown in Table 4.1 and the cerebral TOI varying from 50% to 80%, and subsequently the two-step parameter recovery algorithm was utilized, initially, using a two-layered semi-infinite model for the recovery. This was to consider the case where data is from a human subject, but the model utilized for parameter recovery is based on a simple two-layered model. The parameter recovery results are shown in Figure 4.8 (a), Figure 4.9, and Table 4.3 . As some measurement data does not converge to a stable solution, from these results it can be observed that the parameter recovery is accompanied by high standard deviation which can be attributed to the mismatch between the assumed semi-infinite model and the true head-model.

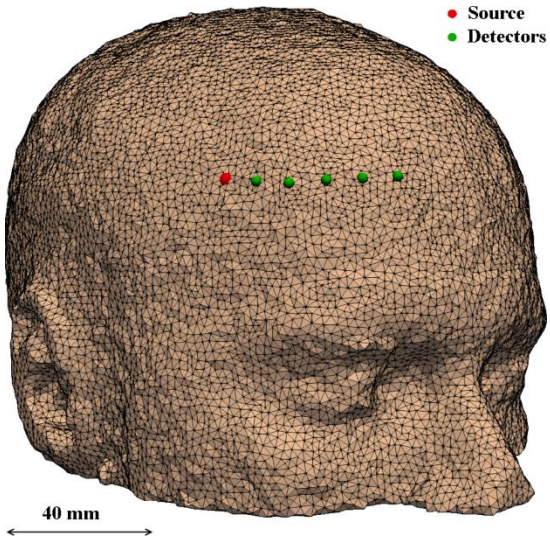

Figure 4.7. Schematic showing an example of the head model with source-detectors placed on the forehead.

To overcome this instability for parameter recovery using a semi-infinite or slab-model approximation, a second head-model that is different to that as used for the data simulation is introduced and incorporated in the inverse problem to improve the accuracy and consistency of the parameter recovery. The geometrical information for the external boundary of this head model (obtained from the original subject specific head model) is used for the inverse problem, therefore instead of the semi-infinite model, a medium with similar boundary as the true head model is considered and by building a model corresponding to this geometry, NIRFAST was used to generate the model-data for the inverse problem, and also for calculating the sensitivities of layer-1 and 2. A dense mesh is built for the recovery model (with an average element size around 0.1 mm^3 which 10 times smaller than the average element size of 1.7 mm^3 considered for head models that are used to simulate data) to compute the sensitivity values corresponding to tissue

thickness as shown in equation (4.12). Individual layers are assigned to this model structure based on the distance from the boundary surface, therefore unlike the original head model which has a heterogeneous and spatially varying thickness of layer-1, the recovery model consists of uniform layer-1 thickness. So, although this model is better than the semi-infinite model by considering the external boundary structure, its internal structure is not exactly the same as the true head model. The corresponding parameter recovery is shown in Figure 4.8 (b), Figure 4.10, and Table 4.3.

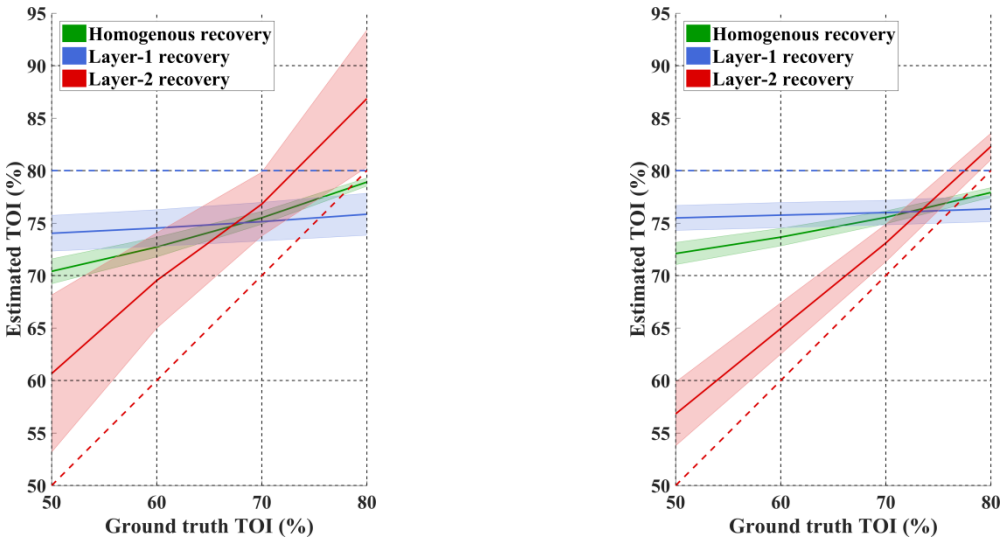

(a) (b)

Figure 4.8. Homogenous and two-layered recovery of TOI for two-layered head model based on: (a) semi-infinite recovery model, (b) head based recovery model. The shaded region shows the standard deviation over different head models with different scattering parameters.

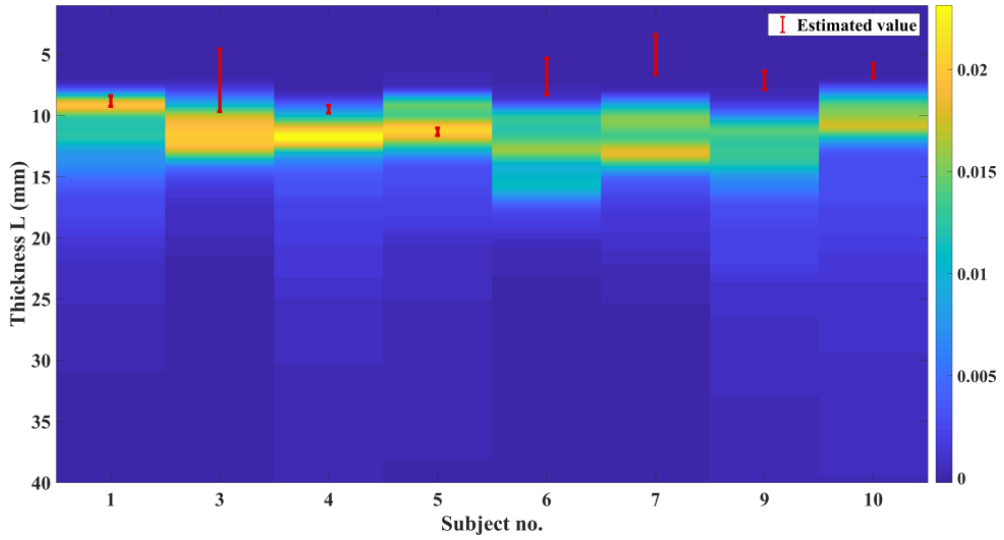

Figure 4.9. Estimated values of layer-1 thickness with semi-infinite recovery model corresponding to extra-cerebral tissue for 10 subject head models, along with the ground-truth probability density function of extra-cerebral tissue thickness in the region of interest. Subjects 2, 8 are not shown as the algorithm did not converge to a stable solution.

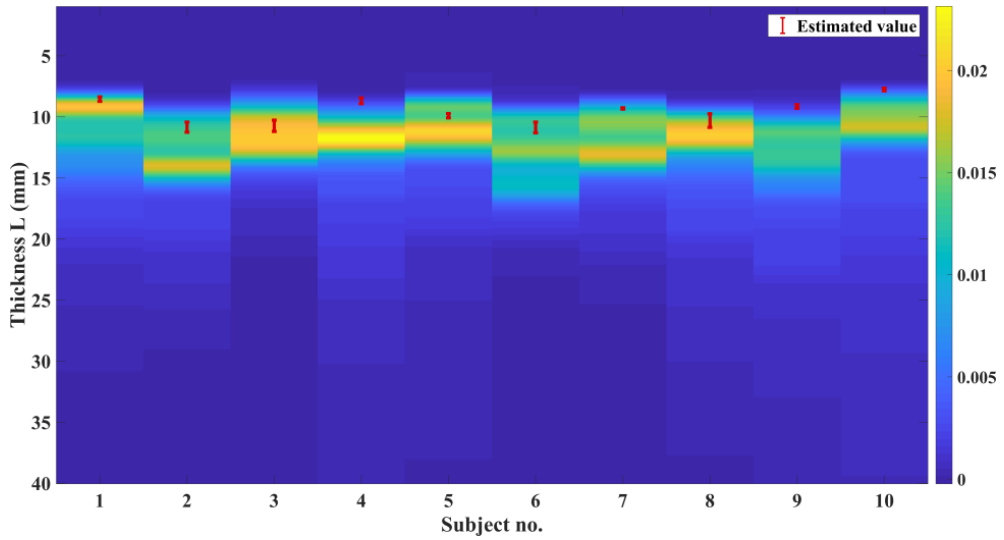

Figure 4.10. Estimated values of extra-cerebral tissue thickness with head-based recovery model for 10 subject head models, along with the ground-truth probability density function of extra-cerebral tissue thickness in the region of interest.

Table 4.3. Average percentage error (%) in the homogenous and two-layered recovery of parameters corresponding to a semi-infinite recovery model and a head based recovery model

Recovery model →		Semi-infinite recovery model	Head-based recovery model
%Δ HbO	Homogenous	22.0 ± 13..3	-27.2 ± 18.4
	Layer-1	21.9 ± 2.9	5.2 ± 4.4
	Layer-2	19.0 ± 7.5	-23.3 ± 7.6
%Δ Hb	Homogenous	48.3 ± 9.3	15.3 ± 22.5
	Layer-1	-5.5 ± 1.2	-20.0 ± 3.7
	Layer-2	45.4 ± 6.1	-1.36 ± 7.6
Δ TOI	Homogenous	9.3 ± 8.0	9.8 ± 9.0
	Layer-1	-5.1 ± 0.6	-4.1 ± 0.3
	Layer-2	8.4 ± 2.6	4.2 ± 1.9
%Δ Sa	Homogenous	12.3 ± 2.2	37.8 ± 0.4
	Layer-1	-34.0 ± 2.2	-6.2 ± 2.7
	Layer-2	4.4 ± 14.4	16.2 ± 2.7
%Δ Sp	Homogenous	-41.2 ± 4.0	-22.1 ± 0.4
	Layer-1	17.8 ± 0.8	26.8 ± 1.1
	Layer-2	-87.8 ± 58.3	-44.2 ± 7.6

These results demonstrate that for the data corresponding to a head model, the proposed algorithm with a semi-infinite recovery-model estimates the TOI with an average recovery error of 8.4% with the two-layered recovery approach as compared to the error of 9.3% with the homogenous approach. Recovery of other tissue parameters (except for scattering power) can be achieved within 45.4% error with the two-layered approach as compared to the error of 48.3% with the homogenous recovery approach. However, using an appropriate recovery model (head based model) the parameter recovery can be greatly improved by reducing the average recovery error of TOI to 4.2% with the two-layered approach as compared to the error of 9.8% with the homogenous approach, and the recovery of other tissue parameters (except for scattering power) can be achieved within 23.3% error with the two-layered approach as compared to the error of 37.8% with the homogenous recovery approach. However, the scattering power parameter exhibits relatively higher recovery errors due its low sensitivity to light-intensity. In regard of the extra-cerebral tissue thickness, as the ground-truth is not a single value but rather varies spatially, we can quantify this variation in terms of a probability density functions as shown in Figure 4.9 and Figure 4.10, and by considering the tissue thickness at the peak probability as the ground-truth, the semi-infinite recovery model estimates the tissue thickness with an average error of 30.1%, whereas using an appropriate head based recovery model the error in estimating the tissue thickness is reduced to 11.8%.

4.4.3. NIRS on forehead: experimental results

A broadband white-light tungsten-halogen light source is used along with a spectrometer to demonstrate the applicability of the described method using real NIRS data measured on a healthy subject at rest. A single subject was recruited from the University of Birmingham community, and written informed consent was obtained. A Tungsten-Halogen light source (Ocean optics HL-2000-FHSA, with approximately 5 minutes of stabilization time) is connected to an optical fiber and used as the source placed on forehead of the subject. Another fiber as connected to a spectrometer (Ocean optics Flame-S) is used as the detector placed on forehead of the subject at a distance 10, 20, 30, 40 mm away from the source. The 50 mm measurement was not used due to its low SNR. The two fibers (Ocean Optics: QP1000-2-VIS-BX) utilized in this experiment have a 1000 µm core diameter, with the efficient wavelength range from 300-1100 nm. The spectrometer consists of an entrance slit of 200 µm, and a grating with groove density of 600 grooves per mm. The signal is collected over different acquisition times of 30 ms, 1.5 s, 15 s, and 30 s, for the source-detector distances of 10, 20, 30 and 40 mm respectively, to obtain a good SNR with the average noise across the wavelengths 650 to 850 nm being less than 5% for these acquisition times. While a 30 s acquisition time for a 40mm measurement is just sufficient to get the signal under noise threshold, the shorter distance measurements are well under 5% noise. The collected signal is time averaged by normalizing each measurement by its corresponding acquisition time. The spectrometer measures the intensities from 340 nm to 1015 nm at a spectral resolution of 0.3 nm, which is later down-sampled to a resolution of 10 nm by averaging every 33 (10/0.3) spectral data points, and is then cropped to the wavelength range 650 nm to 850 nm to match with measurement model considered in simulations. The intensity

measurements at different source-detector distances were measured sequentially (starting from 10 mm to 40 mm) due to instrumental limitations. The subject is at rest during the measurements for all experiments. Each experiment was performed once a day with no stimuli and the subject position and data acquisition protocol was kept constant for all measurements, and therefore it was assumed that the haemodynamic changes over the entire duration of measurements (approx. 3 to 5 mins) were insignificant as often seen during the base-line measurements (81) while the subject is at rest. The proposed head based recovery method as described in section 4.4.2 was implemented using the boundary information of the forehead obtained from the MRI of the subject, and later the layer-1 thickness and tissue parameters of two layers were obtained. It should be noted that, while the MRI of the subject was obtained in supine position, and the subject was measured while sitting on a chair at rest during the experiment and the position was kept constant for all measurements. As the anatomical boundary information of the subject comes from the thin skin/scalp tissue situated on the rigid structure of skull which is unaffected by the subject posture, the boundary information remains the same between the measurements and the acquired MRI. The NIRS experiment is repeated on three different days and the recovery of the parameters are as shown in Table 4.4. Although the physiological parameters of the tissue may have changed over different days, consistent values of tissue thickness over three days were recovered to ascertain the repeatability of the proposed method.

Table 4.4. Homogenous and two-layered parameters recovered using the head-based recovery method described in section 4.4.2

		Day-1	Day-2	Day-3
		Head-based recovery model	Head-based recovery model	Head-based recovery model
HbO (mM)	Homogenous	0.0697	0.0520	0.0694
	Layer-1	0.0358	0.0439	0.0563
	Layer-2	0.1116	0.1333	0.1567
Hb (mM)	Homogenous	0.0201	0.0145	0.0199
	Layer-1	0.0075	0.0098	0.0138
	Layer-2	0.0699	0.1017	0.1130
TOI (%)	Homogenous	77.6	78.2	77.7
	Layer-1	82.6	81.7	80.3
	Layer-2	61.4	56.7	58.1
Sa (mm-1)	Homogenous	0.44	0.56	0.44
	Layer-1	0.58	0.51	0.43
	Layer-2	0.34	0.24	0.12
Sp	Homogenous	0.64	0.69	0.65
	Layer-1	0.69	0.68	0.65
	Layer-2	1.07	1.26	3.0
L (mm)	Layer-1	9.9	10.7	10.8

4.5. Discussion

A broadband continuous wave NIRS parameter recovery method is presented to distinguish extra-cerebral and cerebral tissue haemodynamics, by separating the tissue absorption and scattering parameters and also by simultaneously fitting for the superficial layer thickness. Major challenges of continuous wave NIRS system have been the recovery of scatter (i.e., separating absorption and scattering information from the measured NIRS signal), and removing/separating the extra-cerebral tissue contamination from the NIRS signal to estimate the cerebral haemodynamics. It is shown theoretically in section 4.2 that, while for a given spectral derivative of intensity measurements (any derivative measurements) have non-unique solution sets of layered tissue parameters, the absolute intensity measurements have a unique solution set of layered tissue parameters. A two-step approach is presented to recover the two-layered properties along with tissue thickness. In the case of data generated on a two-layered semi-infinite model, the proposed two step approach using a semi-infinite model in the inverse problem is shown to recover the tissue parameters within 16.6% errors. The recovery error of layer-1 properties are reduced with increasing thickness, this is because of the assumption in step-1 that the short distance measurement is only influenced by layer-1. This increase in accuracy of the estimation of layer-1 properties in step-1 which increase with thickness, should improve the recovery of layer-2 properties in step-2 but with increased thickness there is a drop in the sensitivity of layer-2 and therefore a similar trend of improvement in accuracy is not seen for layer-2. The opposite sign of mean-relative errors for absorption (i.e., HbO and Hb) and scattering parameters (scattering amplitude) shows that the cross-talk between these

parameters is negatively related, any over-estimation of absorption is accompanied by an under-estimation of scattering amplitude and vice versa.

In the case of data generated on head models, a semi-infinite recovery model is shown to recover results with mixed accuracy. This is due to the complex structure i.e., the spatially varying curvature of external medium boundary and internal regional boundary. This is evident from the recovery accuracy of tissue thickness in Figure 4.9 for some head models where a correct two-layered semi-infinite model approximation wasn't found. Therefore, to tackle this problem, using an appropriate boundary structure with the similar two-step parameter recovery approach, it has been demonstrated that the accuracy is greatly improved and similar to the initial case where the data is generated and recovered on semi-infinite model.

The practical implementation of this method has been shown in section 4.4.3. The results presented in Table 4.4 show that the variation in tissue oxygenation levels recovered over three different days is less than 5%, and the variation in the recovery of extra-cerebral tissue thickness was not more than ~1mm, which clearly demonstrates the repeatability of the recovery algorithm. The increase in hemoglobin concentrations across days observed in Table 4.4 accompanied by a decrease in the scattering amplitude can be accounted for the cross-talk between these two parameters, which is also in line with the simulation results observed in Table 4.3 with recovery errors of hemoglobin concentration and scattering amplitude with opposite signs.

It is important to highlight that the human head consists of multiple layers, such as skin, skull, CSF and brain tissue. Therefore, although the proposed methodology only assumes a two-layer model, to account for superficial signal contamination, the results indicate that this is much

more suitable and robust as compared to the conventional homogenous assumptions. Future work should be directed towards extending this methodology to account for multiple layers, which may require the utilization of more boundary measurements and data-types to better extract information about pathlength (45).

4.6. Conclusions

A two-layered parameter recovery method using multi-distance broadband CW intensity measurements is proposed and demonstrated to recover the absolute hemoglobin concentrations, scattering parameters along with the superficial tissue thickness of a human head through simulations across different head models corresponding to different subjects. A practical implementation of this approach with real human subject data measured on forehead is presented and has shown good repeatability in the recovered tissue parameters over three days. However, validation of these results is challenging as the absolute tissue parameters are unknown, it is the subject of future studies and needs further investigation. Finally, this work suggests the ability of multi-distance CW broadband data to retrieve or separate the extra-cerebral tissue parameters and the cerebral tissue parameters and that such an approach is more accurate than recovering bulk tissue parameters.

While the heterogeneity or the superficial tissue contamination brought by the extra-cerebral tissue is dealt with in terms of absolute parameter recovery in this chapter by separating the recovery of the cerebral and extra-cerebral tissues, this aspect of superficial contamination in dynamic parameter recovery (as outlined in section 2.3.2) is well known as briefly outlined in section 2.5.2.2. a similar procedure to reduce the contamination from superficial tissue is yet to

be defined for other data-types (such as phase data in frequency-domain). This leads to the work presented in the next chapter.

Chapter 5

SIGNAL REGRESSION IN FREQUENCY DOMAIN DIFFUSE OPTICAL TOMOGRAPHY TO REDUCE SUPERFICIAL SIGNAL CONTAMINATION

5.1. Introduction

The aim of this chapter is to address the superficial layer contamination in the context of fNIRS based optical imaging systems for data-types other than intensity measurements, such as phase in frequency domain systems. Functional near-infrared spectroscopy (fNIRS) based optical imaging is a neuroimaging technique used to non-invasively monitor functional activity in the brain by tomographic reconstruction of the haemodynamic activity and is often termed as diffuse optical tomography (DOT). These reconstructions can be used in clinical applications such as patient monitoring (82), psychology studies (83, 84) and functional brain mapping (85). It is a relatively inexpensive technology and nonionizing in nature as compared to the alternative neuroimaging tools such as magnetic resonance imaging, computed tomography or positron emission tomography. FD-DOT relies on the measurements of the light intensity and phase, using multi-distance overlapping source-detectors placed on the scalp. The spectrally varying optical properties of the medium that contribute to variation in the measured data-types, are then reconstructed using a diffusion theory based inverse model as described in Chapter 2. While, the contamination of NIR signal with haemodynamic changes in superficial region (82, 86) is a major

challenge as discussed in earlier chapters, a high density overlapping measurements of the multi-source-detector setup, together with the varying depth sensitivity based on source-detector distances directly allow the reconstruction of haemodynamic changes by spatially separating the contributions from deep and shallow regions (75). However, it is still a common practice to apply superficial signal regression on the DOT measurement signals prior to the reconstruction step to significantly improve the 3D recovery including the improvement of recovered contrast of focal activations (70).

At a relatively higher instrumentation cost as compared to CW systems, with the use of a modulated NIR light typically at 100-200 MHz, Frequency domain (FD) systems enable the measurement of the phase shift of the detected NIR light after traversing through the tissue, and these phase measurements correspond to the average pathlength of the photon travelled. Recent works in FD-DOT (71) have demonstrated the more uniform sensitivity of the phase measurements towards deeper tissue, and therefore resulting in a more accurate recovery of focal activations in the brain with a reduction of 59% in localisation error and 21% effective resolution as compared to CW-DOT. To further demonstrate the benefit of utilising phase measurements from a FD system, the sensitivities (Jacobian) of intensity (log intensity) and phase measurements at a single wavelength are shown in Figure 5.1, for a five-layered slab model representing the skin, skull, CSF, grey matter and white matter regions of the head. The thickness of skin, skull, CSF, grey matter is considered to be 2.5mm, 6.5mm, 3mm, and 25mm respectively with the tissue properties as shown in Table 5.1 and the sensitivity maps are shown for source-detector distances of 10, 20, 30 and 40mm. The increasing depth sensitivity of intensity and phase with increasing source-detector distance is clearly observed, and for the same source-

detector distance the phase measurement demonstrates a higher depth sensitivity, while more uniform as compared to intensity.

While this is a very promising aspect of the FD-DOT technique, a straight-forward superficial signal regression procedure on both intensity and phase signals, as will be shown, can result in misleading haemodynamic recovery. It is demonstrated in this work that as the phase signals have relatively higher sensitivity towards deeper tissue than intensity signals, even the short distance phase measurements (which may unknowingly be used to regress superficial signal contamination) may be used to measure the functional activity from the deeper tissue.

The primary requirement of the regressor signal (the short distance measurement that is regressed from the measurements) is that it should be uncorrelated (i.e., orthogonal) to the signals originating at the deeper tissue. The orthogonality will ensure that the correct amount of the regressor signal is removed from the measurements without any residual amount of regressor signal present in the measurements as indicated in the next section in equation (5.4). But in the case of phase signals, even the short distance measurement contains some deeper tissue information, making it correlated to the functional signal originating in deeper tissue. Therefore, an un-checked regression of the phase signals using the short-distance phase measurement would not only include the superficial signal contamination in the recovery, but can also result in a reduced component of the functional signal from the brain and may also lead to false positives of functional activations in the cerebral region. In this work, this phenomenon is demonstrated and an alternative regression methodology is provided for reducing superficial signal contamination in the phase signal in the context of FD DOT system.

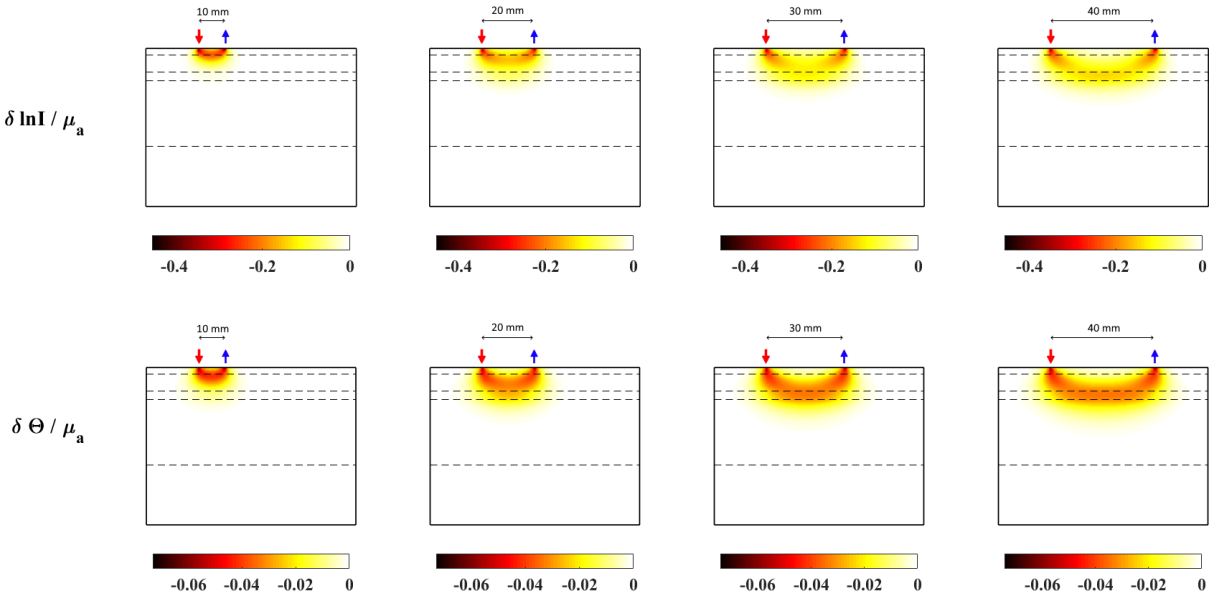

Figure 5.1. Jacobian of log intensity and phase measurements for absorption coefficient at 830 nm, at source-detector distances of 10, 20, 30 and 40 mm, on a five-layered slab. The layers (dashed lines) from top to bottom represent skin/scalp, skull, CSF, grey matter, white matter, with tissue properties shown in Table 5.1.

5.2. Methodology

Consider a NIRS setup with M measurement channels of different source-detector combinations represented by the index i at time t, to measure change in intensity in log-scale $\Delta y_i(t)$, i.e., the change in attenuation of intensity at a given wavelength. It can be expressed as a sum of changes in attenuation due to absorption changes in superficial tissue and in the brain tissue (assuming there are no scattering related changes), which can be written as:

$$\Delta y_i(t) = s_{ys}(i)\,\Delta\mu_{a_s}(t) + s_{yb}(i)\,\Delta\mu_{a_b}(t) \tag{5.1}$$

Here, $s_{ys}(i)$ and $s_{yb}(i)$ are the sensitivities of intensity with respect to absorption changes in superficial and brain tissues respectively, corresponding to a source-detector channel-i. Similarly, the differential phase signal $\Delta p_i(t)$, has a contribution from absorption changes in superficial tissue as well as the brain tissue as:

$$\Delta p_i(t) = s_{ps}(i)\,\Delta\mu_{a_s}(t) + s_{pb}(i)\,\Delta\mu_{a_b}(t) \tag{5.2}$$

where, $s_{ps}(i)$ and $s_{pb}(i)$ are the sensitivities of phase with respect to absorption changes in superficial and brain tissues respectively, corresponding to channel-i. As seen in the above two equations, the NIRS signal is inherently contaminated with changes corresponding to the superficial tissue. In this regard, signal regression techniques are generally used to remove the haemodynamic changes in the superficial tissue, which can otherwise lead to artefacts or over-shadow the functional activation in recovery due to very high sensitivity of superficial tissue relative to the brain. The primary requirement to completely remove superficial signals using a regression method is that the changes in superficial tissue and the brain tissue must be orthogonal to each other (87). By definition, two signals $x_1(t)$ and $x_2(t)$ are said to be orthogonal if they are uncorrelated i.e., their inner product $\langle x_1, x_2\rangle = 0$. The inner-product is defined as:

$$\langle x_1, x_2\rangle = \int_{-\infty}^{\infty} x_1(t)\,x_2(t)\,dt \tag{5.3}$$

Considering $\Delta y_{nn}(t)$ to be the nearest-neighbor (short distance) intensity signal and by assuming it is strongly sensitive to the absorption changes in superficial tissue i.e., $\Delta y_{nn}(t) = k\Delta\mu_{a_s}(t)$ (where k is the corresponding sensitivity factor), along with the condition that the absorption changes in superficial tissue are orthogonal to absorption changes in brain tissue, i.e., $\langle \Delta\mu_{a_s}, \Delta\mu_{a_b} \rangle = 0$, the contribution from the superficial tissue can be regressed from the intensity signals using:

$$\Delta y_{r_i}(t) = s_{yb}(i)\, \Delta\mu_{a_b}(t) = \Delta y_i(t) - \frac{\langle \Delta y_i,\ \Delta y_{nn} \rangle}{\langle \Delta y_{nn}, \Delta y_{nn} \rangle} \Delta y_{nn} \tag{5.4}$$

For frequency-domain NIRS systems, a similar regression method (phase based phase regression) can be applied by extending it to the phase signal as follows:

$$\Delta p_{r_i}(t) = s_{pb}(i)\, \Delta\mu_{a_b}(t) = \Delta p_i(t) - \frac{\langle \Delta p_i,\ \Delta p_{nn} \rangle}{\langle \Delta p_{nn}, \Delta p_{nn} \rangle} \Delta p_{nn} \tag{5.5}$$

However, in the context of phase signals, this may not be directly applicable, as even the short distance phase signals will have some contribution coming from the deeper tissues as shown in Figure 5.1. This is due to the fact that the sensitivity of phase signals is higher for deeper tissues as compared to intensity signals. Therefore, implementing the regression as shown above in equation (5.5), would lead to a decrease in the signal contrast from the brain and also contaminate the brain signal with superficial tissue related changes. To avoid this, the use of

short-distance intensity for the phase regression procedure (intensity based phase regression), is proposed as below:

$$\Delta p_{r_i}(t) = s_{pb}(i)\,\Delta\mu_{a_b}(t) = \Delta p_i(t) - \frac{\langle \Delta p_i,\ \Delta y_{nn}\rangle}{\langle \Delta y_{nn}, \Delta y_{nn}\rangle}\Delta y_{nn} \tag{5.6}$$

The effect of these two different signal regression methods will be demonstrated in the following section through the simulation of visual cortical activation as observed using a frequency domain HD-DOT measurement system. It will be clearly shown that a phase based phase regression would retain the superficial signal contamination even after regression which will also result in unwanted and potentially misinterpreted false positives of focal activations. The use of intensity based phase regression is shown to be a much more accurate approach to fully remove the superficial signal contamination from the DOT reconstruction of focal activations using FD data.

5.3. Simulation

A realistic simulation of a functional activation in the visual cortex region is demonstrated in this section to show the effects of the above-mentioned regression methods in the recovery of functional haemodynamic activity from the cerebral region. Consider a five-layer (skin, skull, CSF, grey matter and white matter) head model mesh with 265K nodes and 1.5mm^3 average volume of the tetrahedral elements, and the tissue properties of oxy-haemoglobin (HbO) and deoxy-

haemoglobin (Hb) concentration, scattering amplitude (Sa) and scattering power (Sp) as shown in Table 5.1 (85). The modelled measurement system consists of 24 sources and 28 detectors in an array as shown in Figure 5.2, which is placed on the back of the head to map visual-cortex activations. In such a grid pattern setup, source-detector distances can be categorized into different neighbourhoods i.e., 13mm (nearest neighbour 1 or NN1), 29mm (NN2), 39mm (NN3), 47mm (NN4), 54mm (NN5) and so on. The first four nearest neighbourhoods are considered in this case as limited by the dynamic range of the detectors and the signal-to-noise ratio at higher measurement distances as seen in a realistic scenario (71).

Table 5.1. Background tissue properties

Region	HbO (mM)	Hb (mM)	Sa (mm^{-1})	Sp
Skin	0.0575	0.0313	0.53	1.15
Skull	0.0443	0.0195	0.72	0.89
CSF	0.0110	0.0083	0.30	0
Grey matter	0.0559	0.0350	0.50	1.73
White matter	0.0680	0.0265	0.81	1.31

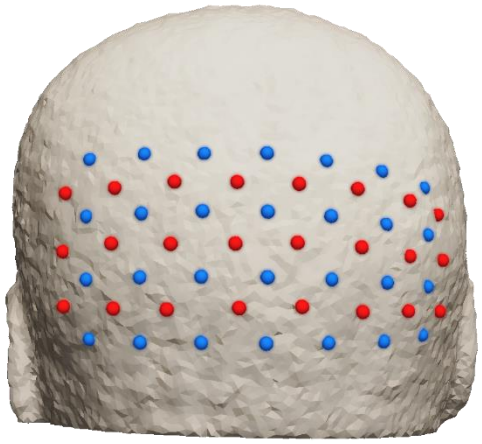

Figure 5.2. Array of 24 sources (red) and 28 detectors (blue) placed on the back of the head to probe visual cortex region.

Physiological signals ($P_j(t)$) at 1.2 Hz, 0.25 Hz, and 0.1 Hz to model cardiac (88), respiratory (89) and Meyer waves (90), are added as sinusoidal changes (91) in haemoglobin concentrations in skin, skull, grey matter and white matter , along with a functional signal $F(t)$ peaking at t=10 seconds originating within grey matter at a depth of 10 mm with an activation

blob of radius 2.5 mm, Figure 5.3. A superficial signal $S(t)$ originating in skin region, peaking at t=30 seconds is also included to observe the effects of superficial layer signal contamination. These functional and superficial signals $F(t)$ and $S(t)$ are modelled using a Gaussian distribution (92) with their temporal full width half maximum (FWHM) values such that the two Gaussian distributions are mutually separated in time to approximately represent two simple orthogonal signals for an ideal regression:

$$F(t) = F_0 \exp\left(-\left(\frac{t-10}{2}\right)^2\right) \tag{5.7}$$

$$S(t) = S_0 \exp\left(-\left(\frac{t-30}{2}\right)^2\right) \tag{5.8}$$

$$P_j(t) = P_{C_j} Q(\omega_C, \mathrm{BW}_C, t) + P_{R_j} Q(\omega_R, \mathrm{BW}_R, t) + P_{M_j} Q(\omega_M, \mathrm{BW}_M, t) \tag{5.9}$$

$$Q(\omega_x, BW, t) = \sum_{\omega} A(\omega) \sin(\omega t + \xi) \tag{5.10}$$

Here, $P_j(t)$ represents the combined physiological signals, while the subscript j=1 represents skin and skull regions and j=2 represents grey and white matter regions. The individual physiological signal $Q(\omega_x, BW, t)$ is a sinusoidal signal with a non-zero bandwidth 'BW' equal to $0.1\times\omega_x$, which can be represented by a sum of sinusoidal signals given by equation (5.10), with their amplitude profile being Gaussian centred at ω_x, and a full width half-maxima of the given BW, along with a random phase offset ξ, such that the function Q lies between -1

and 1, so that P_{C_j}, P_{R_j}, P_{M_j} indicate the respective amplitudes of cardiac, respiratory and Meyer waves from equation (5.9). The physiological signal $P(t)$ is shown in Figure 5.4, along with its frequency spectrum showing a 10% bandwidth associated with these signals.

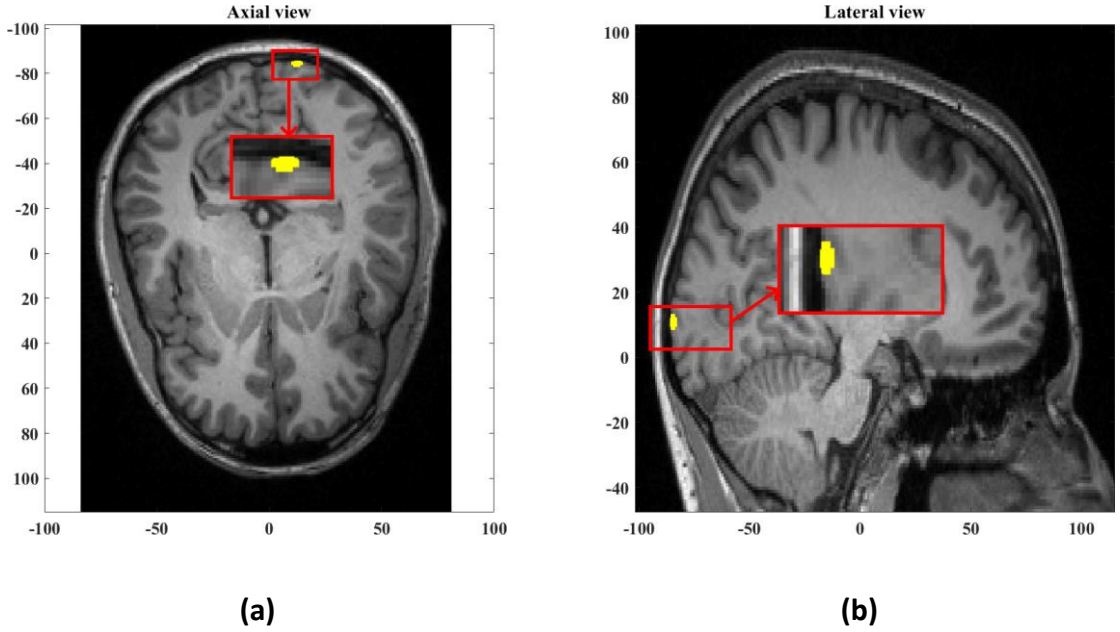

Figure 5.3. (a) Axial view and (b) lateral view of the focal activation in the grey matter at a depth of 10mm and blob radius of 2.5 mm, at time t=10 seconds.

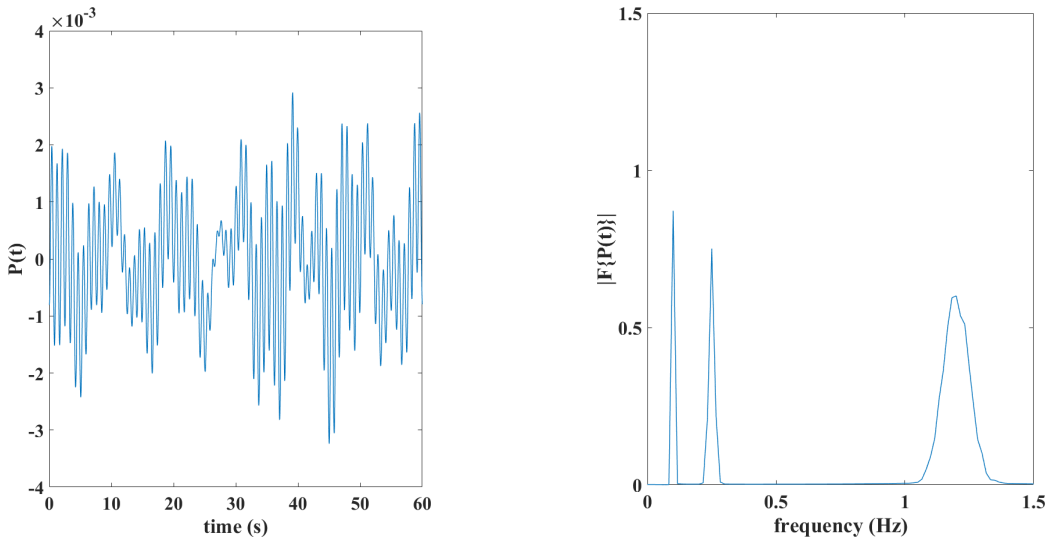

Figure 5.4. (a) Time trace, and (b) frequency spectrum of physiological signal: a combination of cardiac, respiratory and Meyer waves with 10% bandwidth.

All these signals from equations (5.7) to (5.9) represent percentage changes to the background oxy-haemoglobin concentration as given in Table 5.1 with the corresponding deoxy-haemoglobin change considered to be of the same magnitude and opposite sign. For the focal activation however, it is known that the oxy- haemoglobin and the total haemoglobin concentrations increase while the deoxy-haemoglobin decreases (93). In line with this, the deoxy-haemoglobin change for focal activation is considered as '-0.47' times the change observed in oxy-haemoglobin (71). The amplitude F_0 is chosen such that the corresponding maximum observable change in intensity is 0.05 in log scale to accurately represent experimental measurements (69). While the functional signal is only confined to the activation blob of 2.5 mm, the superficial signal occurs in the entire skin region and therefore has quantitatively higher effect on the measured signals. In this regard, S_0 is chosen to be 100 times lower than F_0 so that both functional and superficial

signals can be clearly observed in the both intensity and phase signals. Effectively, the values of these signal strengths considered in this simulation are $P_{C_1} = 0.0018$, $P_{C_2} = 0.006$, $P_{R_1} = 9\times10^{-4}$, $P_{R_2} = 0.0015$, $P_{M_1} = 7\times10^{-4}$, P_{M_2} =0.0012, $F_0 = 3$, $S_0 = 0.03$.

The data is simulated at 40Hz sampling rate, at wavelengths 830 nm and 690 nm at an intensity modulation frequency of 140MHz using NIRFAST (31), with the resulting intensity and phase measurements as shown in Figure 5.5, along with their frequency spectrum. The low-frequency Gaussian profile with ripples at 0.05 Hz (=1/20) interval simply indicates the two Gaussian peaks in the signal at an interval of 20 seconds which correspond to functional and superficial signals in this study. The peaks at 0.1 Hz, 0.25 Hz, and 1.2 Hz correspond to the physiological signals. In accordance with equations (5.7) and (5.8), the negative peak at t=10s in the data as shown in Figure 5.5(a) and Figure 5.5(b) correspond to the increase in oxy-haemoglobin and decrease in deoxy-haemoglobin concentrations at t=10s. This is the functional signal from the modelled focal activation and it becomes stronger (particularly for Intensity data) with increasing source-detector distance owing to the higher depth sensitivity at higher source-detector distance. The data even at higher source-detector separations is also seen to be contaminated with superficial signal identified by the peak at t=30s. The varying amplitudes of functional and superficial signals at different source-detector distances in Figure 5.5(a) and Figure 5.5(b) is due to the varying sensitivity of intensity and phase measurements at different source-detector distances.

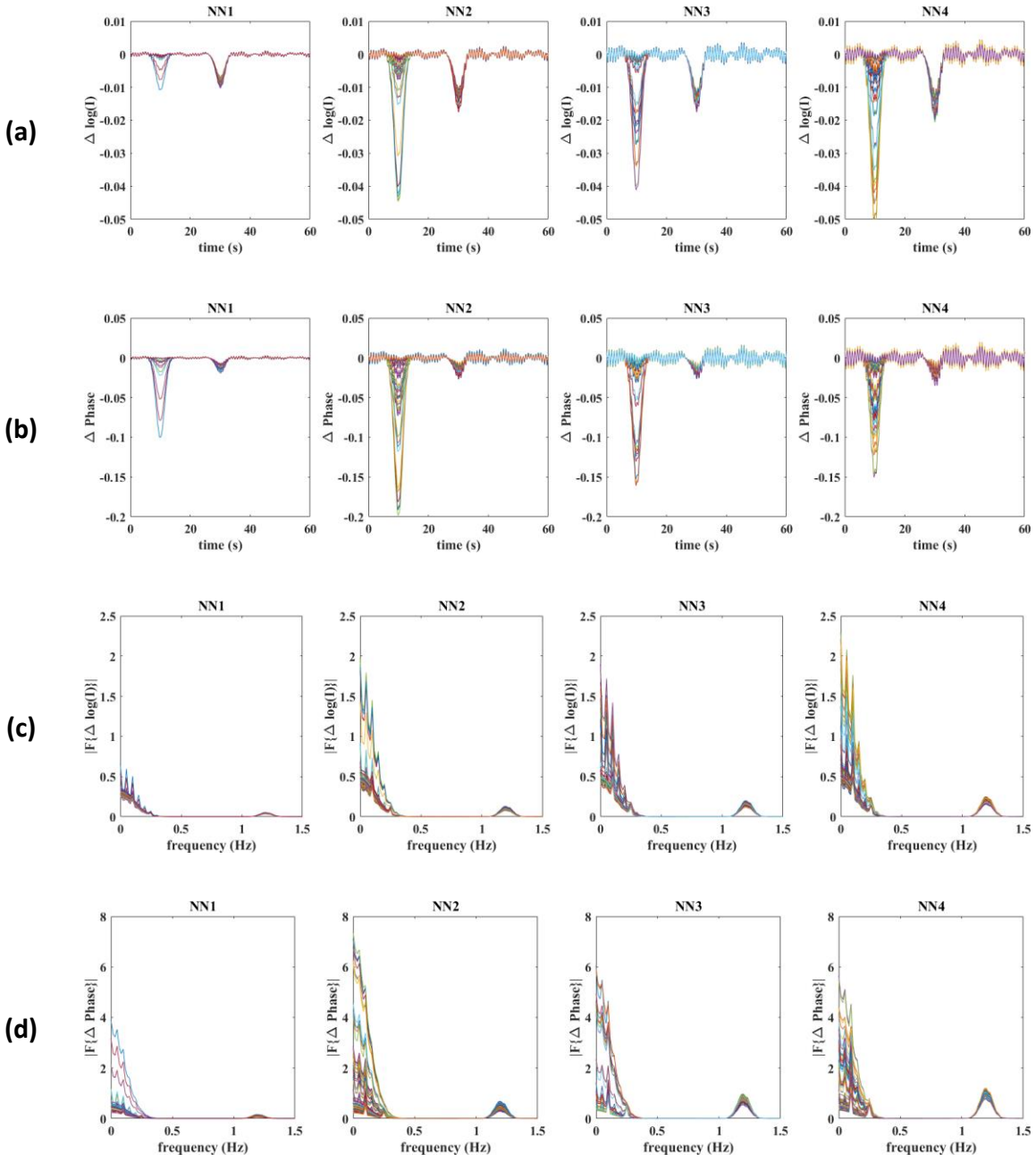

Figure 5.5. (a) and (b) Time traces of intensity and phase measurements without noise at four nearest neighbourhoods modelled at 830 nm; (c) and (d) respective frequency spectra of intensity and phase measurements.

Gaussian random noise is added to the simulated measurements as a function of source-detector distances to model realistic data based on empirically derived noise model. The empirical noise

model was built on data measured using ISS Imagent™ (a frequency domain system console), with six detectors at distances of 18 to 58 mm from source, placed on the visual cortex of the subject. The source modulation frequency was set at 140MHz and data recorded at a sampling rate of 39.74Hz while the subject was at rest and quietly fixated at a blank screen. The noise is then estimated as standard deviation of log mean intensity measurement as intensity noise and of phase difference (in degrees) as the phase noise. It was then fitted to a two-term exponential as a function of source-detector distance details of which can be found elsewhere (71). The calculated noise levels are plotted in Figure 5.6 for the source-detector distances in the measurement setup as shown in Figure 5.2.

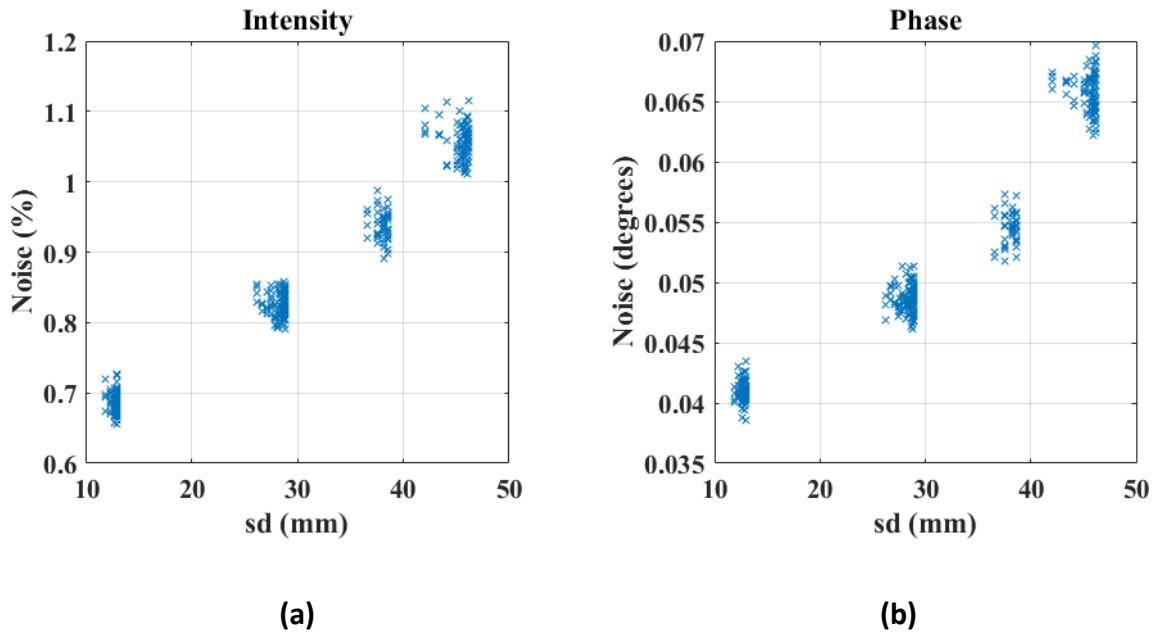

Figure 5.6. Noise levels of intensity and phase measurements as a function of source-detector (sd) distances.

The raw intensity and phase signals with the added noise at the wavelength 830 nm simulated at multiple source-detector distances (grouped as neighbourhoods) are shown in Figure 5.7. To reduce the noise similar to a realistic experimental procedure, the following pre-processing steps are applied before the superficial signal regression procedure:

a) The measurements are high-pass filtered at 0.01 Hz cut-off frequency to remove any drifts present in the signal caused due to the measurement systems (this is not applicable in this simulation experiment) (71).
b) Measurements are then low-pass filtered at 0.1 Hz cut-off frequency to remove the physiological noise i.e., pulse, respiratory and Meyer waves (71).
c) Data is then down-sampled from 40Hz to 1Hz with averaging every 40 samples and thereby greatly reducing random noise present in the signals.
d) To improve the contrast and to further reduce noise, the measurements from multiple repetitions of similar excitations are block-averaged (94). In this case, 10 repetitions are averaged together to increase the signal-to-noise ratio of the data.

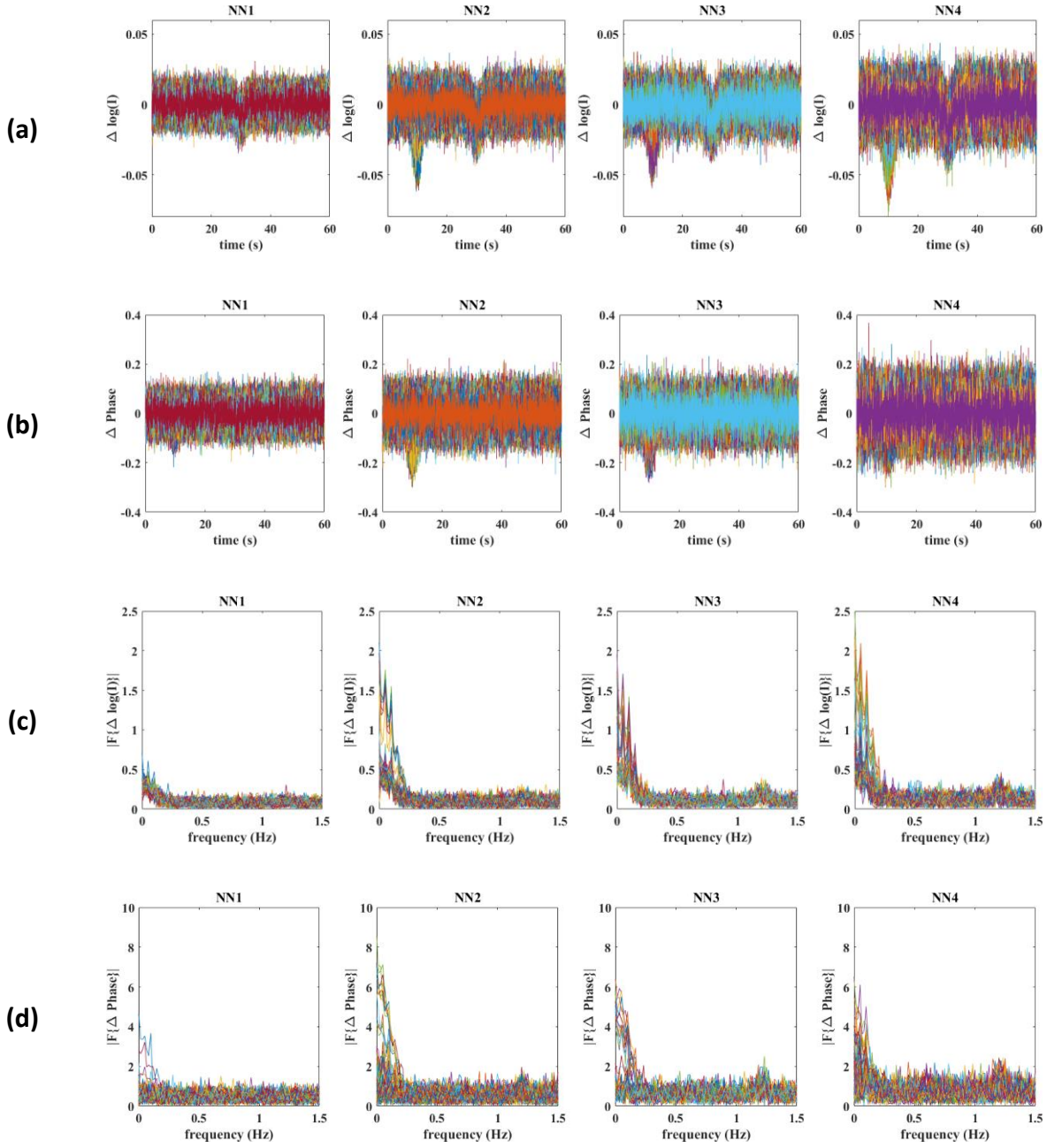

Figure 5.7. (a) and (b) Time traces of intensity and phase measurements with noise added at four nearest neighbourhoods modelled at 830 nm; (c) and (d) respective frequency spectra of intensity and phase measurements.

While the regression of intensity data is well understood (69), the regression of phase signals is the primary objective of this work. It is observed from Figure 5.5 and Figure 5.7 that functional

signal is also seen in the first nearest neighbourhood (NN1) measurements of phase, while the NN1 measurements of intensity signals contain predominantly the superficial signal. Therefore, the following two regression methods are implemented on the phase data:

a) regression of phase signals with the short-distance phase signal (phase based phase regression), and
b) regression of phase signals with the short distance intensity signal (intensity based phase regression).

The regressor signal (short-distance measurement), is regarded as the average of all NN1 measurements of either intensity or phase corresponding to the regression method. The result of regression methods on this pre-processed and noise-reduced intensity and phase data is shown in Figure 5.8.

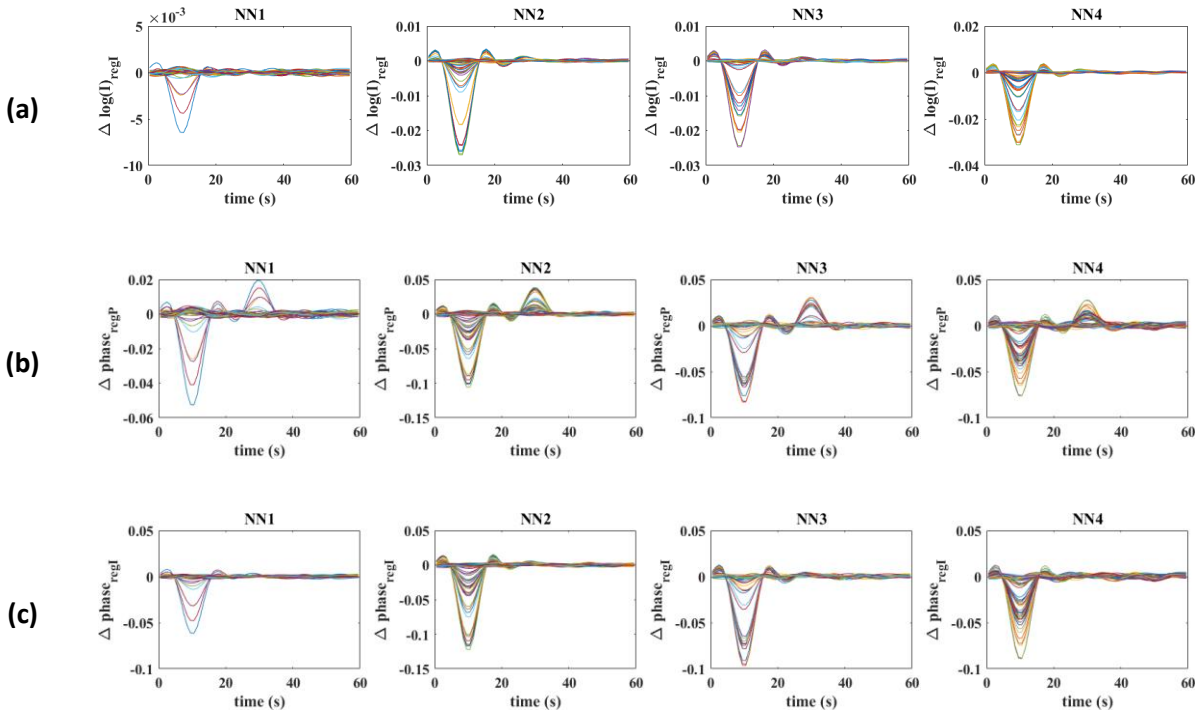

Figure 5.8. (a) Regressed intensity measurements with short-distance intensity measurement, (b) regressed phase measurements with short-distance phase measurement, and (c) regressed phase measurements with short-distance intensity measurement post filtering and all noise-reduction steps.

It can be seen from Figure 5.8(a), that the contamination due to superficial signal at t=30s, is clearly removed from intensity data after regression with short-distance intensity data. The phase signals however retained the superficial signal contamination (t=30s) with a flipped sign after the regression with the short-distance phase measurement as seen in Figure 5.8(b). The regression procedure finds the overlap (cross-correlation coefficient) between the phase measurements and the average of nearest neighbor phase measurement (Δp_{nn}) and subtracts Δp_{nn} of the amplitude proportional to this overlap as defined in equation (5.5). As Δp_{nn} has both superficial signal and a functional component, any phase measurement with a higher relative strength of functional to superficial signal as compared to Δp_{nn} would result in an overlap value

greater than the individual strength of superficial signal present in that phase measurement. Therefore, subtracting a higher amplitude of superficial signal than what is present, we observe a change in sign for superficial signals after regression with Δp_{nn}. However, with the regression of phase signals using short-distance intensity measurement, the superficial signal contamination is clearly seen to be removed in Figure 5.8(c).

To quantitatively represent the reduction of superficial signal contamination, before and after regression, a correlation coefficient between the measurement $\Delta g_i(t)$ and the superficial signal $S(t)$ are calculated as follows:

$$R(g_i, S) = \left| \frac{\langle \Delta g_i, S \rangle}{\sqrt{\langle \Delta g_i, \Delta g_i \rangle} \sqrt{\langle S, S \rangle}} \right|. \tag{5.11}$$

Where, g can represent either intensity $\Delta y_i(t)$, or phase $\Delta p_i(t)$, and the index i represents a measurement channel corresponding to a source-detector combination. The value of $R(g_i, S)$ can vary from 0 to 1 (equivalent to 0 to 100%) which directly represents the amount of superficial signal $S(t)$ present in each of the measurement $\Delta g_i(t)$.

To further observe the amount of superficial signal contamination present exclusively in a subset of the channels that substantially detect the functional activity, a threshold of 90% is considered over the maximum value of $R(g_i, F)$, i.e., $R(g_i, F) > 0.9 \times \max\{R(g_i, F)\}$, where $F(t)$ is the functional signal, and the value $R(g_i, F)$ defines the amount of functional signal present in the measurement similar to equation (5.11). The correlation coefficients $R(g_i, S)$ for

all the measurements before and after regression are shown in Figure 5.9(a), and the correlation coefficients for the channels that detect functional activity are shown in Figure 5.9(b).

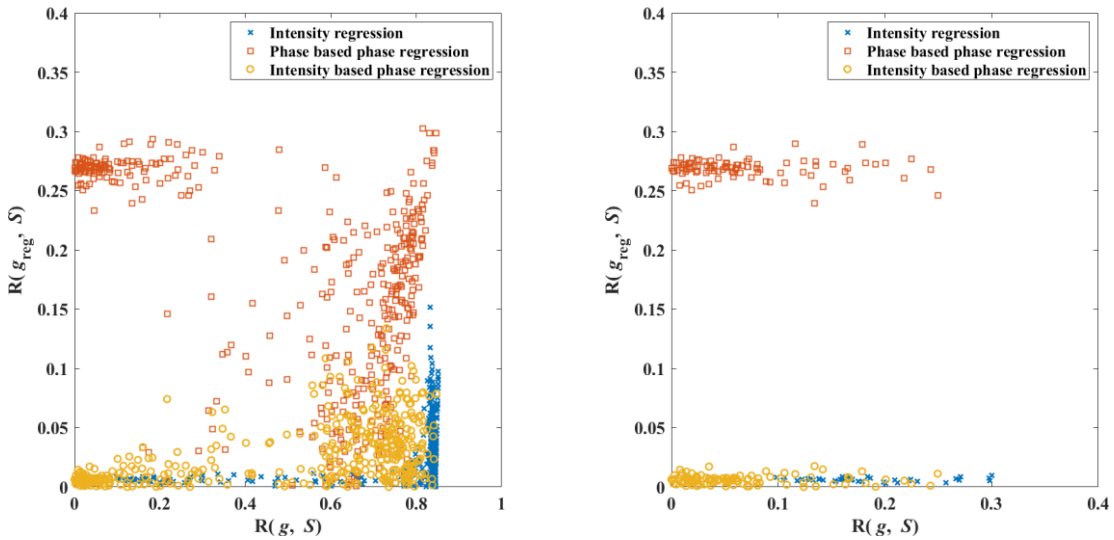

Figure 5.9. Correlation coefficient of all Intensity and Phase measurements with respect to superficial signal, before superficial signal regression vs after superficial signal regression, for (a) all measurement channels (b) for the channels detecting 90% and above of the maximum functional activity.

As the value of the correlation coefficient for all the measurement channels varies from 0 to 1, a root mean square value of $R(g_i, S)$ over all the measurement channels i (or a subset of channels that detect functional activity) is considered to represent an effective strength of the superficial signal in the measurements of either intensity or phase and is shown in Table 5.2 before and after the regression procedure.

Table 5.2. Root mean square (R.M.S) values of correlation coefficients indicating the amount of superficial signal contamination in the intensity and phase measurements before and after regression at 830 nm (the values within brackets correspond to 690 nm).

	Measurement type	Before regression $R(g_i, S)$	After regression $R\left(g_{\mathrm{reg}_i}, S\right)$	Suppression factor
R.M.S calculated on all measurement channels	Intensity	0.7774 (0.8174)	0.0361 (0.0479)	21.5 (17.1)
	Phase	0.5881 (0.5572)	0.2072 (0.0567) (phase based regression)	2.8 (9.8)
			0.0402 (0.0420) (intensity based regression)	14.6 (13.2)
R.M.S calculated on measurement channels with $R(g_i, F) > 0.9\times\max\{R(g_i, F)\}$	Intensity	0.1944 (0.4882)	0.0102 (0.0375)	18.9 (13.0)
	Phase	0.0797 (0.1168)	0.2807 (0.0544) (phase based regression)	0.3 (2.1)
			0.0107 (0.0360) (intensity based regression)	7.4 (3.2)

The suppression factors in Table 5.2 correspond to the ratio of correlation coefficient $R(g_i, S)$ before and after regression, and a value greater than 1 implies the regression procedure has

reduced the superficial signal contamination. The suppression factor for intensity based phase regression is not only greater than 1 but also higher than the phase based phase regression procedure, therefore indicating a better reduction in the superficial signal contamination. A value less than 1 of the suppression factor for phase based phase regression for the channels that detect functional activity highlight that the regression procedure increased the amount of superficial signal contamination in those channels that detect functional activity, the effect of which can be seen in the tomographic reconstruction of the haemoglobin concentrations to identify any recovered functional activations.

Next, the tomographic reconstruction of haemoglobin concentration changes based on the regressed intensity and phase data as shown in Figure 5.8 is performed. The Jacobian $\boldsymbol{J}$ (the sensitivity of intensity and phase with respect to the absorption coefficient at every node in the head model mesh) is constructed (95) for the head-model with background optical properties as given in Table 5.1 on a measurement setup as shown in Figure 5.2 at two wavelengths of 690 nm and 830 nm individually to retrieve the respective absorption changes at these wavelengths. The retrieved absorption changes at each wavelength is then related to the oxygenated haemoglobin (HbO) and deoxygenated haemoglobin (Hb) concentration changes (96):

$$\begin{bmatrix} \Delta\mu_{a_{690}} \\ \Delta\mu_{a_{830}} \end{bmatrix} = \begin{bmatrix} \varepsilon_{\mathrm{HbO},690} & \varepsilon_{\mathrm{HbO},830} \\ \varepsilon_{\mathrm{Hb},690} & \varepsilon_{\mathrm{Hb},830} \end{bmatrix} \begin{bmatrix} \Delta\mathrm{HbO} \\ \Delta\mathrm{Hb} \end{bmatrix} \tag{5.12}$$

The absorption changes ($\Delta\boldsymbol{\mu_a}$) at every node of the head model, is related to the measurement changes ($\Delta\boldsymbol{y}$ and $\Delta\boldsymbol{p}$**),** and the sensitivity matrix as follows:

$$\begin{bmatrix}\Delta \boldsymbol{y} \\ \Delta \boldsymbol{p}\end{bmatrix} = \boldsymbol{J}.\Delta\boldsymbol{\mu_a} = \begin{bmatrix}\boldsymbol{J_y} \\ \boldsymbol{J_p}\end{bmatrix}\Delta\boldsymbol{\mu_a} \tag{5.13}$$

The Jacobian $\boldsymbol{J}$ consists of both the sensitivity of intensity ($\boldsymbol{J_y}$) and phase sensitivities ($\boldsymbol{J_p}$) which are different in their magnitude (71). To retrieve the absorption changes, a single step inversion of the Jacobian is performed together with Tikhonov regularization, to compensate for the ill-posedness and ill-conditioning of the problem (31).

$$\Delta\boldsymbol{\mu_a} = \boldsymbol{J}^{\sim\mathbf{1}}\begin{bmatrix}\Delta \boldsymbol{y} \\ \Delta \boldsymbol{p}\end{bmatrix} = \boldsymbol{J}^{\mathbf{T}}(\boldsymbol{J}\boldsymbol{J}^{\mathbf{T}} + \alpha\mathbf{I})^{-\mathbf{1}}\begin{bmatrix}\Delta \boldsymbol{y} \\ \Delta \boldsymbol{p}\end{bmatrix} \tag{5.14}$$

Here, α is the regularization factor which is considered as $\alpha = \Lambda \max[\mathrm{diag}(\boldsymbol{J}\boldsymbol{J}^{\mathrm{T}})]$, with the weight factor $\Lambda = 0.01$ to smooth the parameter recovery (94). The regularization is implemented separately for the intensity Jacobian and phase Jacobian kernels (71). The recovered absorption changes at two wavelengths are then used to retrieve the corresponding changes in haemoglobin concentrations using equation (5.12).

The recovered focal activation using the intensity data regressed with short-separation intensity measurement (intensity based intensity regression) and phase data regressed with short-separation phase measurement (phase based phase regression), at t=10s is shown in Figure 5.10. This is achieved by spatially thresholding the recovered haemoglobin concentration to 50% of maximum change. Therefore, the size of the observed activation in Figure 5.10 indicates the

FWHM of the recovery which is found to be 10.1mm given the 5mm (2.5 mm radius) of ground-truth focal activation. Similar recovered focal activation is observed using the intensity data and phase data both regressed with short-separation intensity measurement (intensity based intensity regression and intensity based phase regression), at t=10s, also with an FWHM of 10.1mm.

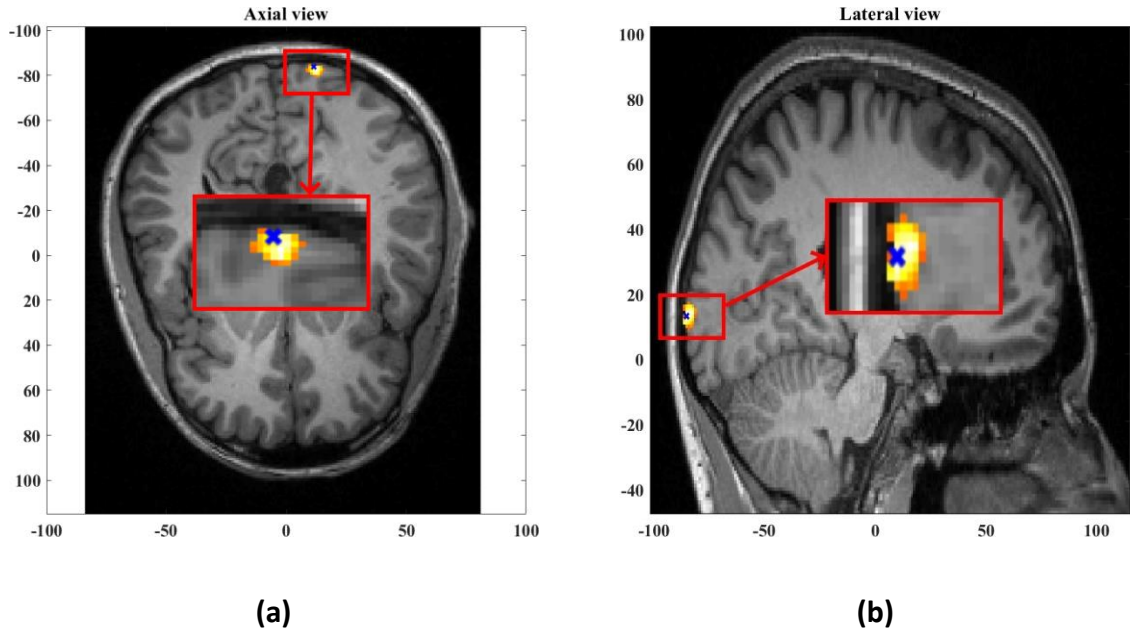

Figure 5.10. Axial view at z=11.8mm (a) and lateral view at x=12.5mm (b) of the recovered oxy-haemoglobin at t=10s showing a positive change, reconstructed using the intensity data regressed with short-separation intensity measurement and phase data regressed with short-separation phase measurement. The center of ground-truth focal activation at (11.5, -85, 10.7) is shown by the blue 'x' mark.

However, at t=30s the recovered haemoglobin changes show a 'false' focal activation for phase based phase regression method as shown in Figure 5.11. Indicating a false positive. The maximum absolute change observed for the recovered oxy-haemoglobin concentration is seen as a negative change as shown in the data in Figure 5.8. The focal activation recovered and shown in

Figure 5.11 indicates a negative change of oxy-haemoglobin concentration thresholded at 50% of maximum absolute change, with an FWHM of 9mm. The oxy-haemoglobin recovery for intensity based phase regression at t=30s however does not show any specific focal activation recovery which is also in-line with the data observed in Figure 5.8.

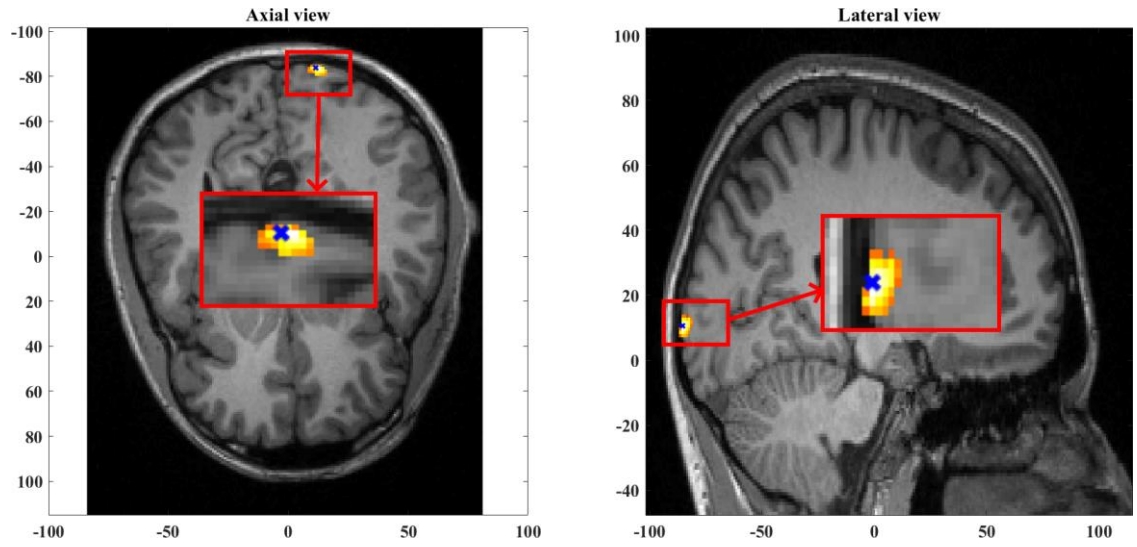

(a) (b)

Figure 5.11. Axial view at z=9.8mm (a) and lateral view at x=13.5mm (b) of the false-positive recovery of oxy-haemoglobin at t=30s showing a negative change, reconstructed using the intensity data regressed with short-separation intensity measurement and phase data regressed with short-separation phase measurement. The center of ground-truth focal activation (11.5, -85, 10.7), occurring at t=10s is shown by the blue 'x' mark.

To further substantiate the presence of superficial signal contamination in phase based phase regression in comparison to the intensity based phase regression, the recovered oxy-haemoglobin in the region of ground-truth activation, i.e., within 2.5 mm radius from (11.5, -85, 10.7) is shown in Figure 5.12 and Figure 5.13. The negative side lobes on either side of the peak at t=10s is simply an effect of using the band-pass filter on a Gaussian signal. The negative peak of oxy-haemoglobin in Figure 5.12, at t=30s, clearly indicates the direct effect of superficial signal

contamination introduced due to the phase based regression method appearing in not just the cerebral region but in the locality of ground-truth activation and therefore leading to false positives.

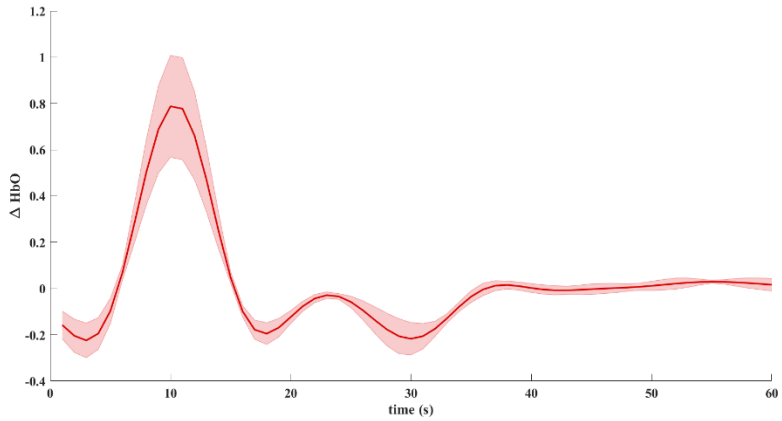

Figure 5.12. Temporal plot of normalized oxy-haemoglobin recovery in the region of ground-truth focal activation for phase based phase regression method.

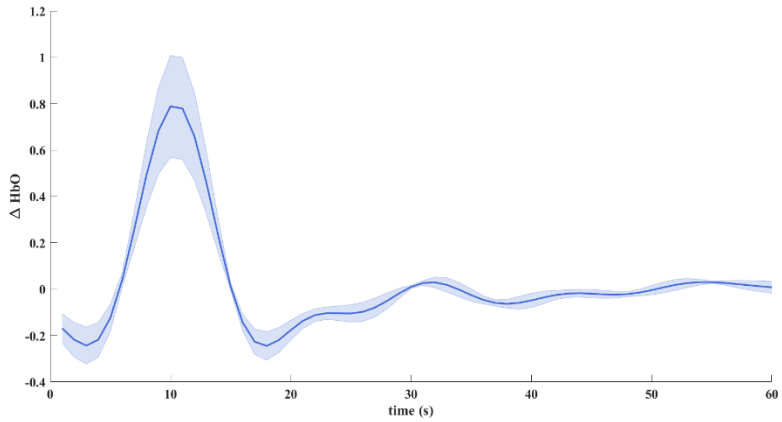

Figure 5.13. Temporal plot of normalized oxy-haemoglobin recovery in the region of ground-truth focal activation for intensity based phase regression method

5.4. Discussion

Recent developments in FD-DOT imaging studies have shown that the use of phase data along with intensity data significantly improves the image quality. The higher depth sensitivity of phase signal relative to intensity signal enables a significantly better localization of focal activations especially in depth using an FD-DOT system, out-performing a CW-DOT system. However, performing similar pre-processing techniques of signal regression that are implemented in a CW-DOT system without careful observation will lead to unintended and misleading haemodynamic activity, and therefore misinterpreting the results.

While the superficial signal regression for intensity data is well understood, and utilized often to improve the image quality, the signal regression for phase data however is not as straight-forward or well understood. The very advantageous aspect of higher sensitivity of phase signal to deeper tissue can lead to even the short-distance phase measurement detecting functional activity from deeper tissue. Therefore, any regression of phase signal using this short-distance phase measurement (phase based phase regression) would not completely remove the superficial signal contamination and also may additionally cause reduction in the strength of the recovered functional signal. To this end, superficial signal regression of phase data using short-distance intensity measurement (intensity based phase regression) is shown to more accurately remove the superficial signal contamination.

Utilizing realistic head model data, Figure 5.5(b) highlights the presence of functional signal, originated in the cerebral region at a depth of 10mm from surface, even in the short-distance phase signals, while the short-distance intensity signals mostly contain the superficial signal.

Therefore, given the superficial signal being uncorrelated to the functional signal, the regressor signal in phase based phase regression method (i.e., short-distance phase measurement) is still correlated with the functional signal. This is unlike the regressor signal in intensity based phase regression method (i.e., short-distance intensity measurement) which is uncorrelated to the functional signal which will affect the regression procedure as highlighted in section 5.2. This is seen in the results of Figure 5.8(b), where an unbalanced regression using short-distance phase measurement causes a negative effect of signal contamination (inverted peak at t=30s) in the phase data. It is also seen to reduce the functional component in the signals (decreased magnitude at t=10s, as compared to raw data in Figure 5.5(b)) that can cause reduction in the contrast of recovered functional activation; the stronger the functional component in the regressor signal (short distance phase measurement) the greater is the reduction in the functional component in all the measurements post regression. But using short distance intensity measurement to regress phase in Figure 5.8(c) has proven to be efficient in its performance both by retaining a higher functional component and by suppressing the superficial signal component at t=30s.

The strength of superficial signal present in intensity and phase measurements as defined by the correlation coefficient shown in Figure 5.9 indicate that the phase based phase regression retains a higher strength of the superficial signal in the regressed data as compared to intensity regression and intensity based phase regression procedures. The RMS value of the correlation coefficient (calculated on all measurement channels) shown in Table 5.2, before and after the regression indicates the reduction in superficial signal contamination at 830 nm by factor 2.8 for phase based phase regression (13% of what is observed in intensity regression), and 14.6 for

intensity based phase regression (68% of what is observed in intensity regression), demonstrating the improvement in the regression of phase measurements using short-separation intensity measurement. The corresponding suppression factors at 690 nm are 9.8 for phase based phase regression (57% of what is observed in intensity regression) and 13.2 for intensity based phase regression (77% of what is observed in intensity regression). The relatively higher suppression factors for phase based phase regression at 690 nm compared to those at 830 nm is because the functional signal present in the short-separation phase measurement at 690 nm is relatively lower than that at 830 nm, and therefore making the phase regressor signal more uncorrelated to the functional signal. The lower functional activity at 690 nm corresponds to the lower deoxy-haemoglobin change i.e., 0.47 times that of oxy-haemoglobin change, as the signal at 690 nm is more sensitive to deoxy-haemoglobin and at 830 nm it is more sensitive to oxy-haemoglobin.

The DOT parameter recovery based on this regressed data is seen in Figure 5.10. The focal activations at t=10s for both phase based phase regression and intensity based phase regression methods (together with regressed intensity data in both cases) are found to have maxima-location of (12.5, -83.3, 11.8), at a distance of 2.2mm from the center of ground-truth activation, and an FWHM of 10.1 mm corresponding to a ground-truth width of 5mm of the focal activation blob. At t=30s however, the DOT parameter recovery of haemodynamic activity for phase based phase regression method, as seen in Figure 5.11, estimated a false positive focal activation at a maxima-location of (13.5, -85.3, 9.8), also at a distance of 2.2 mm from the center of ground-truth focal activation (that occurred only at t=10s) and an FWHM of 9mm.

The cause of such false positive can be explained by considering a set ‘S’ of measurement channels that prominently detect the functional signals that originate in the region R. Conversely,

any change in these ‘S’ set of measurement channels corresponds to a prospective recovery in the region R. The regressor signal of phase which contains both functional and superficial signal content, would cause a new peak corresponding to superficial signal, if it is absent initially in the given ‘S’ set of measurements, which would therefore result in a recovery in the original activation region ‘R’. Thus, instead of removing superficial signal contamination, the phase based regression approach would cause the superficial signal to directly contaminate the haemodynamic recovery in the cerebral region. This is further substantiated by Figure 5.12 and Figure 5.13 showing the recovered oxy-haemoglobin concentration over the entire period of time in the original focal-activation region ‘R’, where it is seen that a negative peak at t=30s for phase based phase regression method showing the superficial signal contamination, while the oxy-haemoglobin recovery for intensity based phase regression method did not show any such peaks at t=30s.

5.5. Conclusions

This work has demonstrated the adverse effects of implementing a phase-based phase regression in FD-DOT and shows the existence of superficial contamination in such cases even after regression, due to the possibility of the presence of the functional signal in phase data even at shorter SD separations, while also reducing the functional component in all of the measurements, which can lead to a reduction in the contrast of recovered focal activations. An alternative to the intensity-based phase regression method is proposed and demonstrated to correctly remove superficial signal contamination.

This type of regression plays a significant role in any FD-based methods in which signal regression is implemented, such as FD-DOT. The same theory can also be extended for time resolved systems (TRS) in which the moments-based analysis is implemented to observe haemodynamic activity, as the first-order moment of the distribution of time of flight of photons is similar to the phase measurement in FD NIRS systems and can also become significant to other data types (higher order moments in TRS) that have a higher sensitivity toward deeper tissue and therefore require an intensity-based (total photon count in TRS) regression approach instead of using the same data type for superficial signal regression. This needs further investigation and is the subject of further studies.

Chapter 6

CONCLUSIONS AND FUTURE WORK

6.1. Conclusions

The current state of NIRS in the application of monitoring TBI patients is presented together with the short-comings in the existing parameter recovery methods. New computational methods have been proposed and demonstrated to overcome the existing challenges with NIRS in the context of TBI addressing the following hypotheses:

1. Measurement of TOI using NIRS requires absorption coefficient at least two wavelengths. While the conventional methods of continuous wave NIRS cannot extract (de-couple) absorption and scattering properties of the tissue from intensity only measurements at each wavelength, the use of multi-spectral information can help in extracting absorption and scattering properties by spectrally constraining the problem and therefore estimating more accurate TOI values.
2. The application of multi-distance broadband intensity measurements can distinguish between cerebral and extra-cerebral tissue's absorption and scattering parameters.
3. The use of layered head-model based parameter recovery methods greatly improves the accuracy of cerebral tissue parameters compared to the conventionally used layered slab models.

4. While the use of intensity and phase measurements can greatly improve the localization and resolution of brain activation maps, the superficial signal contamination still poses an issue with its conventional application on phase measurements but alternative regression method can be developed for the phase measurements.

The application of spectrally constrained parameter recovery has been shown to separate the absorption and scattering properties from intensity only measurements to get more accurate estimates of TOI. This was otherwise not possible and the estimation of TOI relied on the assumption of scattering properties causing uncertainty in the results. It also addresses another major challenge for a CW system i.e., superficial signal contamination.

In reference to hypotheses 2 and 3, the non-uniqueness in CW-NIRS is primarily addressed showing that a regional constraint on the parameter recovery leads to unique parameter set for the given measurement set of intensities. A two-layered parameter recovery method using multi-distance broadband CW intensity measurements is proposed and demonstrated to recover the absolute haemoglobin concentrations, scattering parameters, and the superficial tissue thickness of a human head through simulations across different head models corresponding to different subjects. A practical implementation of this approach with real human subject data measured on the forehead is presented and has shown good repeatability in the recovered tissue parameters over three days. Finally, this work demonstrates the ability of multi-distance CW broadband intensity data to retrieve or separate the extra-cerebral tissue parameters and the cerebral tissue parameters using model based parameter recovery and that such an approach is more accurate than recovering bulk tissue parameters.

With regards to the fourth hypothesis, the adverse effects of implementing superficial signal regression on phase data using phase measurement corresponding to short source-detector distance are demonstrated, which clearly shows the existence of superficial contamination in such cases even after regression, due to the possibility of the presence of functional signal in phase data even at shorter source-detector separations, while also reducing the functional component in all the measurements which can lead to a reduction in the contrast of recovered focal activations. An alternative of intensity based phase regression method is also proposed and demonstrated to properly remove superficial signal contamination. This type of regression plays a significant role in any FD based methods, where signal regression is implemented such as FD-DOT.

6.2. Future work

This research provides the computational methodologies to overcome the major challenges in near-infrared spectroscopy aimed towards cerebral monitoring for TBI patients, yet there is scope for further research.

The work in Chapter 3 presents the optimal wavelength set for the spectrally constrained SRS approach for the chromophores oxy and deoxy-haemoglobin and the wavelength optimization considers the wavelength range where these chromophores are the major contributors towards light absorption. To include other chromophores such as water,

cytochrome c oxidase and others the optimization process needs to be reimplemented including the full wavelength range where these chromophores are dominant absorbing constituents.

While the accuracy of model-based broadband spectral recovery of tissue parameters is demonstrated in Chapter 4 using computational simulations on two layered models, further study is required to investigate its applicability to extend the approach for five-layered geometry of head. Furthermore, although the broadband intensity data provides more information, the inverse problem of parameter recovery process is computationally expensive due to the modelling of data at large number of wavelengths. Therefore, further analysis is also required to understand if an optimal wavelength set can provide a better model-based recovery of cerebral and extra-cerebral tissues.

The superficial signal regression implemented on phase measurements in Chapter 5 can also be extended for NIRS systems like TRS where the moments based analysis is implemented to observe haemodynamic activity (97), as the first-order moment of the distribution of time of flight of photons is similar to the phase measurement in FD NIRS systems. This approach can also be significant to other data types (ex: higher order moments in TRS) that have a higher sensitivity towards deeper tissue and therefore require an intensity based (equivalent to the total photon count in TRS) regression approach instead of using the same data type for superficial signal regression. This is the subject of future studies and needs further investigation.

Finally, while the proposed computational methods improve the existing NIRS techniques to overcome their major challenges without any requirement on changes to the existing instrumentation, to validate the applicability of these NIRS techniques in clinical environment for monitoring TBI patients, rigorous clinical validation studies are eventually required, and this

research work provides the proof-of-concept and serves as the beginning step towards its clinical application.

REFERENCES

1. Boniface R, Lugazia ER, Ntungi AM, Kiloloma O. Management and outcome of traumatic brain injury patients at Muhimbili Orthopaedic Institute Dar es Salaam, Tanzania. The Pan African Medical Journal. 2017;26.
2. Hyder AA, Wunderlich CA, Puvanachandra P, Gururaj G, Kobusingye OC. The impact of traumatic brain injuries: A global perspective. NeuroRehabilitation. 2007;22:341-53.
3. Murray GD, Teasdale GM, Braakman R, Cohadon F, Dearden M, Iannotti F, et al. The European Brain Injury Consortium Survey of Head Injuries. Acta Neurochirurgica. 1999;141(3):223-36.
4. Maloney-Wilensky E, Gracias V, Itkin A, Hoffman K, Bloom S, Yang W, et al. Brain tissue oxygen and outcome after severe traumatic brain injury: a systematic review. Critical care medicine. 2009;37(6):2057-63.
5. White H, Venkatesh B. Oxford textbook of neurocritical care, chapter 17: traumatic brain injury. Oxford textbook of neurocritical care: Oxford University Press; 2016. p. 213, 5.
6. Torricelli A, Contini D, Pifferi A, Caffini M, Re R, Zucchelli L, et al. Time domain functional NIRS imaging for human brain mapping. NeuroImage. 2014;85:28-50.
7. McDonald BC, Saykin AJ, McAllister TW. Functional MRI of mild traumatic brain injury (mTBI): progress and perspectives from the first decade of studies. Brain Imaging Behav. 2012;6(2):193-207.
8. Sykora M, Czosnyka M, Liu X, Donnelly J, Nasr N, Diedler J, et al. Autonomic Impairment in Severe Traumatic Brain Injury: A Multimodal Neuromonitoring Study. Critical care medicine. 2016;44(6):1173-81.
9. Signorini DF, Andrews PJ, Jones PA, Wardlaw JM, Miller JD. Adding insult to injury: the prognostic value of early secondary insults for survival after traumatic brain injury. J Neurol Neurosurg Psychiatry. 1999;66(1):26-31.
10. Fletcher JJ, Bergman K, Blostein PA, Kramer AH. Fluid balance, complications, and brain tissue oxygen tension monitoring following severe traumatic brain injury. Neurocrit Care. 2010;13(1):47-56.
11. Maas AI, Stocchetti N, Bullock R. Moderate and severe traumatic brain injury in adults. Lancet Neurology. 2008;7(8):728-41.
12. Ract C, Le Moigno S, Bruder N, Vigue B. Transcranial Doppler ultrasound goal-directed therapy for the early management of severe traumatic brain injury. Intensive Care Med. 2007;33(4):645-51.
13. Davies D, Clancy M, Su Z, Denghani H, Belli A. Choosing a cerebral near-infrared spectroscopy system for use in traumatic brain injury: deriving the ideal source detector layout. Crit Care. 2014;18(Suppl 1):P468-P.
14. Boushel R, Langberg H, Olesen J, Gonzales-Alonzo J, Bulow J, Kjaer M. Monitoring tissue oxygen availability with near infrared spectroscopy (NIRS) in health and disease. Scand J Med Sci Sports. 2001;11(4):213-22.
15. Davies DJ, Su Z, Clancy MT, Lucas SJ, Dehghani H, Logan A, et al. Near-Infrared Spectroscopy in the Monitoring of Adult Traumatic Brain Injury: A Review. J Neurotrauma. 2015;32(13):933-41.
16. Budohoski KP, Zweifel C, Kasprowicz M, Sorrentino E, Diedler J, Brady KM, et al. What comes first? The dynamics of cerebral oxygenation and blood flow in response to changes in arterial pressure and intracranial pressure after head injury. Br J Anaesth. 2012;108(1):89-99.
17. Weerakkody RA, Czosnyka M, Zweifel C, Castellani G, Smielewski P, Brady K, et al. Near infrared spectroscopy as possible non-invasive monitor of slow vasogenic ICP waves. Acta Neurochir Suppl. 2012;114:181-5.

18. Leal-Noval SR, Cayuela A, Arellano-Orden V, Marin-Caballos A, Padilla V, Ferrandiz-Millon C, et al. Invasive and noninvasive assessment of cerebral oxygenation in patients with severe traumatic brain injury. Intensive Care Med. 2010;36(8):1309-17.
19. Durduran T, Yodh AG. Diffuse correlation spectroscopy for non-invasive, micro-vascular cerebral blood flow measurement. NeuroImage. 2014;85:51-63.
20. Raboel PH, Bartek J, Jr., Andresen M, Bellander BM, Romner B. Intracranial Pressure Monitoring: Invasive versus Non-Invasive Methods-A Review. Crit Care Res Pract. 2012;2012:950393.
21. Fischer JB, Ghouse A, Tagliabue S, Maruccia F, Rey-Perez A, Báguena M, et al., editors. Non-invasive estimation of intracranial pressure by diffuse correlation spectroscopy. Biophotonics Congress: Biomedical Optics 2020 (Translational, Microscopy, OCT, OTS, BRAIN); 2020 2020/04/20; Washington, DC: Optical Society of America.
22. Farzam P, Sutin J, Wu K-C, Zimmermann B, Tamborini D, Dubb J, et al. Fast diffuse correlation spectroscopy (DCS) for non-invasive measurement of intracranial pressure (ICP) (Conference Presentation): SPIE; 2017.
23. Thavasothy M, Broadhead M, Elwell C, Peters M, Smith M. A comparison of cerebral oxygenation as measured by the NIRO 300 and the INVOS 5100 Near-Infrared Spectrophotometers. Anaesthesia. 2002;57(10):999-1006.
24. Robertson CS, Zager EL, Narayan RK, Handly N, Sharma A, Hanley DF, et al. Clinical evaluation of a portable near-infrared device for detection of traumatic intracranial hematomas. J Neurotrauma. 2010;27(9):1597-604.
25. Ghosh A, Elwell C, Smith M. Review article: cerebral near-infrared spectroscopy in adults: a work in progress. Anesth Analg. 2012;115(6):1373-83.
26. Taroni P, Pifferi A, Torricelli A, Comelli D, Cubeddu R. In vivo absorption and scattering spectroscopy of biological tissues. Photochem Photobiol Sci. 2003;2(2):124-9.
27. Mourant JR, Fuselier T, Boyer J, Johnson TM, Bigio IJ. Predictions and measurements of scattering and absorption over broad wavelength ranges in tissue phantoms. Applied optics. 1997;36(4):949-57.
28. van Staveren HJ, Moes CJM, van Marie J, Prahl SA, van Gemert MJC. Light scattering in lntralipid-10% in the wavelength range of 400–1100 nm. Applied optics. 1991;30(31):4507-14.
29. Yamada Y, Suzuki H, Yamashita Y. Time-Domain Near-Infrared Spectroscopy and Imaging: A Review. Applied Sciences. 2019;9(6):1127.
30. Arridge SR. Optical tomography in medical imaging. Inverse Problems. 1999;15(2):R41-R93.
31. Dehghani H, Eames ME, Yalavarthy PK, Davis SC, Srinivasan S, Carpenter CM, et al. Near infrared optical tomography using NIRFAST: Algorithm for numerical model and image reconstruction. Communications in numerical methods in engineering. 2008;25(6):711-32.
32. Schweiger M, Arridge SR, Hiraoka M, Delpy DT. The finite element method for the propagation of light in scattering media: boundary and source conditions. Medical physics. 1995;22(11 Pt 1):1779-92.
33. Wang X, Gong Y, Song D, Wu Z. The Study of the Diffuse Equation About a Three-Layered Matched Medium. International Journal of Infrared and Millimeter Waves. 2004;25(10):1545-56.
34. Pucci O, Toronov V, St. Lawrence K. Measurement of the optical properties of a two-layer model of the human head using broadband near-infrared spectroscopy. Applied optics. 2010;49(32):6324-32.
35. Li A, Kwong R, Cerussi A, Merritt S, Hayakawa C, Tromberg B. Method for recovering quantitative broadband diffuse optical spectra from layered media. Applied optics. 2007;46(21):4828-33.
36. Kienle A, Patterson MS, Dögnitz N, Bays R, Wagnières G, van den Bergh H. Noninvasive determination of the optical properties of two-layered turbid media. Applied optics. 1998;37(4):779-91.
37. Arridge SR, Schotland JC. Optical tomography: forward and inverse problems. Inverse Problems. 2009;25(12):59.
38. Arridge SR, Schweiger M, Hiraoka M, Delpy DT. A finite element approach for modeling photon transport in tissue. Medical physics. 1993;20(2 Pt 1):299-309.

39. Chen J, Intes X. Time-gated perturbation Monte Carlo for whole body functional imaging in small animals. Opt Express. 2009;17(22):19566-79.
40. Lu W, Duan J, Veesa JD, Styles IB. New nonlocal forward model for diffuse optical tomography. Biomed Opt Express. 2019;10(12):6227-41.
41. Sassaroli A, Martelli F, Fantini S. Perturbation theory for the diffusion equation by use of the moments of the generalized temporal point-spread function. III. Frequency-domain and time-domain results. J Opt Soc Am A Opt Image Sci Vis. 2010;27(7):1723-42.
42. Scholkmann F, Kleiser S, Metz AJ, Zimmermann R, Mata Pavia J, Wolf U, et al. A review on continuous wave functional near-infrared spectroscopy and imaging instrumentation and methodology. NeuroImage. 2014;85 Pt 1:6-27.
43. Yalavarthy PK, Pogue BW, Dehghani H, Paulsen KD. Weight-matrix structured regularization provides optimal generalized least-squares estimate in diffuse optical tomography. Medical physics. 2007;34(6):2085-98.
44. Fantini S, Franceschini MA, Fishkin JB, Barbieri B, Gratton E. Quantitative determination of the absorption spectra of chromophores in strongly scattering media: a light-emitting-diode based technique. Applied optics. 1994;33(22):5204-13.
45. Hallacoglu B, Sassaroli A, Fantini S. Optical Characterization of Two-Layered Turbid Media for Non-Invasive, Absolute Oximetry in Cerebral and Extracerebral Tissue. PLOS ONE. 2013;8(5):e64095.
46. Applegate MB, Roblyer D. Multi-distance diffuse optical spectroscopy with a single optode via hypotrochoidal scanning. Optics letters. 2018;43(4):747-50.
47. Boas D, Gaudette T, Arridge S. Simultaneous imaging and optode calibration with diffuse optical tomography. Opt Express. 2001;8(5):263-70.
48. Dehghani H, Pogue BW, Poplack SP, Paulsen KD. Multiwavelength three-dimensional near-infrared tomography of the breast: initial simulation, phantom, and clinical results. Applied optics. 2003;42(1):135-45.
49. Michaelsen KE, Krishnaswamy V, Shi L, Vedantham S, Poplack SP, Karellas A, et al. Calibration and optimization of 3D digital breast tomosynthesis guided near infrared spectral tomography. Biomed Opt Express. 2015;6(12):4981-91.
50. Jobsis FF. Noninvasive, infrared monitoring of cerebral and myocardial oxygen sufficiency and circulatory parameters. Science. 1977;198(4323):1264-7.
51. Patterson MS, Schwartz E, Wilson BC. Quantitative Reflectance Spectrophotometry For The Noninvasive Measurement Of Photosensitizer Concentration In Tissue During Photodynamic Therapy: SPIE; 1989. 8 p.
52. Suzuki S, Takasaki S, Ozaki T, Kobayashi Y. Tissue oxygenation monitor using NIR spatially resolved spectroscopy: SPIE; 1999. 11 p.
53. Fantini S, Franceschini M-A, Maier J, Walker S, Barbieri B, Gratton E. Frequency-domain multichannel optical detector for noninvasive tissue spectroscopy and oximetry. Optical Engineering. 1995;34(1).
54. Patterson MS, Chance B, Wilson BC. Time resolved reflectance and transmittance for the non-invasive measurement of tissue optical properties. Applied optics. 1989;28(12):2331-6.
55. Puszka A, Di Sieno L, Mora AD, Pifferi A, Contini D, Planat-Chretien A, et al. Spatial resolution in depth for time-resolved diffuse optical tomography using short source-detector separations. Biomed Opt Express. 2015;6(1):1-10.
56. Puszka A, Di Sieno L, Mora AD, Pifferi A, Contini D, Boso G, et al. Time-resolved diffuse optical tomography using fast-gated single-photon avalanche diodes. Biomed Opt Express. 2013;4(8):1351-65.
57. Pifferi A, Contini D, Mora AD, Farina A, Spinelli L, Torricelli A. New frontiers in time-domain diffuse optics, a review. J Biomed Opt. 2016;21(9):091310.

58. Zouaoui J, Di Sieno L, Herve L, Pifferi A, Farina A, Mora AD, et al. Chromophore decomposition in multispectral time-resolved diffuse optical tomography. Biomed Opt Express. 2017;8(10):4772-87.
59. Wolf M, Ferrari M, Quaresima V. Progress of near-infrared spectroscopy and topography for brain and muscle clinical applications. J Biomed Opt. 2007;12(6):062104.
60. Clancy M, Belli A, Davies D, Lucas SJE, Su Z, Dehghani H. Improving the quantitative accuracy of cerebral oxygen saturation in monitoring the injured brain using atlas based Near Infrared Spectroscopy models. Journal of Biophotonics. 2016;9(8):812-26.
61. Arridge SR, Lionheart WR. Nonuniqueness in diffusion-based optical tomography. Optics letters. 1998;23(11):882-4.
62. Corlu A, Choe R, Durduran T, Lee K, Schweiger M, Arridge SR, et al. Diffuse optical tomography with spectral constraints and wavelength optimization. Applied optics. 2005;44(11):2082-93.
63. Corlu A, Durduran T, Choe R, Schweiger M, Hillman EM, Arridge SR, et al. Uniqueness and wavelength optimization in continuous-wave multispectral diffuse optical tomography. Optics letters. 2003;28(23):2339-41.
64. Eames ME, Wang J, Pogue BW, Dehghani H. Wavelength band optimization in spectral near-infrared optical tomography improves accuracy while reducing data acquisition and computational burden. Journal of biomedical optics. 2008;13(5):054037-.
65. Jacques SL. Corrigendum: Optical properties of biological tissues: a review. Physics in Medicine and Biology. 2013;58(14):5007-8.
66. Matcher SJ, Kirkpatrick PJ, Nahid K, Cope M, Delpy DT. Absolute quantification methods in tissue near-infrared spectroscopy: SPIE; 1995. 10 p.
67. Gagnon L, Cooper RJ, Yucel MA, Perdue KL, Greve DN, Boas DA. Short separation channel location impacts the performance of short channel regression in NIRS. NeuroImage. 2012;59(3):2518-28.
68. Gagnon L, Yücel MA, Boas DA, Cooper RJ. Further improvement in reducing superficial contamination in NIRS using double short separation measurements. NeuroImage. 2014;85 Pt 1(0 1):127-35.
69. Zeff BW, White BR, Dehghani H, Schlaggar BL, Culver JP. Retinotopic mapping of adult human visual cortex with high-density diffuse optical tomography. Proceedings of the National Academy of Sciences of the United States of America. 2007;104(29):12169-74.
70. Gregg NM, White BR, Zeff BW, Berger AJ, Culver JP. Brain specificity of diffuse optical imaging: improvements from superficial signal regression and tomography. Front Neuroenergetics. 2010;2.
71. Doulgerakis M, Eggebrecht AT, Dehghani H. High-density functional diffuse optical tomography based on frequency-domain measurements improves image quality and spatial resolution. Neurophotonics. 2019;6(3):035007.
72. Farrell TJ, Wilson BC, Patterson MS. The use of a neural network to determine tissue optical properties from spatially resolved diffuse reflectance measurements. Physics in Medicine and Biology. 1992;37(12):2281-6.
73. Flexman ML, Kim HK, Stoll R, Khalil MA, Fong CJ, Hielscher AH. A wireless handheld probe with spectrally constrained evolution strategies for diffuse optical imaging of tissue. The Review of scientific instruments. 2012;83(3):033108.
74. Liu H, Boas DA, Zhang Y, Yodh AG, Chance B. Simplified approach to characterize optical properties and blood oxygenation in tissue using continuous near-infrared light: SPIE; 1995. 7 p.
75. Dehghani H, White BR, Zeff BW, Tizzard A, Culver JP. Depth sensitivity and image reconstruction analysis of dense imaging arrays for mapping brain function with diffuse optical tomography. Applied optics. 2009;48(10):D137-43.
76. Spinelli L, Zucchelli L, Contini D, Caffini M, Mehler J, Flo A, et al. In vivo measure of neonate brain optical properties and hemodynamic parameters by time-domain near-infrared spectroscopy. Neurophotonics. 2017;4(4):041414.

77. Matcher SJ, Cope M, Delpy DT. In vivo measurements of the wavelength dependence of tissue-scattering coefficients between 760 and 900 nm measured with time-resolved spectroscopy. Applied optics. 1997;36(1):386-96.
78. Tosh W, Patteril M. Cerebral oximetry. BJA Education. 2016;16(12):417-21.
79. Greisen G, Leung T, Wolf M. Has the time come to use near-infrared spectroscopy as a routine clinical tool in preterm infants undergoing intensive care? Philosophical Transactions of the Royal Society A: Mathematical, Physical and Engineering Sciences. 2011;369(1955):4440-51.
80. Pucci O, Sharieh S, Toronov V. Spectral and spatial characteristics of the differential pathlengths in non-homogeneous tissues: SPIE; 2008.
81. Davies DJ, Clancy M, Lighter D, Balanos GM, Lucas SJE, Dehghani H, et al. Frequency-domain vs continuous-wave near-infrared spectroscopy devices: a comparison of clinically viable monitors in controlled hypoxia. Journal of clinical monitoring and computing. 2017;31(5):967-74.
82. Weigl W, Milej D, Janusek D, Wojtkiewicz S, Sawosz P, Kacprzak M, et al. Application of optical methods in the monitoring of traumatic brain injury: A review. J Cereb Blood Flow Metab. 2016;36(11):1825-43.
83. Ehlis A-C, Barth B, Hudak J, Storchak H, Weber L, Kimmig A-CS, et al. Near-Infrared Spectroscopy as a New Tool for Neurofeedback Training: Applications in Psychiatry and Methodological Considerations. Japanese Psychological Research. 2018;60(4):225-41.
84. Minagawa Y, Xu M, Morimoto S. Toward Interactive Social Neuroscience: Neuroimaging Real-World Interactions in Various Populations. Japanese Psychological Research. 2018;60(4):196-224.
85. Eggebrecht AT, Ferradal SL, Robichaux-Viehoever A, Hassanpour MS, Dehghani H, Snyder AZ, et al. Mapping distributed brain function and networks with diffuse optical tomography. Nature photonics. 2014;8(6):448-54.
86. Ferrari M, Quaresima V. Near Infrared Brain and Muscle Oximetry: From the Discovery to Current Applications. Journal of Near Infrared Spectroscopy. 2012;20(1):1-14.
87. Saager RB, Berger AJ. Direct characterization and removal of interfering absorption trends in two-layer turbid media. J Opt Soc Am A Opt Image Sci Vis. 2005;22(9):1874-82.
88. Tgavalekos K, Pham T, Krishnamurthy N, Sassaroli A, Fantini S. Frequency-resolved analysis of coherent oscillations of local cerebral blood volume, measured with near-infrared spectroscopy, and systemic arterial pressure in healthy human subjects. PLoS One. 2019;14(2):e0211710.
89. Tong Y, Lindsey KP, de BFB. Partitioning of physiological noise signals in the brain with concurrent near-infrared spectroscopy and fMRI. J Cereb Blood Flow Metab. 2011;31(12):2352-62.
90. Leamy DJ, Ward TE, Sweeney KT. Functional Near Infrared Spectroscopy (fNIRS) synthetic data generation. Conf Proc IEEE Eng Med Biol Soc. 2011;2011:6589-92.
91. Prince S, Kolehmainen V, Kaipio JP, Franceschini MA, Boas D, Arridge SR. Time-series estimation of biological factors in optical diffusion tomography. Phys Med Biol. 2003;48(11):1491-504.
92. Boas DA, Strangman G, Culver JP, Hoge RD, Jasdzewski G, Poldrack RA, et al. Can the cerebral metabolic rate of oxygen be estimated with near-infrared spectroscopy? Phys Med Biol. 2003;48(15):2405-18.
93. Murata Y, Sakatani K, Katayama Y, Fukaya C. Increase in focal concentration of deoxyhaemoglobin during neuronal activity in cerebral ischaemic patients. J Neurol Neurosurg Psychiatry. 2002;73(2):182-4.
94. Eggebrecht AT, White BR, Ferradal SL, Chen C, Zhan Y, Snyder AZ, et al. A quantitative spatial comparison of high-density diffuse optical tomography and fMRI cortical mapping. NeuroImage. 2012;61(4):1120-8.
95. Arridge SR, Schweiger M. Photon-measurement density functions. Part 2: Finite-element-method calculations. Applied optics. 1995;34(34):8026-37.
96. Subhadra S, Brian WP, Shudong J, Hamid D, Keith DP, editors. Validation of hemoglobin and water molar absorption spectra in near-infrared diffuse optical tomography. ProcSPIE; 2003.

97. Liebert A, Wabnitz H, Grosenick D, Moller M, Macdonald R, Rinneberg H. Evaluation of optical properties of highly scattering media by moments of distributions of times of flight of photons. Applied optics. 2003;42(28):5785-92.